A MULTI-SCALE FRAMEWORK FOR THERMO-VISCOELASTIC ANALYSIS OF FIBER METAL LAMINATES

A Dissertation

by

SOURABH SAWANT

Submitted to the Office of Graduate Studies of
Texas A&M University
in partial fulfillment of the requirements for the degree of

DOCTOR OF PHILOSOPHY

December 2008

Major Subject: Mechanical Engineering

A MULTI-SCALE FRAMEWORK FOR THERMO-VISCOELASTIC ANALYSIS OF FIBER METAL LAMINATES

A Dissertation

by

SOURABH SAWANT

Submitted to the Office of Graduate Studies of
Texas A&M University
in partial fulfillment of the requirements for the degree of

DOCTOR OF PHILOSOPHY

Approved by:

Chair of Committee,	Anastasia Muliana
Committee Members,	Junuthula Reddy
	William Schneider
	Jose Roesset
Head of Department,	Dennis O'Neal

December 2008

Major Subject: Mechanical Engineering

ABSTRACT

A Multi-scale Framework for Thermo-viscoelastic Analysis of Fiber Metal Laminates.

(December 2008)

Sourabh Sawant, B.E, Shivaji University, India; M.Tech, Indian Institute of Technology Madras, India

Chair of Advisory Committee: Dr. Anastasia Muliana

Fiber Metal Laminates (FML) are hybrid composites with alternate layers of orthotropic fiber reinforced polymers (FRP) and isotropic metal alloys. FML can exhibit a nonlinear thermo-viscoelastic behavior under the influence of external mechanical and non-mechanical stimuli. Such a behavior can be due to the stress and temperature dependent viscoelastic response in one or all of its constituents, namely, the fiber and matrix (within the FRP layers) or the metal layers. To predict the overall thermo-viscoelastic response of FML, it is necessary to incorporate different responses of the individual constituents through a suitable multi-scale framework. A multi-scale framework is developed to relate the constituent material responses to the structural response of FML. The multi-scale framework consists of a micromechanical model of unidirectional FRP for ply level homogenization. The upper (structural) level uses a layered composite finite element (FE) with multiple integration points through the thickness. The micromechanical model is implemented at these integration points. Another approach (alternative to use of layered composite element) uses a sublaminate

model to homogenize responses of the FRP and metal layers and integrate it to continuum 3D or shell elements within the FE code. Thermo-viscoelastic constitutive models of homogenous orthotropic materials are used at the lowest constituent level, i.e., fiber, matrix, and metal in the framework. The nonlinear and time dependent response of the constituents requires the use of suitable correction algorithms (iterations) at various levels in the multi-scale framework. The multi-scale framework can be efficiently used to analyze nonlinear thermo-viscoelastic responses of FML structural components. The multi-scale framework is also beneficial for designing FML materials and structures since different FML performances can be first simulated by varying constituent properties and microstructural arrangements.

ACKNOWLEDGEMENTS

This is an excellent opportunity to thank all those who have contributed to my doctoral studies and supported me during this journey. I would like to express my deep and sincere gratitude to my advisor, Dr. Anastasia Muliana. She has been a true and an ideal guide during this academic journey by providing me with invaluable guidance and constant supervision during my doctoral studies. I whole-heartedly thank her for providing me with financial support during the entire duration of my doctoral studies. I consider myself very lucky to have carried out my research under her able guidance. I am also grateful to my committee members, Dr. J. N. Reddy, Dr. William Schneider and Dr. Jose Roesset, for their helpful comments and suggestions.

I would like to thank my wife, Vasundhara, for her moral and emotional support during this entire period. I entered Texas A&M University to pursue my PhD after working in industry for 5 long years. Coming back to the academic field and successfully carrying out my PhD studies would not have been possible without the constant encouragement and unconditional love and support of my wife. I would also like to thank my parents for supporting my decision to pursue higher studies. Their desire to support me in any way during this academic venture was in itself the greatest moral support for me. I thank my in-laws for their unwavering faith in me. I would also like to thank my friends and relatives (especially my brother, Swapnil) for their love and support.

In the days to come, I will surely be thinking whether I have thanked enough all the people mentioned above in this acknowledgement. As a final word, I sincerely thank all others who contributed their efforts, however miniscule, towards making my dissertation successful.

NOMENCLATURE

ARALL®	Aramid Reinforced Aluminum Laminate
CLT	Classical Laminate Theory
ESL	Equivalent Single Layer
FE	Finite Element
FML	Fiber Metal Laminate
FRP	Fiber Reinforced Polymer/Plastic
FSDT	First-order Shear Deformation Theory
GFRP	Glass Fiber Reinforced Polymer/Plastic
GLARE®	Glass Reinforced Aluminum Laminate
HSDT	Higher-order Shear Deformation Theory
KFRP	Kevlar Fiber Reinforced Polymer/Plastic
NR	Newton-Raphson
RVE	Representative Volume Element
TCM	Thermo-rheologically complex material
TSM	Thermo-rheologically simple material
UMAT	User Material (Subroutine)
Vf	Fiber Volume Fraction

TABLE OF CONTENTS

CHAPTER Page

LIST OF FIGURES

FIGURE Page

FIGURE Page

FIGURE Page

FIGURE Page

LIST OF TABLES

TABLE Page

CHAPTER I

INTRODUCTION

1.1 MOTIVATION

Multilayered composite systems often refer to composites having alternating layers of different fiber reinforcements such as unidirectional fibers, woven fabrics, braided preforms, or randomly oriented fibers. While each constituent in the multilayered composites retains its features, the composite material reveals macroscopic mechanical properties that are superior to the ones of the parent constituents. Another form of multilayered composites combines fiber reinforced polymers (FRP) laminas and metal sheets, which are known as fiber metal laminates (FML). FML have alternate metal and FRP layers with metal on the top and the bottom of the lay-up. The motivation behind the development of FML can be traced back to the objective of obtaining fatigue resistant aircraft wings with good impact resistance. The FML surprisingly showed enhanced fatigue resistance as compared to both, the monolithic aluminum and FRP. The improved fatigue properties are attributed to the reduced crack propagation due to fiber-bridging mechanism in FML. Several types of FML such as glass reinforced aluminum laminates (GLARE®) and aramid reinforced aluminum laminates (ARALL®) have been developed. The FML have been applied in the primary load bearing components of aircraft fuselage and wings (e.g. fuselage of Airbus 380 is made of GLARE®, lower wing structure of Fokker F-27 aircraft and cargo door of McDonnell

---

This dissertation follows the style of Acta Mechanica.

Douglas C-17 aircraft is made of ARALL®).

Manufacturing processes, different transport (thermal conductivity, moisture diffusivity, etc) and mechanical properties in every layer and also within the layer's constituents often lead to residual stresses (or prestresses) at various length scales: laminate, ply, and constituents. The mechanical properties of these FML composite materials are also affected by change in environmental conditions (humidity and temperatures). Due to their complex microstructures, modeling the responses of FML composites in order to predict the performance of FML composite structures becomes very challenging. Furthermore, the mechanical properties of each constituent often vary with time, stress, temperature, and moisture, which add complexity in modeling the overall composite responses. The development of new synthetic fibrous reinforcements (which are relatively more susceptible to time, temperature and humidity dependent deformations) and new combinations of angle ply lay-ups within the FRP layers is another motivation for a predictive capability of the overall time dependent behavior of these materials. In case of FML, the homogenous metal layers can also contribute to the overall time dependent response.

Significant progress with regards to understanding linear elastic and elastic-plastic properties of GLARE® and ARALL® has recently been made. However, very limited studies have been done in understanding the nonlinear viscoelastic and long-term behavior of FML. This has lead to a relatively higher factor of safety for usage of these materials. A research in this area can improve reliability in using FML. Predictive capabilities on the overall performance of FML can result in significant cost saving

during material and structural design process. This can open opportunity in using FML in other areas such as marine and offshore structures, automobiles, railways, and infrastructure.

New development of advanced material also requires rigorous structural analysis and design. Finite element (FE) analysis has been widely used in analyzing thermo-mechanical responses of practical structural components with complex geometries and loadings. The FE analysis of FML composites should take into account the anisotropy, macroscopic heterogeneity of each layer, and the lay-up of the laminate with a minimum expense in terms of the added computational costs. A multi-scale model has been developed to link constitutive models of the constituents to the overall response of composite structures. In case of nonlinear responses of the constituents, a two-way homogenization procedure is necessary to obtain effective responses from the constituents and recognize detailed nonlinear constitutive relations in the constituents due to external loadings. A multi-scale framework of FML requires: 1) to obtain the nonlinear time dependent response of each constituent of FML; 2) a ply level homogenization scheme for the FRP layers such that it recognizes the different responses in the fiber and matrix; and 3) a laminate level homogenization scheme to combine the response of each layer of the FML.

1.2 RESEARCH OBJECTIVE

The present study deals with the multi-scale analysis of thermo-viscoelastic behaviors of FML, focusing on GLARE® and ARALL®. The thermo-viscoelastic

behaviors of the thermo-rheologically complex materials (TCM) are considered for each constituent in the FML. A time integration algorithm for the general nonlinear viscoelastic constitutive models of orthotropic media is developed and used for the constituents (fiber, polymer matrix, aluminum). Micromechanical and laminate level homogenization procedures are formulated to obtain the overall response of the FML. This constitutive multi-scale material model is designed to be compatible with general displacement based FE code suitable for performing structural analysis. By linking different constitutive material models of fiber, matrix, and metal layers through micromechanical and laminate level homogenization, a multi-scale framework for FML is formulated.

1.3 LITERATURE REVIEW

This section presents state of the art knowledge in understanding thermo-mechanical and time-dependent behavior of FML. The literature review includes analytical, numerical, and experimental works on the nonlinear constitutive modeling of FML. The studies on the thermo-viscoelastic behaviors of the FRP and its constituents, the fiber and polymer matrix are also reviewed. Finally, the multi-scale modeling of layered composites is reviewed.

1.3.1 Overview of FML

Fiber metal laminates (FML) consists of thin metal alloy sheets bonded alternately with fiber-reinforced plastic (FRP) layers. Aluminum alloy is often used as the metal

sheets, while glass and Kevlar fibers are applied for the FRP layers. These FML (hybrid) composites offer superior mechanical properties over conventional FRP composites as well as monolithic aluminum alloys. Donnellan & Cook [15] have outlined the various advantages of FML in comparison with its parent constituents. Aluminum sheets are always placed on the top and bottom to protect against impact loading and environmental (temperature, moisture, ultraviolet, and other solvent) attack. In FML the fiber need not be aligned in the transverse direction since the aluminum provides sufficient strength and stiffness in that direction. The fiber-bridging, which is one of the characteristics of failure mechanisms in continuous fiber composites, impedes the growth of cracks in the aluminum layers under tensile fatigue. These laminates also possess the traditional advantages of metals namely the impact strength, compressive strength, formability, easy machining and supportability and inspectability. The presence of a viscoelastic resin imparts good vibration and acoustic damping ability to the FML. The resin also provides an embedded thermal insulation and high lightening strike resistance. Assembly of FML parts is easier than corresponding sheet metal structure since most of the integration of parts is already carried out during the lay-up process. This can reduce number of mechanical joints and hence reduce areas of stress concentration. In addition, damaged laminates can be repaired using conventional metal repair methods such as riveting of FML repair patches. In fact, FML offer another better repair alternative (with superior damage tolerance) of using bonded FML repair patches as well. Krishnakumar [44] has provided a survey of extensive works on manufacturing, testing, and modeling of the GLARE® and ARALL® FML.

Other types of FML such as carbon reinforced aluminum laminates (CARALL) (Haga and Kimura [24]) and low strength low cost vinylon reinforced aluminum laminates (VIRALL) (Sui et al., [77]) have also been developed. CARALL possesses an inherent disadvantage of low resistance to galvanic corrosion due to good electrical conductivity of carbon fibers. CARALL and ARALL® both require a residual stress relief treatment. A significant residual stress is always induced during curing of these laminates due to the negative coefficient of thermal expansion of aramid and carbon. Haga et al. [25] have discussed about a new hybrid FML with alternate bonded layers of strength aluminum sheets and unidirectional hybrid FRP layers. The hybrid FRP layer is composed of a carbon-FRP (CFRP) layer sandwiched in between two Kevlar-FRP (KFRP) layers. This lay-up introduces an insulating KFRP layer between CFRP and aluminum layer thus taking care of the galvanic corrosion in CARALL laminates. Rommel et al. [70] and Cortes and Cantwell [13] have investigated a number of FML based on titanium alloy and special high temperature adhesives reinforced by carbon fibers. These FML are potential candidates for high temperature applications including supersonic jets and space shuttles.

A historic overview of the developments of FML is given by Vermeeren [80]. FML were first developed for the Fokker F-27 aircraft in the 70s. It was observed that these laminates have superior fatigue properties. A lower cost of the FML compared with full composites was also the driving force for development of FML. ARALL® was first applied to the wing structure of the F-27 aircrafts. Later when ARALL® was applied to the fuselage, they were found to be ineffective due to fiber breakage under fuselage

loading. This was attributed to the weak fiber-matrix bond in KFRP. GLARE® with a strong glass fiber-epoxy matrix bond appeared to be the solution to this problem. A number of variants of GLARE® suitable for various regions of the fuselage were developed. These variants are mentioned in Table 1.1. The development of GLARE® was speeded due to the Airbus A380 project. This project resulted in about 100 sub-projects in the research of GLARE®. The dimensions of GLARE® panels are limited only by the width of aluminum layers and not in the length direction (rolling direction). Vermeeren et al. [81] have also discussed the "splice" concept of joining GLARE® panels to efficiently produce wider fuselage skin panels. The concept is similar to a lap joint with butted aluminum sheets placed in between continuous prepregs.

Table 1.1 Variants of GLARE® and ARALL®

FML	Grade	Sub	Metal sheet		Fiber Reinforced Polymer Prepreg		Main beneficial characteristics
			Thickness (mm)	Alloy	Thickness (mm)	Fiber angle	
GLARE	Glare1	-	0.3-0.4	7475-T761	0.25	0/0	Fatigue, Strength, Yield stress
	GLARE 2	GLARE 2A	0.2-0.5	2024-T3	0.25	0/0	Fatigue, Strength
		GLARE 2B	0.2-0.5	2024-T3	0.25	90/90	Fatigue, Strength
	GLARE 3	-	0.2-0.5	2024-T3	0.25	0/90	Fatigue, Impact
	GLARE 4	GLARE 4A	0.2-0.5	2024-T3	0.375	0/90/0	Fatigue, Strength in 0 direction
		GLARE 4B	0.2-0.5	2024-T3	0.375	90/0/90	Fatigue, Strength in 90 direction
	GLARE 5	-	0.2-0.5	2024-T3	0.5	0/90/90 /0	Impact
	GLARE 6	GLARE 6A	0.2-0.5	2024-T3	0.25	+45/-45	Shear, Off-axis properties
		GLARE 6B	0.2-0.5	2024-T3	0.25	-45/+45	Shear, Off-axis properties
ARALL	Arall 1	-	0.3	7075-T6	0.216	0	High strength
	Arall 2	-	0.3	2024-T3	0.216	0	Increased flammability
	Arall 3	-	0.3	7475-T76	0.216	0	Controlled toughness, Good exfoliation resistance, High strength
	Arall 4	-	0.3	2024-T8	0.216	0	High temperature stability

Note that the rolling direction for Aluminum is defined as 0˚ and the transverse rolling direction is defined as 90˚.

1.3.2 Existing studies on the nonlinear constitutive models of FML

The FML may exhibit nonlinear viscoelastic and/or plastic behaviors due to the existence of FRP and metal alloy layers. The nonlinearity is intensified under combined mechanical and non-mechanical effects such as elevated temperatures and humid environments. A predictive capability on the overall nonlinear response of the FML that recognizes different responses in every FRP and metallic layers becomes necessary.

Van Rooijen et al. [79] have used a rule of mixtures in terms of the metal volume fraction to obtain effective elastic modulus, yield strength, and ultimate tensile strength of the FML. Kawai et al. [42] have carried out an experimental investigation of the off-axis inelastic and fracture behavior of GLARE® under static tensile loading. The fracture strength from the experimental tests was predicted by the Tsai-Hill Theory. The experiments also revealed good in-plane shear strength compared to that of unidirectional glass lamina. The effective response of the laminate was predicted using the modified Classical Lamination Theory (CLT), which takes into account the effect of failure-induced elastic degradation of GFRP layers. The analytical results obtained using the partial lamina fracture model (based on the assumption that ply failure causes stiffness reduction in transverse direction only) are comparable with experimental results. Chen & Sun [10] have modeled the elastic-plastic behavior of an ARALL® laminate using CLT having KFRP layers modeled as orthotropic elastic and aluminum as orthotropic elastic plastic (orthotropic plasticity is introduced on account of rolling of aluminum). Hashagen et al. [37] have used FE method for modeling FML layers. An elastic-plastic material model was used for the FRP and aluminum layers. A geometrically nonlinear solid-like shell element with the nonlinear material models integrated at the integration points was developed for the FML. Barbero et al. [4] have used FE based on layerwise theory with piecewise linear displacement interpolation for the elastic analysis of ARALL® laminates. They have considered additional layers of pure resin in between the FRP and metal sheets in the numerical modeling. Pindera et al. [64] have carried out an experimental investigation of the creep response of ARALL®

laminates at 121˚ C with and without mechanical pre-straining effects. A pronounced viscoelastic behavior is observed in ARALL® at stress levels below its proportional limit. Aluminum exhibits nonlinear viscoelastic behavior while KFRP exhibits linear viscoelastic behavior. The CLT theory was used to model the overall creep response of the ARALL® laminates. Botelho et al. [6] have obtained viscoelastic properties such as storage modulus and loss modulus for glass FRP, aluminum, and GLARE®. The effect of hygrothermal loading on the viscoelastic properties of these three materials was examined. It was found that aluminum provides good protection against moisture absorption hence there is no significant deterioration of properties on account of hygrothermal loading. Most of the existing studies for time dependant behavior of FML have been restricted to a few experimental studies. To the best knowledge of this author, there is no significant research carried out for analytical and numerical modeling of the nonlinear time dependant behavior of FML under general mechanical and non-mechanical loadings, so that they can be used for analysis of practical structures with the aid of numerical techniques such as FE method.

1.3.3 Nonlinear thermo-viscoelastic behaviors of fiber reinforced polymers (FRP)

In order to predict the overall performance of FML, understanding nonlinear and time dependant behaviors of its constituents, which are the fiber, polymer matrix and metal alloy, becomes essential. In general, the constitutive model for the FRP depends on time, stress, strain, temperature, moisture and other ageing effects such as ultraviolet radiation and oxidation. FRP composites exhibit significant viscoelastic behavior

primarily due to the viscous flow of the polymeric matrix. Viscoelastic behaviors of polymers are intensified under extreme temperatures and humid environments. The use of synthetic (polymer) fibers such as aramid and polyethylene in the FRP results in a more complex viscoelastic behavior. Experimental tests on aramid fibers and aramid FRP composites show significant temperature dependences on the elastic and time-dependent properties of the aramid fibers and aramid FRP (Hanson [34]; Walruth [83]; Wang et al [86]; Haftchenari et al. [23]; Alwis and Burgoyne [2]). It is shown that high temperatures decrease the strength and stiffness of the materials. Experimental tests on high temperature polyimide resin and polyimide reinforced composites also show strong temperature dependences on the elastic and viscoelastic response characteristics, strength, and thermal properties (Benedikt et al. [5]; Caruthers et al. [8]; Harris and Gates [35]; Morgan et al. [49]; and Rupnowski et al. [71]. Under an extreme service environment, hygrothermal induced property deterioration is linked to chain scission of the polyimide cross-links (Morgan et al. [49]). Based on their rheological responses at different temperatures, FRPs can be classified as thermo-rheologically simple materials (TSM) or thermo-rheologically complex materials (TCM). If the temperature affects mainly the time-dependant (transient) material properties and the effect of temperature can be incorporated through a time-scale shift factor only, materials are categorized as TSM. For TSM, the temperatures do not change the configuration of the polymer molecular (chemical) structures nor affect its elastic and long-term (relaxed) moduli. On the other hand, for TCM, temperature affects the polymer molecular structure significantly and influences the material's initial (elastic), long-term (equilibrium), and

time dependant (transient) properties (Harper & Weitsman [36]; Caruthers & Cohen [9]; Wineman & Rajagopal [88]). Current works on modeling temperature dependent viscoelastic responses have been extensively driven by the assumption of thermo-rheologically simple materials (TSM), in which the temperature effect is incorporated only through a time-scale shift factor (Antonakakis et al [3]; Hashin et al. [38]; Morland et al. [50]). Recently Muliana and Sawant [58] presented micromechanical modeling of FRP having TCM responses in the fiber and matrix constituents.

Experimental tests on the viscoelastic behavior of FRP are often done under constant stress (creep loading) or constant strain (relaxation test). The tests are performed on several off-axis FRP specimens at various load levels and/or several environmental conditions. Depending on the fiber materials and duration of tests, the viscoelastic behaviors along FRP fiber direction can be significant. For example, FRP with Kevlar fiber show time dependant response along its unidirectional fiber direction, while the ones with glass and carbon fibers do not experience significant viscoelastic response along their unidirectional fiber direction under a short-term period. While in the transverse and off-axis fiber direction, non-negligible viscoelastic responses are often exhibited due to the matrix-dominated mode of loading. Linear viscoelastic response is considered whenever stress or strain response satisfies proportionality condition and superposition principle. Therefore, for a linear viscoelastic response, creep and relaxation functions are interrelated and permit the construction of one from the other. In case of a nonlinear viscoelastic material, creep and relaxation functions are often not invertible. This is the case when large stress levels are applied, especially when

combined with elevated temperatures or high moisture. In addition, existence of imperfections and discontinuities in the material can enhance the nonlinear viscoelastic behavior. Scott et al [75] have provided an extensive review of technical literature on the experimental characterization of viscoelastic behaviors of FRP.

1.3.4 Analytical and numerical methods for analyzing nonlinear viscoelastic responses

Hereditary integral or differential operator form is often employed for modeling the viscoelastic response of polymer-based materials (Findley et al. [18]; Christensen [11]; Wineman & Rajagopal [88]). The Schapery's nonlinear single integral form [74] is widely used for the nonlinear viscoelastic polymers and FRP. The stress or strain dependent nonlinear parameters can be incorporated to the Schapery's model. In case of FRP, the nonlinear parameters are often expressed in terms of the Von mises effective stress or the octahedral shear stress in the polymer matrix such as discussed by Lou & Schapery [47]. It should also be noted that the Schapery constitutive model is suitable for small deformations problems (as in our case) and it violates the balance of angular momentum for large deformations (Rajagopal and Shrinivasa [67]). Hilton and Yi [40] have performed the analytical investigation of anisotropic and isotropic viscoelastic Poisson's ratio time effects. They have discussed the implications of having different time functions (which is generally true for FRP) in all directions for a general anisotropic material on the Poisson's ratios in different directions. The Poisson's ratios are usually nonlinear functions of pair of normal strains and hence nonlinear functions of

stress and time histories. They can be time independent only under a set of restrictive conditions such as identical time functions in all directions and constant stresses. They are also time independent if the stress tensor can be expressed as uncoupled functions in the temporal and spatial domain. Further the Poisson's ratios determined under uniaxial loading may not be applicable to multi-axial loading cases. The Poisson's ratio is a function of the sequence of loading as well.

Numerical algorithms that are compatible with FE analyses have been widely developed mainly for analyzing viscoelastic constitutive models of TSM. A recursive numerical algorithm has been applied for analyzing linear and nonlinear viscoelastic integral models for isotropic materials (Taylor et al. [78]; Henriksen [39]; Lai and Bakker [45]; Kaliske and Rothert [41]; and Haj-Ali and Muliana [29]). The nonlinear stress-based material parameters were incorporated in the above viscoelastic models. The temperature effect was carried through a time-shift factor, which refers to a class of TSM. A similar recursive approach was used by Feng [17] for modeling linear viscoelastic materials described by the Voltera integral equation. Zienkiewicz et al. [91] used a recursive method to solve a differential equation in terms of strain rate on a spring-dashpot mechanical analog model (Kelvin model). The stress and the material properties were assumed to be constant over the time interval. Simo and Hughes [76] presented numerical algorithms of inelastic materials including viscoelasticity. Constitutive material models with internal state variables were used to derive a strain-based nonlinear viscoelastic models. Muliana and Khan [55] derived a recursive-

iterative algorithm suitable for TCM behaviors. The algorithm is verified for TCM behaviors of FM73 and Hercules 3502 polymers.

Several time-integration algorithms have been proposed for analyzing linear viscoelastic responses of anisotropic media. Zocher et al. [92] proposed a FE scheme for linear viscoelastic orthotropic materials using an integration point update algorithm. A single reduced time was assumed in all the directions (though this is usually not the case for many composites). The stress increment was decomposed into a current linearized part and a history part stored from the previous increment. Instead of assuming a constant strain over a time step, the strain rate was assumed to be constant, thus resulting in a better prediction of creep. This method was suitable only for linear viscoelastic responses, in which the updated consistent tangent stiffness or iterative procedure can be avoided. Yi et al. [89] developed a FE integration procedure for orthotropic materials subjected to mechanical and hygrothermal loading. A recursive viscoelastic exponential series was generated from the time-domain integration of the virtual work with a linear viscoelastic constitutive model. An equal time step was used which either provides computational accuracy at the cost of efficiency (if small time step is chosen) or provides computational efficiency at the cost of accuracy (if large time step is chosen).

A numerical method has also been developed for a nonlinear anisotropic viscoelastic model. Poon and Ahmad [65, 66] proposed an integration scheme for stress relaxation with strain-based nonlinear functions. The Schapery's nonlinear integral model was applied independently for each of the anisotropic moduli. The time shift factor used for incorporating the temperature dependant property in TSM was

independently defined for each direction. The choice of the state variables resulted in conversion of the hereditary integral to a set of linear differential equations. The iterations for stress correction were not required due to the use of strain based nonlinear parameters. Though iterative stress correction can be avoided by use of strain-based parameters, it is often more difficult to conduct experimental tests for characterizing the strain based material parameters. Kennedy [43] developed a nonlinear viscoelastic algorithm for orthotropic materials that are compatible with eight node layered shell element. The nonlinear viscoelastic constitutive model followed the one used by Lou and Schapery [47]. The hereditary effects were taken care by separating the transient creep compliance as an exponential series and a steady flow term. The recursive approach was used for solving the hereditary integral model. Integration at each time step was performed using the mid-point method. Dillard and Brinson [14] developed a hereditary based numerical algorithm for two dimensional analysis of orthotropic laminated composites based on first-order forward time-stepping solution in conjunction with the classical lamination theory. Logarithmic time stepping was used for the algorithm. The use of an explicit solution method and logarithmic time stepping resulted in the algorithm to be only conditionally stable. Gramoll et al. [21] solved the numerical instability problem in the previous algorithm [14]. Instead of solving the hereditary integral, each Kelvin element represented by Prony series was solved independently as a differential equation and the solution was summed together, a technique similar to that presented by Zienkiewicz et al. [91]. The stress was assumed to be a function of current strain as well as the current strain rate. The nonlinear differential equation was solved

using the Backward Euler (implicit) method. A single nonlinear stress parameter, which is a function of current octahedral shear stress in the matrix, was assumed. The resulting nonlinear equations were solved using the Newton-Raphson method. Sawant & Muliana [73] have used a modified Schapery's nonlinear single integral form to include the effects of stress and temperature on time-dependent material responses suitable for the TCM behavior. A recursive-iterative algorithm is developed to calculate the current stress state from the given strains and temperature, and the history variables stored at the previous time step. The stress and temperature fields influence the elastic and time-dependent material constants. Extensive literature reviews on the development of numerical algorithms of viscoelastic materials can be found in Zocher et al. [92].

1.3.5 Multi-scale models for analyzing multi-layered composites

The multi-layered composites, i.e., laminated composites and FML, possess multi-scale characteristics. The lowest continuum scale can consists of various forms of fiber constituents dispersed in the matrix medium. The upper scale is a lamina such as fiber reinforced matrix and monolithic metal layer. The highest material scale comprises of laminate with various stacking sequences. Multi-scale modeling approaches have been developed to predict overall responses of the multi-layered systems through several levels of material homogenization schemes.

The simplest homogenization technique is the rule of mixtures in which the overall properties of composites are proportional to the volume contents of the constituents. The planar constitutive relations are developed on the basis of iso-strain

assumption in the fiber direction and iso-stress assumption in the transverse and shear direction (Eckold [16]). Fish et al. [19] have considered a two-phase medium for homogenization of an elastic fiber and an elasto-plastic matrix. An incremental approach with implicit stress update schemes is used for the homogenization to obtain the overall response of the composite. Several micromodels with detailed stress-strain fields of the fibers and matrix have been formulated, which can be found in Aboudi [1], Christensen [12], Nemat-Nasser and Hori [59]. A simplified unit-cell model of a representative volume element (RVE), derived from periodically distributed microstructure, has been proposed to analyze fiber and particle reinforced composites (Haj-Ali and Muliana [28]; Haj-Ali [26]; Muliana and Haj-Ali [52]; Muliana and Kim [56]). The homogenization schemes are formulated in terms of the average constitutive relations in subcells within the unit-cell, which give approximated values of the overall composite behaviors. This method is computationally efficient and is suitable for incorporating nonlinear response and performing thermo-viscoelastic analyses of composite structures at multiple length-scales (Muliana and Haj-Ali [52]; Muliana [51]). The above micromechanical models are derived to obtain effective viscoelastic composites having linear elastic inclusions (fibers or particles) and inelastic/viscoelastic matrix. In such case, the overall time-dependent behaviors of the composites are controlled by the matrix viscoelasticity.

To date, limited micromechanical models have been formulated to analyze thermo-viscoelastic behaviors of FRP having different fiber and matrix viscoelasticity. Haddad and Tanary [22] proposed a microstructural model for temperature-dependent creep responses of composites having randomly oriented and short fibers. Both fiber

and matrix exhibited linear viscoelastic behaviors. The time-dependent behavior of the individual fiber-bundle was formulated as a combination of a viscoelastic matrix substance within the bundle and an ensemble of unidirectional elastic fibers. Brinson and Knauss [7] used the correspondence principle of viscoelasticity to study the time-temperature behaviors of composite materials. Each phase in the composite system was modeled as TSM with linear viscoelastic and the resulting overall composite properties are TCM. A numerical model was presented to examine the TCM behaviors of the studied composite systems. Hashin et al. [38] used a concentric cylinder assembly (CCA) and a hexagonal periodic array to predict thermo-viscoelastic behaviors of unidirectional fiber composites having an elastic fiber and a TCM matrix system. Numerical results were presented for creep strains under isothermal and cyclic temperature conditions. Sadkin and Aboudi [72] and Aboudi [1] used the method of cell (MOC) to analyze thermal effects on the viscoelastic response of unidirectional fiber reinforced composites. The viscoelastic matrix was modeled as a TCM material. Predictions were compared with longitudinal and transverse creep responses of graphite/epoxy composites generated using a detailed finite element (FE) unit-cell. Recently, Muliana and Haj-Ali [54] derived micromechanical models for multi-layered composites with TCM characteristics of the polymer matrix. The fibers are assumed linearly elastic. The overall creep responses of the composites at different stresses and temperatures obtained from the micromodel formulations are compared with experimental data of the multi-layered composites with 0^o, 45^o, and 90^o unidirectional fiber orientations.

The response of a laminate (made by stacking of laminas) can be obtained using several lamination theories. Reddy [69] has provided a detailed overview of the lamination theories. There are two classes of lamination theories namely the two dimensional equivalent single layer theories (ESL) and the three dimensional elasticity theories. In the equivalent single layer theories, the heterogeneous lay-up is treated as a single layer with a constitutive behavior that accounts for properties of each layer and the sequence of the lay-up. The CLT, the first-order shear deformation theory (FSDT) and the higher-order shear deformation theory (HSDT) are the ESL theories used for analysis of laminates. The CLT provides good results for thin section laminates where the transverse shear deformation is negligible. In case of thick section laminates, the shear deformation theories are used to account for the transverse shear deformation. The laminates can also be analyzed by detailed 3D modeling of each lamina, i.e. 3D layerwise theories and the sublaminate model. These 3D theories are capable of providing the 3D stress field for each lamina and hence can model phenomenon such as delamination and ply-level damage. Haj-Ali et al. [27, 28] proposed a sublaminate model for laminate level homogenization to study nonlinear time-dependent responses of thick-section multi-layered composites. The sublaminate model is based on the 3D lamination theory assuming an in-plane strain and out of plane stress continuity and a perfect bond between layers.

Literature indicates a few attempts at multi-scale modeling of nonlinear and time dependent behavior of composites structures. Yu and Fish [90] have presented a multi-scale homogenization in both the spatial and temporal domain for coupled multi-physics

problems and the framework is applied for a coupled thermomechanical viscoelastic analysis. Rapidly varying spatial and temporal scales are introduced through separate scaling parameters to capture the effect of local heterogeneities at different time scales. Fish and Shek [20] have described the procedure for nonlinear multi-scaling of composite structures. A coupled multi-scaling is achieved using Newton-multilevel method, which involve an iterative method to determine the consistent tangent stiffness at each level after suitable corrections. A multi-scale framework based on integrated micromechanical model and FE structural analyses for nonlinear elastic response of laminated composite structures was studied by Pecknold and Haj-Ali [61] Haj-Ali and Pecknold [32] and Pecknold and Rahman [62]. This framework was modified by Muliana and Haj-Ali [53] and Haj-Ali and Muliana [30] to include the nonlinear and time dependent effects in layered composite structures. The framework is used to analyze nonlinear viscoelastic behaviors of pultruded composites structures with layers of E-glass unidirectional fibers and continuous filament mat. The micromechanical homogenization for each layer and a sublaminate approach for homogenizing the two layers into a nonlinear anisotropic equivalent continuum were used in conjunction with finite element (FE) analysis. Muliana and Haj-Ali [54] have also carried out the multi-scale modeling of long-term behavior of laminated composite structures by incorporating the micromechanical model for each layer of laminated composite and integrating it with three-dimensional and shell-based finite elements.

1.4 OUTLINE OF THE DISSERTATION

The dissertation is organized as follows:

1. Chapter II presents the development of a numerical algorithm for thermo-viscoelastic analysis of orthotropic materials that belong to TCM. The nonlinearity due to stress and temperature is incorporated to the elastic and time-dependent material constants. This algorithm is verified using creep data of orthotropic glass-epoxy and glass-vinylester composites. The algorithm can also be reduced to obtain viscoelastic responses of isotropic materials. This is verified by applying it to the thermo-viscoelastic analysis of isotropic epoxy resin. Finally the algorithm is used for a sequential thermo-mechanical analysis of a plate with a hole made of unidirectional glass-vinyl ester FRP.
2. Chapter III presents the development of a concurrent micromechanical model for FRP systems with unidirectional fiber reinforcements. Both fibers and polymeric matrix are allowed to exhibit nonlinear thermo-viscoelastic behavior of TCM. The fibers are assumed to be orthotropic and the polymer matrix is considered as isotropic. The micromodel of the FRP is idealized with four fiber and matrix subcells. A constant average stress and strain is assumed for each subcell and an incremental formulation is obtained in terms of these average strains and stresses. The algorithm developed in chapter II is integrated within the micromechanical model to obtain the orthotropic viscoelastic response of the fiber. The thermo-viscoelastic responses obtained from the concurrent micromodel are verified with available experimental data. Detailed FE models (with circular fiber in a square

matrix) of the FRP microstructures are generated for several fiber volume fractions. Thermo-viscoelastic responses from the micromodel are also compared to the ones of the detailed FRP microstructures.

3. Chapter IV presents the multi-scale approach for the analysis of FML. In this chapter, two approaches for laminate level homogenization of FML are introduced. The first approach uses a layered composite element within the finite element (FE) framework having multiple integration points through the thickness. The constitutive material models for the metallic and FRP layers are implemented separately at each material point. The second approach uses a sublaminate model to first homogenize responses of the metallic and FRP layers. The outcome of the sublaminate model is a 3D orthotropic thermo-viscoelastic response, which is implemented at the material/Gaussian points in a general shell or 3D continuum elements. The analysis with the above two approaches is also carried out with the micromechanical model (developed in chapter III) for the FRP layers of the FML. The results are verified with experimental data as well as with detailed 3D analysis. The approaches are compared in terms of computational accuracy and efficiency.
4. Chapter V presents the application of the multi-scale framework to the thermo-viscoelastic analysis of FML structures. For this purpose, a stress analysis is carried out for a part of an aircraft fuselage skin made up of GLARE®. The GLARE® skins in the fuselage are connected through splices. Such a connection is also modeled and the stress-strain responses in the critical zones are monitored.

5. The dissertation is concluded in the chapter VI with directions for further research.

CHAPTER II

A THERMO-MECHANICAL VISCOELASTIC ANALYSIS OF ORTHOTROPIC MATERIALS*

This chapter presents a numerical algorithm for nonlinear thermo-mechanical viscoelastic analyses of orthotropic materials that follow thermo-rheologically complex behaviors. The viscoelastic behavior of the individual orthotropic FRP layers and isotropic metal alloy layers of FML can be modeled using this algorithm. The previously developed recursive-iterative algorithm for stress-dependent viscoelastic behaviors on an isotropic medium (Haj-Ali and Muliana [29]) is extended to include time-temperature effects for an orthotropic medium. The algorithm is derived based on implicit stress integration solutions within a general displacement based finite element (FE) framework for small deformations and uncoupled thermo-mechanical problems. The Schapery's nonlinear single integral form is generalized for modeling viscoelastic responses of an orthotropic medium. The effects of stress and temperature are incorporated in the elastic and time-dependent material properties, which allow prediction of time-dependent responses under general stress and temperature histories. A recursive-iterative method is developed to calculate the current stress state from the given strains and temperature, and the history variables stored at the previous time step. Furthermore, a consistent tangent stiffness matrix is formulated to enhance equilibrium and avoid divergence at the structural level.

---

* Reprinted with permission from "A thermo-mechanical viscoelastic analysis of orthotropic materials" by Sawant S. P., Muliana A. H, March, 2008, Composite Structures, v 83, n 1, , p 61-72 © 2007 Elsevier Ltd.

Verifications of the numerical algorithm are first performed for linear viscoelastic behaviors of Kevlar/epoxy composites tested by Walruth [83]. This is followed by the verification of nonlinear stress-dependent viscoelastic behaviors of glass/epoxy-laminated composites tested by Lou and Schapery [47]. The performance of the recursive-iterative algorithm under multi-axial conditions is validated with responses from different off-axis angles. Next, the viscoelastic responses under combined thermo-mechanical loading are also verified with experimental data on off-axis glass/vinylester multi-layered composites tested by Muliana et al. [57]. Finally, the integrated numerical algorithm with FE framework is presented for analysis of plate with a hole.

2.1 CONSTITUTIVE MODEL FOR NONLINEAR ORTHOTROPIC VISCOELASTIC MATERIALS

A constitutive model for multi-axial stress-temperature dependent viscoelastic behavior of an orthotropic medium is presented in this section. The Schapery nonlinear single integral constitutive model [74, 47] is modified to include the effects of stress and temperature on time-dependent material responses. The following formulations will follow indicial notation equations, unless otherwise indicated. The linear viscoelastic constitutive model for anisotropic materials under uncoupled thermo-mechanical loading can be written in the form:

$$\varepsilon_{ij}(t) = \int_0^t S_{ijkl}(t-\tau)\frac{d\sigma_{kl}(\tau)}{d\tau}d\tau + \int_0^t \alpha_{ij}(T^{\tau})\frac{dT(\tau)}{d\tau}d\tau \tag{2.1}$$

or

$$\sigma_{ij}(t) = \int_0^t C_{ijkl}(t-\tau)\frac{d\varepsilon_{kl}(\tau)}{d\tau}d\tau + \int_0^t \beta_{ij}(t-\tau)\frac{dT(\tau)}{d\tau}d\tau \tag{2.2}$$

where the component of time dependent compliance and moduli tensors are $S_{ijkl}(t)$ and $C_{ijkl}(t)$, respectively; α and β are second order tensors defining coefficient of thermal expansion and thermo elastic moduli, respectively. The material symmetry and the symmetry of stress and strain tensors lead to

$$\begin{aligned} S_{ijkl}(t) &= S_{klij}(t) = S_{jikl}(t) = S_{ijlk}(t) \\ C_{ijkl}(t) &= C_{klij}(t) = C_{jikl}(t) = C_{ijlk}(t) \end{aligned} \tag{2.3}$$

In general, the material compliance or moduli can be functions of time, stress, strain, and temperature. This study formulates a time integration procedure for orthotropic viscoelastic materials having stress and temperature dependent material parameters suitable for thermo-rheologically complex materials (TCM). The time, stress, and temperature dependent compliance is expressed as:

$$S_{ijkl}(t,\sigma,T) = S_{ijkl}(0,\sigma,T) + \Delta S_{ijkl}(t,\sigma,T) \tag{2.4}$$

where $S(0,\sigma,T)$ is the compliance at time 0, which is often considered as the time independent (instantaneous elastic) compliance, and $\Delta S(t,\sigma,T)$ is the transient compliance. Substituting Eq. (2.5) into (2.2) gives

$$\begin{aligned} \varepsilon_{ij}(t) &= \int_0^t [S_{ijkl}(0,\sigma,T) + \Delta S_{ijkl}(t-\tau,\sigma,T)]\frac{d\sigma_{kl}(\tau)}{d\tau}d\tau + \int_0^t \alpha_{ij}\frac{dT(\tau)}{d\tau}d\tau \\ &= S_{ijkl}(0,\sigma,T)\sigma_{kl}(t) + \int_0^t \Delta S_{ijkl}(t-\tau,\sigma,T)\frac{d\sigma_{kl}(\tau)}{d\tau}d\tau + \int_0^t \alpha_{ij}\frac{dT(\tau)}{d\tau}d\tau \end{aligned} \tag{2.5}$$

Equation (2.5) represents the general multi-axial constitutive equation for stress and temperature dependent nonlinear viscoelastic materials. This equation is valid under the assumption that the derivative of stress $\sigma_{ij}(t)$ is a continuous function of time with $\sigma_{ij}(t) = 0$ for $t < 0$. The compliance needs to satisfy the "fading memory" characteristic, in which the current strains depend more strongly on the recent stress-time history than the distant stress-time history. Hence the compliance $S_{ijkl}(t)$, its first time derivative, $dS_{ijkl}(t)/dt$, and 2nd time derivative, $d^2S_{ijkl}(t)/dt^2$, are continuous and non-negative in the interval $0 \le t < \infty$. This also indicates a monotonic nature of the compliance.

Halpin and Pagano [33] have presented an experimental procedure to characterize the time-dependent properties of an orthotropic material that obey material symmetry (Onsager reciprocity relations). The strain-stress relation similar to Eq. (2.5) was used with stress and temperature independent material properties. Lou and Schapery [47] have extended the Schapery nonlinear single integral form [74] to characterize time-stress dependent behaviors of orthotropic materials. In this study, the Schapery nonlinear integral model [74] and the extension to orthotropic materials (Lou and Schapery [47] is adopted and extended to multi-axial case for stress-temperature dependent properties for non-aging materials, which is written as:

$$\varepsilon_{ij}^{t} \equiv \varepsilon_{ij}(t) = g_0(\bar{\sigma}^t, T^t) S_{ijkl}^0 \sigma_{kl}^t + g_1(\bar{\sigma}^t, T^t) \int_0^t \Delta S_{ijkl}^{(\psi^t - \psi^\tau)} \frac{d[g_2(\bar{\sigma}^\tau, T^\tau)\sigma_{kl}^\tau]}{d\tau} d\tau + \int_0^t \alpha_{ij}(T^\tau) \frac{dT^\tau}{d\tau} d\tau \quad (2.6)$$

Here $S_{ijkl}^0(t)$ and $\Delta S_{ijkl}^t(t)$ are the instantaneous elastic and transient compliance, ψ^t is the reduced-time (effective time) given by:

$$\psi^t \equiv \psi(t) = \int_0^t \frac{d\xi}{a(\bar{\sigma}^\xi, T^\xi)} \qquad \psi^\tau \equiv \psi(\tau) = \int_0^\tau \frac{d\xi}{a(\bar{\sigma}^\xi, T^\xi)} \tag{2.7}$$

It is observed that Eq. (2.6) is a special form of Eq. (2.5) where the stress and temperature dependency of a viscoelastic material is carried through the nonlinear parameters g_0, g_1, g_2 and a. In this study, the nonlinear material parameters are modeled as functions of current effective stress $\bar{\sigma}^t$ and temperature T^t. The parameter g_0 measures the reduction or increase in elastic compliance due to stress and temperature. The nonlinearity introduced by g_0 is analogous to that present in the Ramberg-Osgood stress strain relationship (Ramberg and Osgood, [68] except that the nonlinearity is not restricted to a power-law relationship with strain hardening parameters. The parameter g_1 measures the nonlinearity effect in the transient compliance. Levesque et al. [46] has pointed out the restriction on the nonlinear parameters for a thermodynamically admissible extension of the one dimensional Schapery model to the multi-axial stress-strain relations. One of the requirements is that the parameter g_1 to be of a matrix form instead of a single 'equivalent stress dependent' scalar. Though this requirement is not considered in the formulation here, the results obtained are found to be satisfactory for multi-axial loading cases as will be verified later in this chapter. Moreover, the use of a single scalar provides with an ease of material characterization (no loss of material symmetry) as well as the numerical implementation without significant loss of accuracy. The parameter g_2 accounts for the loading rate effect on the time-dependent response. The parameter $a(\bar{\sigma}^t, T^t)$ is time shift (interchange) factors measured with respect to the reference stress and temperature. If the thermal effects are carried through the shift

factor $a(T^t)$ only, the thermo-rheologically simple material (TSM) is exhibited. The parameters T and T_0 are the current and reference temperatures respectively. The superscript denotes a dependent time variable. In general, the coefficient of thermal expansion α_{ij} is a material and temperature dependent. For simplicity, the nonlinear stress and temperature dependent material parameters will be written as:

$$\begin{aligned} g_\beta(\bar{\sigma}^t, T^t) &= g_\beta^t \quad \beta = 0,1,2 \\ a(\bar{\sigma}^t, T^t) &= a^t \qquad \bar{\sigma}^t = \sqrt{\frac{3}{2} S_{ij}^t S_{ij}^t} \end{aligned} \tag{2.8}$$

This constitutive model is applied independently for each component in the compliance matrix. The material symmetry conditions are imposed to the compliances, which give six independent time integral equations. A time integration algorithm, which uses a recursive approach, is formulated to solve these time integral constitutive equations. This algorithm is designed to be compatible with general FE structural analyses. The integrated structural (global) and material (local) levels requires to perform linearized solutions of the nonlinear constitutive equations and iterative schemes simultaneously at the local and global levels. The purpose of adding iterative schemes is to minimize errors arising from the linearization; otherwise very small time increments are required. Moreover, keeping time increments small is computationally expensive and it often leads to significant mismatch after several incremental steps have been performed due to the accumulated errors. The recursive-iterative time integration algorithm is discussed in the next section.

2.2 RECURSIVE-ITERATIVE TIME INTEGRATION ALGORITHM

The integrated global-local framework for the time integration algorithm is described as follows. At each global iteration within the incremental time-step $\Delta t^{(m)}$, trial incremental component of strain tensor $\Delta\varepsilon_{ij}^{t,(m)}$ and temperature $\Delta T^{(m)}$ are obtained from the structural level, given in Eq. (2.9). The superscript (m) denotes global iteration counter within the current incremental time step. The goal is to calculate current total stresses $\sigma_{ij}^{t,(m)}$ and material's consistent tangent stiffness $C_{ijkl}^{t,(m)}$ from given current variables and history variables stored at the previous converged solution at time $t-\Delta t$. The $\boldsymbol{Hist\_vars}^{\boldsymbol{t,(m)}}$ is a state variable tensor, which depends on the constitutive material models. The converged $C_{ijkl}^{t,(m)}$ after m global iteration at the current time t will be used to provide incremental trial strains for the next time step $t-\Delta t$. Due to the uncoupled thermo-mechanical problems, the trial incremental temperature is directly linked to the incremental time step. The procedure in Eq. (2.9) is performed at each material (Gaussian) integration point within elements at every structural iteration to achieve structural and material convergence simultaneously. Thus, an efficient and accurate numerical algorithm for solving the constitutive material model becomes necessary. For simplicity, the superscript (m) that indicates the global iteration counter will be ignored in the rest of this manuscript and the local iteration counter will be denoted by the superscript (k).

$$
\begin{aligned}
&\text{Input :} \quad \Delta\varepsilon_{ij}^{t,(m)}, \Delta T^{(m)}, \Delta t^{t,(m)} \quad m = \text{global iteration counter} \\
&\text{History :} \ \varepsilon_{ij}^{t-\Delta t}; \sigma_{ij}^{t-\Delta t}; T^{t-\Delta t}; \boldsymbol{Hist\_vars^{t,(m)}} \\
&\text{Compute :} \ \varepsilon_{ij}^{t,(m)} = \varepsilon_{ij}^{t-\Delta t} + \Delta\varepsilon_{ij}^{t,(m)} \quad T^{t,(m)} = T^{t-\Delta t} + \Delta T^{t,(m)} \\
&\qquad\qquad t^{(m)} = (t - \Delta t) + \Delta t^{(m)} \\
&\qquad\qquad \sigma_{ij}^{t,(m)} = \sigma_{ij}^{t-\Delta t} + \Delta\sigma_{ij}^{t,(m)} \quad \Delta\sigma_{ij}^{t,(m)} = f(\sigma_{ij}^{t,(m)}, T^{t,(m)}, \Delta\varepsilon_{ij}^{t,(m)}, Hist\_vars^{t-\Delta t}) \\
&\qquad\qquad C_{ijkl}^{t,(m)} = \frac{\partial\Delta\sigma_{ij}^{t,(m)}}{\partial\Delta\varepsilon_{ij}^{t,(m)}} \\
&\text{Output :} \quad \sigma_{ij}^{t,(m)}, C_{ijkl}^{t,(m)}, \boldsymbol{Hist\_vars^{t,(m)}}
\end{aligned}
\tag{2.9}
$$

The transient compliance in Eq. (2.6) follows the Prony series exponential form, which is:

$$\Delta S_{ijkl}^{\psi^t} = \sum_{n=1}^{N_{ijkl}} S_{ijkl(n)}(1 - \exp[-\lambda_{ijkl(n)}\psi^t]) \tag{2.10}$$

where N_{ijkl} is the number of terms for each component in the transient compliance tensor, $S_{ijkl(n)}$ is the nth coefficient of the Prony series for each component in the transient compliance tensor, and $\lambda_{ijkl(n)}$ is the nth reciprocal of retardation time that corresponds to the $S_{ijkl(n)}$.

Substituting Eq. (2.10) into Eq. (2.6) yields the following mechanical strain tensor:

$$\varepsilon_{ij}^t = g_0^t S_{ijkl}^0 \sigma_{kl}^t + g_1^t g_2^t \sum_{n=1}^{N_{ijkl}} S_{ijkl(n)} \sigma_{kl}^t - g_1^t \sum_{k=1}^{3}\sum_{l=1}^{3}\sum_{n=1}^{N_{ijkl}} \underbrace{S_{ijkl(n)} q_{ijkl(n)}^t}_{\text{no sum on } i \text{ and } j} \tag{2.11}$$

where

$$q_{ijkl(n)}^t = \int_0^t \exp[-\lambda_{ijkl(n)}(\psi^t - \psi^\tau)] \frac{d(g_2^\tau \sigma_{kl}^\tau)}{d\tau} d\tau \qquad \textit{(no sum on k and l)} \tag{2.12}$$

The $q_{ijkl(n)}^{t-\Delta t}$ parameter is the hereditary integral for every Prony term in each component of the compliance tensor. This is a history state variable stored from the last converged step at time ($t-\Delta t$). The history variables are updated at the end of each time increment.

Following Haj-Ali and Muliana [29], the integral form in Eq. (2.12) is solved recursively by dividing the integral into two parts. The first integral includes the limits ($0, t-\Delta t$), i.e. up to the previous converged time step, which is stored as history variables. The limits of the second integral are taken as ($t-\Delta t$, t), which is the current incremental step. Thus, Eq. (2.12) is written as:

$$q_{ijkl(n)}^{t} = \int_{0}^{t-\Delta t} \exp[-\lambda_{ijkl(n)}(\psi^{t}-\psi^{\tau})]\frac{d(g_2^{\tau}\sigma_{kl}^{\tau})}{d\tau}d\tau + \int_{t-\Delta t}^{t} \exp[-\lambda_{ijkl(n)}(\psi^{t}-\psi^{\tau})]\frac{d(g_2^{\tau}\sigma_{kl}^{\tau})}{d\tau}d\tau \quad (2.13)$$

The reduced time increment is defined by:

$$\Delta\psi^{t} \equiv \psi^{t} - \psi^{t-\Delta t} \quad (2.14)$$

Using the reduced time increment in Eq. (2.14) and solving the first integral part in Eq. (2.13) give:

$$\int_{0}^{t-\Delta t} \exp[-\lambda_{ijkl(n)}(\psi^{t}-\psi^{\tau})]\frac{d(g_2^{\tau}\sigma_{kl}^{\tau})}{d\tau}d\tau = \exp[-\lambda_{ijkl(n)}\Delta\psi^{t}]q_{ijkl(n)}^{t-\Delta t} \quad (2.15)$$

The second integral of Eq. (2.13) is solved by parts with an assumption of linear ($g_2^{\tau}\sigma_{kl}^{\tau}$) term over the current time increment (Δt), which gives $\frac{d^2 g_2^{t}\sigma_{ij}^{t}}{dt^2}=0$. Thus, at every incremental time Δt, the term $\frac{dg_2^{t}\sigma_{ij}^{t}}{dt}$ is obtained by $\frac{g_2^{t}\sigma_{ij}^{t} - g_2^{t-\Delta t}\sigma_{ij}^{t-\Delta t}}{\Delta t}$. It is also

assumed that the time shift parameter $a(\bar{\sigma}^t, T^t)$ is not directly a function of time. Therefore, the second integral can be reduced to:

$$\int_{t-\Delta t}^{t} \exp[-\lambda_{ijkl(n)}(\psi^t - \psi^\tau)] \frac{d(g_2^\tau \sigma_{kl}^\tau)}{d\tau} d\tau = \frac{1-\exp[-\lambda_{ijkl(n)}\Delta\psi^t]}{\lambda_{ijkl(n)}\Delta\psi^t}(g_2^t\sigma_{kl}^t - g_2^{t-\Delta t}\sigma_{kl}^{t-\Delta t}) \quad (2.16)$$

(no sum on k and l)

Substituting Eqs.(2.15) and Eq.(2.16) into Eq.(2.13), the hereditary integral can be written at the end of current time (t) as:

$$q_{ijkl(n)}^t = \exp[-\lambda_{ijkl(n)}\Delta\psi^t] q_{ijkl(n)}^{t-\Delta t} + \frac{1-\exp[-\lambda_{ijkl(n)}\Delta\psi^t]}{\lambda_{ijkl(n)}\Delta\psi^t}(g_2^t\sigma_{kl}^t - g_2^{t-\Delta t}\sigma_{kl}^{t-\Delta t}) \text{ (No sum on k and l)} \quad (2.17)$$

The strain at current time t is obtained by substituting Eq. (2.17) into Eq. (2.11) as:

$$\begin{aligned}\varepsilon_{ij}^t = {} & g_0^t S_{ijkl}^0 \sigma_{kl}^t + g_1^t g_2^t \sum_{n=1}^{N_{ijkl}} (S_{ijkl(n)}\sigma_{kl}^t) - g_1^t \sum_{k=1}^{3}\sum_{l=1}^{3}\sum_{n=1}^{N_{ijkl}} S_{ijkl(n)} \left[\exp\left[-\lambda_{ijkl(n)}\Delta\psi^t\right] q_{ijkl(n)}^{t-\Delta t}\right] \\ & - g_1^t \sum_{n=1}^{N_{ijkl}} \left[S_{ijkl(n)} \frac{1-\exp\left[-\lambda_{ijkl(n)}\Delta\psi^t\right]}{\lambda_{ijkl(n)}\Delta\psi^t} \left(g_2^t\sigma_{kl}^t - g_2^{t-\Delta t}\sigma_{kl}^{t-\Delta t}\right)\right]\end{aligned} \quad (2.18)$$

The strains in Eq. (2.18) can be written as:

$$\begin{aligned}\varepsilon_{ij}^t = {} & \left[g_0^t S_{ijkl}^0 + g_1^t g_2^t \sum_{n=1}^{N_{ijkl}} S_{ijkl(n)} - g_1^t g_2^t \sum_{n=1}^{N_{ijkl}} \left(S_{ijkl(n)} \frac{1-\exp\left[-\lambda_{ijkl(n)}\Delta\psi^t\right]}{\lambda_{ijkl(n)}\Delta\psi^t} \right) \right] \sigma_{kl}^t \\ & - \left[\sum_{k=1}^{3}\sum_{l=1}^{3}\sum_{n=1}^{N_{ijkl}} \underbrace{S_{ijkl(n)} \exp\left[-\lambda_{ijkl(n)}\Delta\psi^t\right] q_{ijkl(n)}^{t-\Delta t}}_{\text{no sum on i \& j}} - g_2^{t-\Delta t} \sum_{n=1}^{N_{ijkl}} S_{ijkl(n)} \frac{1-\exp\left[-\lambda_{ijkl(n)}\Delta\psi^t\right]}{\lambda_{ijkl(n)}\Delta\psi^t} \sigma_{kl}^{t-\Delta t} \right] \\ = {} & \bar{S}_{ijkl}^t \sigma_{kl}^t - A_{ij}^t\end{aligned} \quad (2.19)$$

where $\bar{S}_{ijkl}^t$ is the current effective compliance. Substituting $\exp\left[-\lambda_{ijkl(n)}\Delta\psi^t\right] q_{ijkl(n)}^{t-\Delta t}$ in Eq. (2.17) into A_{ij}^t in Eq. (2.19) gives:

$$A_{ij}^{t} = g_1^{t}\left[\sum_{k=1}^{3}\sum_{l=1}^{3}\sum_{n=1}^{N_{ijkl}}\underbrace{S_{ijkl(n)}q_{ijkl(n)}^{t-\Delta t}}_{\text{no sum on i \& j}} - g_2^{t}\sum_{n=1}^{N_{ijkl}}S_{ijkl(n)}\frac{1-\exp\left[-\lambda_{ijkl(n)}\Delta\psi^{t}\right]}{\lambda_{ijkl(n)}\Delta\psi^{t}}\sigma_{kl}^{t}\right] \tag{2.20}$$

The incremental formulation of strain can be obtained from Eq. (1), which is:

$$\Delta\varepsilon_{ij}^{t} = \varepsilon_{ij}^{t} - \varepsilon_{ij}^{t-\Delta t} = \left[\overline{S}_{ijkl}^{t}\sigma_{kl}^{t} + A_{ij}^{t}\right] + \left[\overline{S}_{ijkl}^{t-\Delta t}\sigma_{kl}^{t-\Delta t} + A_{ij}^{t-\Delta t}\right] \tag{2.21}$$

Using Eq. (2.20) the term A_{ij}^{t} - $A_{ij}^{t-\Delta t}$ in Eq. (2.21) is expressed as:

$$\begin{aligned}
A_{ij}^{t} - A_{ij}^{t-\Delta t} &= g_1^{t}\left[\sum_{k=1}^{3}\sum_{l=1}^{3}\sum_{n=1}^{N_{ijkl}}\underbrace{S_{ijkl(n)}q_{ijkl(n)}^{t}}_{\text{no sum on i \& j}} - g_2^{t}\sum_{n=1}^{N_{ijkl}}S_{ijkl(n)}\frac{1-\exp\left[-\lambda_{ijkl(n)}\Delta\psi^{t}\right]}{\lambda_{ijkl(n)}\Delta\psi^{t}}\sigma_{kl}^{t}\right] \\
&\quad - g_1^{t-\Delta t}\left[\sum_{k=1}^{3}\sum_{l=1}^{3}\sum_{n=1}^{N_{ijkl}}\underbrace{S_{ijkl(n)}q_{ijkl(n)}^{t-\Delta t}}_{\text{no sum on i \& j}} - g_2^{t-\Delta t}\sum_{n=1}^{N_{ijkl}}S_{ijkl(n)}\frac{1-\exp\left[-\lambda_{ijkl(n)}\Delta\psi^{t-\Delta t}\right]}{\lambda_{ijkl(n)}\Delta\psi^{t-\Delta t}}\sigma_{kl}^{t-\Delta t}\right] \\
&= \sum_{k=1}^{3}\sum_{l=1}^{3}\sum_{n=1}^{N_{ijkl}}\underbrace{S_{ijkl(n)}\left(g_1^{t-\Delta t} - g_1^{t}\exp\left[-\lambda_{ijkl(n)}\Delta\psi^{t}\right]\right)q_{ijkl(n)}^{t}}_{\text{no sum on i \&j}} \\
&\quad + g_2^{t-\Delta t}\sum_{n=1}^{N_{ijkl}}S_{ijkl(n)}\left[g_1^{t}\frac{1-\exp\left[-\lambda_{ijkl(n)}\Delta\psi^{t}\right]}{\lambda_{ijkl(n)}\Delta\psi^{t-\Delta t}} - g_1^{t-\Delta t}\frac{1-\exp\left[-\lambda_{ijkl(n)}\Delta\psi^{t-\Delta t}\right]}{\lambda_{ijkl(n)}\Delta\psi^{t-\Delta t}}\right]\sigma_{kl}^{t-\Delta t}
\end{aligned} \tag{2.22}$$

Thus, substituting Eq. (2.22) into (2.21) gives the current component of incremental strain tensor:

$$\begin{aligned}
\Delta\varepsilon_{ij}^{t} &= \left[\overline{S}_{ijkl}^{t}\sigma_{kl}^{t} - \overline{S}_{ijkl}^{t}\sigma_{kl}^{t-\Delta t}\right] + \sum_{k=1}^{3}\sum_{l=1}^{3}\sum_{n=1}^{N_{ijkl}}S_{ijkl(n)}\left(g_1^{t-\Delta t} - g_1^{t}\exp\left[-\lambda_{ijkl(n)}\Delta\psi^{t}\right]\right)q_{ijkl(n)}^{t} \\
&\quad + g_2^{t-\Delta t}\sum_{n=1}^{N_{ijkl}}S_{ijkl(n)}\left[g_1^{t}\frac{1-\exp\left[-\lambda_{ijkl(n)}\Delta\psi^{t}\right]}{\lambda_{ijkl(n)}\Delta\psi^{t-\Delta t}} - g_1^{t-\Delta t}\frac{1-\exp\left[-\lambda_{ijkl(n)}\Delta\psi^{t-\Delta t}\right]}{\lambda_{ijkl(n)}\Delta\psi^{t-\Delta t}}\right]\sigma_{kl}^{t-\Delta t}
\end{aligned} \tag{2.23}$$

Equations (2.19) and (2.23) define the current total and incremental strains, respectively. These equations can be used to determine the unknown stress for a given incremental strain and the history variables $q_{ijkl(n)}^{t-\Delta t}$ from the previous step at $(t-\Delta t)$. However, the nonlinear parameters in Eqs. (2.19) and (2.23) are expressed as functions

of current temperature and total stresses. The total stresses at the current time (t) are not known. Therefore, an iterative scheme is needed in order to find the correct stress. Linearized trial stress performed using Eqs. (2.19) or (2.23) is used as starting points in the iterative scheme. The chosen trial values (initial approximation solutions) and iterative method can significantly affect convergence. The Newton-Raphson's (NR) iterative method, which approximates a function with a linear tangent function to satisfy equilibrium conditions locally, is used. The NR's method can increase convergent process rapidly, however, linearized tangent functions often lead to divergence solutions if during the iteration process the convergence is not monotonic or if the magnitude of the tangent functions is very small (approaching zero). The initial approximation (trial) stress tensor is determined using the following approximation of nonlinear parameters:

$$\begin{aligned} g_\beta^{t,tr} &= g_\beta^{t,(0)} = g_\beta(\overline{\sigma}^{t-\Delta t}, T^{t-\Delta t}) \;\; \beta = 0,1,2 \\ a^{t,tr} &= a^{t,(0)} = a(\overline{\sigma}^{t-\Delta t}, T^{t-\Delta t}) \end{aligned} \tag{2.24}$$

The trial current component of stress tensor is formed based on the current known variables and history variables. Using the constitutive model in Eq. (2.23) and the current stress tensor defined in Eq. (2.1) gives the following trial stress:

$$\sigma_{ij}^{t,tr} = \sigma_{ij}^{t-\Delta t} + \Delta\sigma_{ij}^{t,tr}$$

$$\Delta\sigma_{ij}^{t,tr} = \left[\overline{S}_{ijkl}^{t-\Delta t}\right]^{-1}\left\{\Delta\varepsilon_{ij}^{t} - \sum_{k=1}^{3}\sum_{l=1}^{3}\sum_{n=1}^{N_{ijkl}} S_{ijkl(n)}\left(g_1^{t-\Delta t} - g_1^{t}\exp\left[-\lambda_{ijkl(n)}\Delta\psi^{t}\right]\right)q_{ijkl(n)}^{t}\right\} \tag{2.25}$$

The linearized approximation stress tensor in Eq. (2.25) is used to calculate the nonlinear parameters (g_0, g_1, g_2, and a) in Eqs. (2.19) and (2.23). This causes a mismatch between the calculated strain and the given strain. The component of residual tensor can

be defined by using either the incremental strains Eq. (2.23), or the total strains, Eq. (2.19). The residual tensor based on incremental strain is:

$$
\begin{aligned}
R_{ij}^{t} &= \left[\bar{S}_{ijkl}^{t}\sigma_{kl}^{t} - \bar{S}_{ijkl}^{t-\Delta t}\sigma_{kl}^{t-\Delta t} \right] + \sum_{k=1}^{3}\sum_{l=1}^{3}\sum_{n=1}^{N_{ijkl}} \underbrace{S_{ijkl(n)}\left(g_1^{t-\Delta t} - g_1^{t}\exp\left[-\lambda_{ijkl(n)}\Delta\psi^{t} \right] \right) q_{ijkl(n)}^{t-\Delta t}}_{\text{no sum on i \& j}} \\
&+ g_2^{t-\Delta t}\sum_{n=1}^{N_{ijkl}} S_{ijkl(n)} \left[g_1^{t}\frac{1-\exp\left[-\lambda_{ijkl(n)}\Delta\psi^{t} \right]}{\lambda_{ijkl(n)}\Delta\psi^{t-\Delta t}} - g_1^{t-\Delta t}\frac{1-\exp\left[-\lambda_{ijkl(n)}\Delta\psi^{t-\Delta t} \right]}{\lambda_{ijkl(n)}\Delta\psi^{t-\Delta t}} \right] \sigma_{kl}^{t-\Delta t} \qquad (2.26) \\
&- \Delta\varepsilon_{ij}^{t} \\
R_{ij}^{t} &= \left[\bar{S}_{ijkl}^{t}\sigma_{kl}^{t} - \bar{S}_{ijkl}^{t-\Delta t}\sigma_{kl}^{t-\Delta t} \right] + B_{ij}^{t} + D_{ij}^{t} - \Delta\varepsilon_{ij}^{t}
\end{aligned}
$$

Variable B_{ij}^{t} contains the history variables and variable D_{ij}^{t} is the third term of the residual vector. The current incremental strain $\Delta\varepsilon_{ij}^{t} \equiv \Delta\varepsilon_{ij}^{t(m)}$ in Eq. (2.26) is obtained from the structural level at the mth global iteration. The NR iterative method is used to correct for the trial stress and minimize residual strains. This requires defining the Jacobian tensor by taking the derivative of the residual tensor in Eq. (2.26) with respect to the incremental stress as:

$$
\frac{\partial R_{ij}^{t}}{\partial\Delta\sigma_{kl}^{t}} = \bar{S}_{ijkl}^{t} + \frac{\partial\bar{S}_{ijkl}^{t}}{\partial\Delta\sigma_{kl}^{t}}\sigma_{kl}^{t} + \frac{\partial B_{ij}^{t}}{\partial\Delta\sigma_{kl}^{t}} + \frac{\partial D_{ij}^{t}}{\partial\Delta\sigma_{kl}^{t}} \qquad (2.27)
$$

The derivation in the second, third and fourth terms in Eq. (27) are defined by:

$$
\begin{aligned}
\frac{\partial\bar{S}_{ijkl}^{t}}{\partial\Delta\sigma_{kl}^{t}} = \Bigg\{ &\frac{\partial g_0^{t}}{\partial\bar{\sigma}^{t}} S_{ijkl}^{0} + \left(\frac{\partial g_1^{t}}{\partial\bar{\sigma}^{t}} g_2^{t} + g_1^{t}\frac{\partial g_2^{t}}{\partial\bar{\sigma}^{t}} \right) \sum_{n=1}^{N_{ijkl}} S_{ijkl(n)} \left(1 - \frac{1-\exp\left[-\lambda_{ijkl(n)}\Delta\psi^{t} \right]}{\lambda_{ijkl(n)}\Delta\psi^{t}} \right) \\
&+ g_1^{t}g_2^{t}\frac{\partial \mathrm{a}^{t}}{\partial\bar{\sigma}^{t}} \sum_{n=1}^{N_{ijkl}} S_{ijkl(n)} \left[\frac{\exp\left[-\lambda_{ijkl(n)}\Delta\psi^{t} \right] - 1}{\lambda_{ijkl(n)}\Delta t} + \frac{\exp\left[-\lambda_{ijkl(n)}\Delta\psi^{t} \right]}{\mathrm{a}^{t}} \right] \Bigg\} \frac{\partial\bar{\sigma}^{t}}{\partial\Delta\sigma_{kl}^{t}}
\end{aligned} \qquad (2.28)
$$

$$\frac{\partial B_{ij}^{t}}{\partial \Delta\sigma_{kl}^{t}} = -\sum_{n=1}^{N_{ijkl}} S_{ijkl(n)} \exp\left[-\lambda_{ijkl(n)}\Delta\psi^{t}\right]\left(\frac{\partial \mathrm{g}_1^{t}}{\partial \bar{\sigma}^{t}} + g_1^{t}\lambda_{ijkl(n)}\frac{\Delta t}{(\mathrm{a}^{t})^{2}}\frac{\partial \mathrm{a}^{\mathrm{t}}}{\partial \bar{\sigma}^{t}}\right)\frac{\partial \bar{\sigma}^{t}}{\partial \Delta\sigma_{kl}^{t}} q_{ijkl(n)}^{t-\Delta t} \tag{2.29}$$

$$\begin{aligned}\frac{\partial D_{ij}^{t}}{\partial \Delta\sigma_{kl}^{t}} = g_2^{t-\Delta t}\sum_{n=1}^{N_{ijkl}} S_{ijkl(n)}\Bigg\{&\left(\frac{\partial \mathrm{g}_1^{t}}{\partial \bar{\sigma}^{t}} + \frac{g_1^{t}}{\mathrm{a}^{t}}\frac{\partial \mathrm{a}^{t}}{\partial \bar{\sigma}^{t}}\right)\frac{1-\exp\left[-\lambda_{ijkl(n)}\Delta\psi^{t}\right]}{\lambda_{ijkl(n)}\Delta\psi^{t}} \\ &-\frac{g_1^{t}}{\mathrm{a}^{t}}\frac{\partial \mathrm{a}^{t}}{\partial \bar{\sigma}^{t}}\exp\left[-\lambda_{ijkl(n)}\Delta\psi^{t}\right]\Bigg\}\sigma_{kl}^{t-\Delta t}\frac{\partial \bar{\sigma}^{t}}{\partial \Delta\sigma_{kl}^{t}}\end{aligned} \tag{2.30}$$

where the term $\dfrac{\partial \Delta\bar{\sigma}^{t}}{\partial \Delta\sigma_{kl}^{t}} = \dfrac{3}{2}\dfrac{S_{ij}^{t}}{\Delta\sigma_{kl}^{t}}\left(\delta_{ik}\delta_{jl} - \dfrac{1}{3}\delta_{ij}\delta_{kl}\right)$

Next, the consistent tangent stiffness matrix is calculated by taking the inverse of the partial derivative of the incremental strain with respect to the incremental stress at the end of the current time step. Using Eq. (2.27), the consistent tangent stiffness, C_{ijkl}^{t} at the converged state, is:

$$C_{ijkl}^{t} \equiv \frac{\partial \Delta\bar{\sigma}_{ij}^{t}}{\partial \Delta\varepsilon_{kl}^{t}} = \left[\frac{\partial R_{ij}^{t}}{\partial \Delta\sigma_{kl}^{t}}\right]^{-1}; \left\|R_{ij}^{t}\right\| \longrightarrow 0 \tag{2.31}$$

Another iterative method, which is fixed point (FP) method, can also be used in the stress update algorithm. The initial approximation (trial) stress is determined using Eq. (2.25) with trial nonlinear parameters are defined in Eq. (2.24). During the iteration, the component of residual tensor is expressed in terms of the total stress:

$$R_{ij}^{t,(k+1)} = \sigma_{ij}^{t,(k+1)} - \sigma_{ij}^{t,(k)} \tag{2.32}$$

where (k) indicates the local iteration counter and the current stress at the iteration (k+1) is defined using Eq. (2.19) as:

$$\sigma_{ij}^{t,(k+1)} = \left[\bar{S}^{t,(k)}_{ijkl} \right]^{-1} \left(\varepsilon_{ij}^{t} + A_{ij}^{t,(k)} \right) \tag{2.33}$$

The nonlinear parameters in Eq. (2.33) is defined by $g_{\beta}^{t,(k)} = g_{\beta}(\bar{\sigma}^{t,(k)}, T^{t})$ and $a^{t,(k)} = a(\bar{\sigma}^{t,(k)}, T^{t})$. Once convergence is achieved, the consistent tangent stiffness matrix in Eq. (2.34), the current stress, and history variables in Eqs. (2.17) are updated and sent to the structural level.

$$C_{ijkl}^{t} = \frac{\partial \sigma_{ij}^{t}}{\partial \varepsilon_{kl}^{t}} = \left[\bar{S}_{ijkl}^{t} \right]^{-1} \tag{2.34}$$

The complete numerical algorithm, which is used to provide the correct stress and its corresponding nonlinear parameters for a given strain increment, is summarized in Fig. 2.1.

1. Input variables: (at the mth global iteration)

$\varepsilon_{ij}^{t-\Delta t}, \Delta\varepsilon_{ij}^{t,(m)}, \Delta t^{(m)}, \Delta t^{t,(m)}$ History: $\sigma_{ij}^{t-\Delta t}, T_{ij}^{t-\Delta t}, q_{ijkl(n)}^{t-\Delta t}$

2. Initial approximation variables:

$g_{\beta}^{t,tr} = g_{\beta}(\sigma^{t-\Delta t}, T^{t-\Delta t})$ β=0,1,2, $a^{t,tr} = a(\sigma^{t-\Delta t}, T^{t-\Delta t})$

$S_{ijkl}^{t,tr} = S_{ijkl}^{t}(g_{\beta}^{t,tr}, a^{t,tr})$

$\Delta\sigma_{ij}^{t,tr} = \Delta\sigma_{ij}^{t,tr}(\Delta S_{ij}^{t,tr}, \Delta\sigma_{kk}^{t,tr})$ $\sigma_{ij}^{t,(0)} = \sigma_{ij}^{t-\Delta t} + \Delta\sigma_{ij}^{t,tr}$

3. Iterate for k=1,2,3 …. (k = local iteration counter)

3.1 Compute nonlinear parameters:

$g_{\beta}^{t,(k)} = g_{\beta}(\sigma^{t,(k)}, T^{t,(m)})$ β=0,1,2, $\mathrm{a}^{t,(k)} = \mathrm{a}(\sigma^{t,(k)}, T^{t,(m)})$

where $T^{t,(m)} = T^{t-\Delta t} + \Delta\sigma^{t,(m)}$

3.2 Compute stress correction:

NR method:

$$\Delta\sigma_{ij}^{t,(k+1)} = \Delta\sigma_{ij}^{t,k} + \left[\frac{\partial R_{ij}^{t,(k)}}{\partial\Delta\sigma_{kl}}\right]^{-1} R_{kl}^{t,(k)} \qquad \sigma_{ij}^{t,(k+1)} = \sigma_{ij}^{t-\Delta t} + \Delta\sigma_{ij}^{t,(k+1)}$$

FP method:

$\sigma_{ij}^{t,(k+1)} = f(\sigma_{ij}^{t,(k)}, \varepsilon_{ij}^{t,(m)}, T^{t,(m)})$ where $\varepsilon_{ij}^{t,(m)} = \varepsilon_{ij}^{t-\Delta t} + \Delta\varepsilon_{ij}^{t,(m)}$

3.3 Evaluate residual tensor:

NR method:

$$R_{ij}^{t,(k+1)} = \left[S_{ijkl}^{t,(k+1)}\sigma_{kl}^{t,(k+1)} - S_{ijkl}^{t-\Delta t}\sigma_{kl}^{t-\Delta t}\right] + B_{ij}^{t,(k+1)} + D_{ij}^{t,(k+1)} - \Delta\varepsilon_{ij}^{t,(m)}$$

FP method:

$R_{ij}^{t,(k+1)} = \sigma_{ij}^{t,(k+1)} - \sigma_{ij}^{t,(k)}$

IF $\left\|R_{ij}^{t,(k+1)}\right\| \le Tol$ THEN GOTO 4 and EXIT

ELSE GOTO 3

4 Update stress, consistent tangent stiffness, and history variables:

$\sigma_{ij}^{t} \leftarrow \sigma_{ij}^{t,(k+1)}$ C_{ijkl}^{t} $q_{ijkl(n)}^{t} \leftarrow q_{ijkl(n)}^{t,(k+1)}$

Fig. 2.1 Recursive-iterative algorithm for nonlinear orthotropic viscoelastic material

2.3 VERIFICATION OF THE NUMERICAL ALGORITHM

The proposed numerical algorithm of nonlinear orthotropic viscoelastic constitutive model is implemented at each material point (Gaussian integration point) within the 3D continuum elements. The material subroutine (UMAT) of the ABAQUS FE code is used. Thermo-mechanical viscoelastic test data on Kevlar/epoxy laminated composites reported by Walruth [83], glass/epoxy laminated composites reported by Lou and Schapery [47], glass/vinylester multilayered composites of Muliana et al. [57] and FM-73 epoxy resin of Peretz & Weitsman [63] are used to validate the proposed numerical algorithm. The experimental tests were performed under different thermo-mechanical loading histories.

2.3.1 Viscoelastic responses of Kevlar/epoxy composites

The recursive iterative algorithm is verified using creep data on Kevlar/epoxy composites. For Kevlar composites, a viscoelastic behavior is observed in the fiber direction as well due to the viscoelastic response of Kevlar fiber. Hence a time dependant behavior is observed in all the principle directions of a unidirectional lamina. Walruth [83] tested viscoelastic responses of a unidirectional Kevlar/epoxy composite. Five time dependant material properties for a transversely isotropic lamina are reported. Monotonic testing was also carried out to characterize composite elastic moduli and strengths in the material principle directions. The shear response was measured using the Iosipescu shear method. The effective elastic properties for Kevlar/epoxy are given

in Table 2.1. The calibrated prony parameters for each principal compliance are given in Table 2.2.

Table 2.1 Elastic properties for Kevlar/epoxy

Modulus (MPa)				Poisson's ratio	
E_{11}	$E_{22}=E_{33}$	$G_{12}=G_{13}$	G_{23}	$\nu_{12}=\nu_{13}$	ν_{23}
83420	5720	2954	1900	0.4	0.59

Table 2.2 Prony parameters for Kevlar/epoxy system

N	λn (1/s)	Dn x 10^{-6} (1/MPa)		
		S_{1111}	S_{2222}	S_{1212}
1	1	1	35	100
2	10^{-1}	1	2.5	5.8
3	10^{-2}	0.9	10	25
4	10^{-3}	0.36	11	25
5	10^{-4}	0.48	11	20
6	10^{-5}	0.6	19	25

Response for various off-axis angles is not reported in Walruth [83]; however, the off-axis compliance S_θ is computed using the following transformation:

$$S_\theta = S_{1111}\cos^4\theta + 2S_{1122}\sin^2\theta\cos^2\theta + S_{2222}\sin^4\theta + S_{1212}\sin^2\theta\cos^2\theta \tag{2.35}$$

Numerical verifications are first performed for fiber angles of 0° and 90°. The numerical predictions for 30°, 45°, 60° fiber angles are also obtained at a stress of $0.1S_{ut}^{\theta}$. The ultimate strength for each off-axis fiber, S_{ut}^{θ}, is obtained using the stress transformation equation:

$$S_{ut}^{\theta} = S_{ut11}cos^2\theta + S_{ut22}sin^2\theta + S_{ut12}sin\theta cos\theta \tag{2.36}$$

The reported values of S_{ut11}, S_{ut22} and S_{ut12} are 1340, 13.8, and 80.6 MPa, respectively. Excellent agreements between the numerical and fitted experimental responses are obtained, as shown in Fig. 2.2. This verifies the numerical algorithm for linear viscoelastic responses.

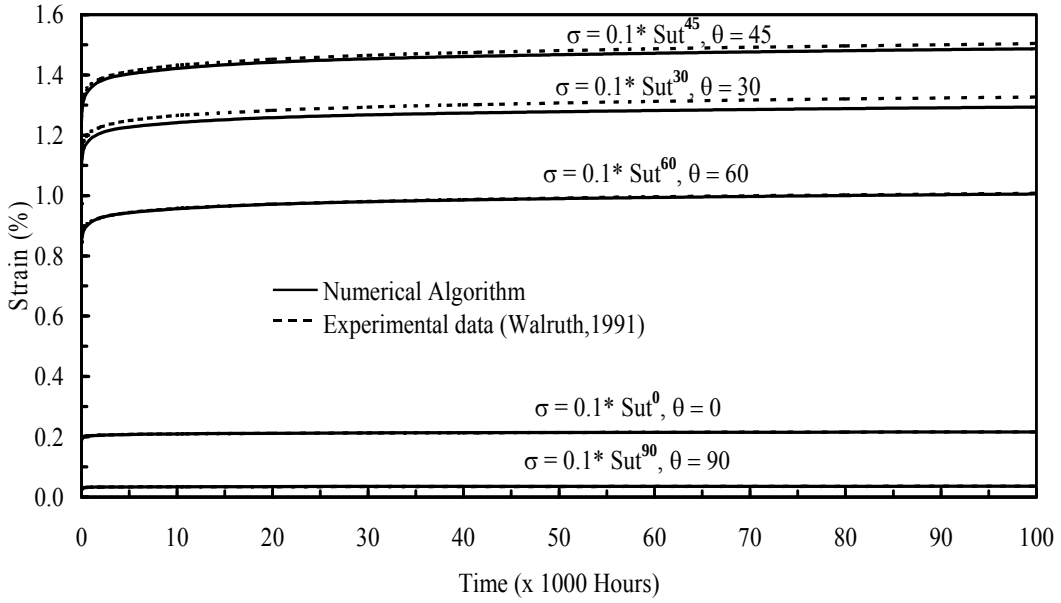

Fig. 2.2 Creep strain response for Kevlar/epoxy composite for θ = 0°, 30°, 45°, 60° & 90° at σ=$0.1S_{ut}^{\theta}$

2.3.2 Nonlinear viscoelastic response of glass/epoxy laminated composites

The creep data for glass/epoxy off-axis coupon reported by Lou and Schapery [47] is used to verify the proposed numerical algorithm for stress dependent nonlinear viscoelastic behaviors. Composite specimens with different fiber orientations: 0°, 30°, 45°, 60°, and 90° were tested at fixed environmental conditions: 164°F and 21% humidity. The orthotropic effective elastic properties are given in Table 2.3. The nonlinear material properties (g_0, g_1, g_2, and a) are stress dependent, which are expressed as functions of an average effective stress. All temperature dependant nonlinear parameters are taken as unity. For the numerical implementation, the time-dependent model given in Eq. (2.10) is used. The fitted Prony parameters for the transverse and shear compliances are given in Table 2.4.

Table 2.3 Elastic properties for glass/epoxy

Modulus (ksi)				Poisson's ratio	
E_{11}	$E_{22}=E_{33}$	$G_{12}=G_{13}$	G_{23}	$\nu_{12}=\nu_{13}$	ν_{23}
5435	1538	622.5	437.5	0.31	0.35

Table 2.4 Prony parameters for glass/epoxy system

N	λn (1/min)	Dn x 10^{-6} (1/ksi)	
		S_{2222}	S_{1212}
1	1	0.08	0.065
2	10-1	0.067	0.6
3	10-2	0.0305	0.11
4	10-3	0.215	1.0
5	10-4	0.31	0.9
6	10-5	0.78	6

The above composite systems follow transversely isotropic materials, so that $S_{3333}(t) = S_{2222}(t) = S_{1313}(t) = S_{1212}(t)$. It was also reported that in fiber directions, the time-dependent effects were negligible. Since there is no available experimental data for $S_{2323}(t)$, therefore the $S_{2323}(t)$ term is taken as time-independent. The nonlinear stress-dependent parameters in Eq. (2.5) are functions of effective stress, which are:

$$\begin{aligned} g_0 &= 0.04\bar{\sigma} + 0.9304 \\ g_1 &= 0.0035\bar{\sigma}^3 - 0.0661\bar{\sigma}^2 + 0.4186\bar{\sigma} + 0.2727 \\ g_2 &= -0.00466\bar{\sigma}^3 - 0.0991\bar{\sigma}^2 + 0.6286\bar{\sigma} + 1.9146 \\ a_\sigma &= 2.899e^{-0.5652\bar{\sigma}} \end{aligned} \tag{2.37}$$

Using the time-dependent and nonlinear material parameters in Table 2.2 and Eq. (2.37), respectively, numerical predictions of creep responses for off-axis composite systems having 30°, 45°, 60°, and 90° angles are performed, illustrated in Figs. 2.3-2.6. The responses are shown at different stresses that indicate both linear and nonlinear

ranges. Good agreements between the numerical and experimental responses are shown. The linear viscoelastic behaviors are shown for all cases under load 1ksi.

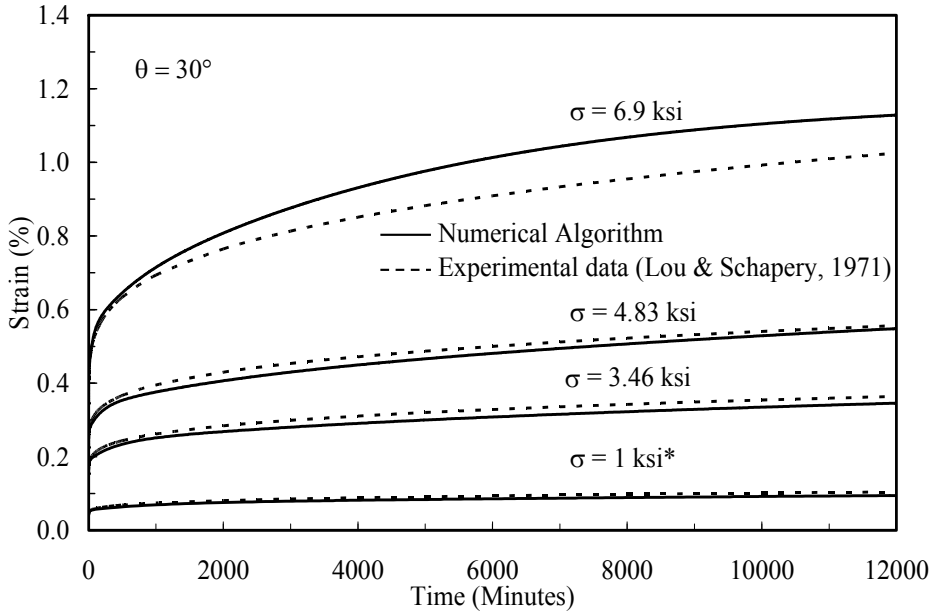

Fig. 2.3 Creep strain response for glass/epoxy ($\theta = 30°$)

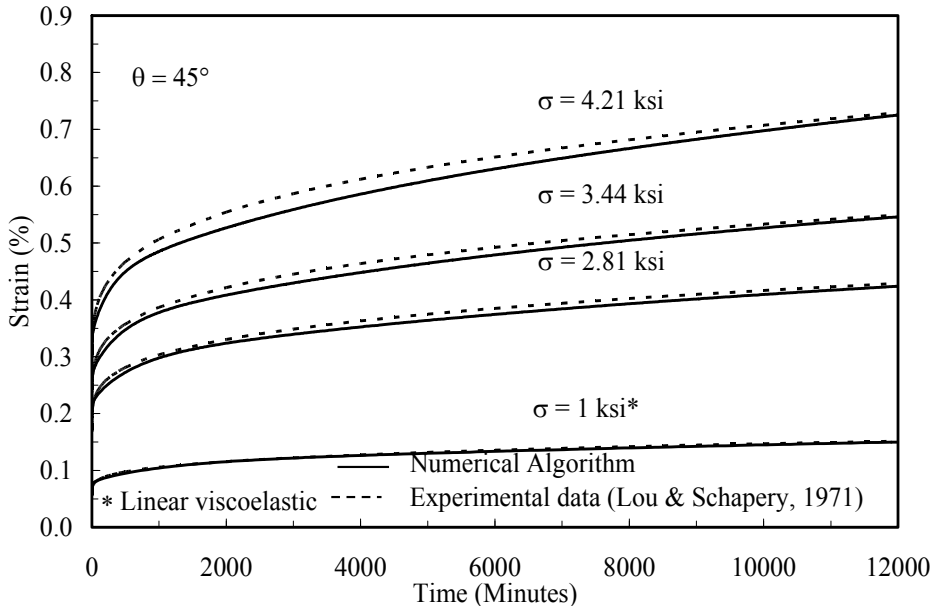

Fig. 2.4 Creep strain response for glass/epoxy ($\theta = 45°$)

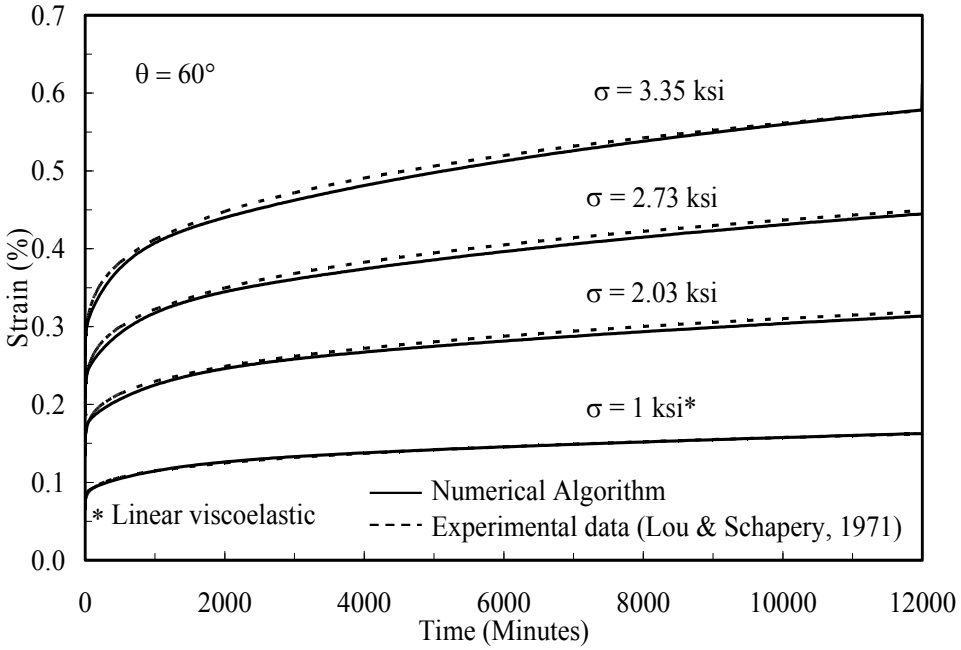

Fig. 2.5 Creep strain response for glass/epoxy ($\theta = 60°$)

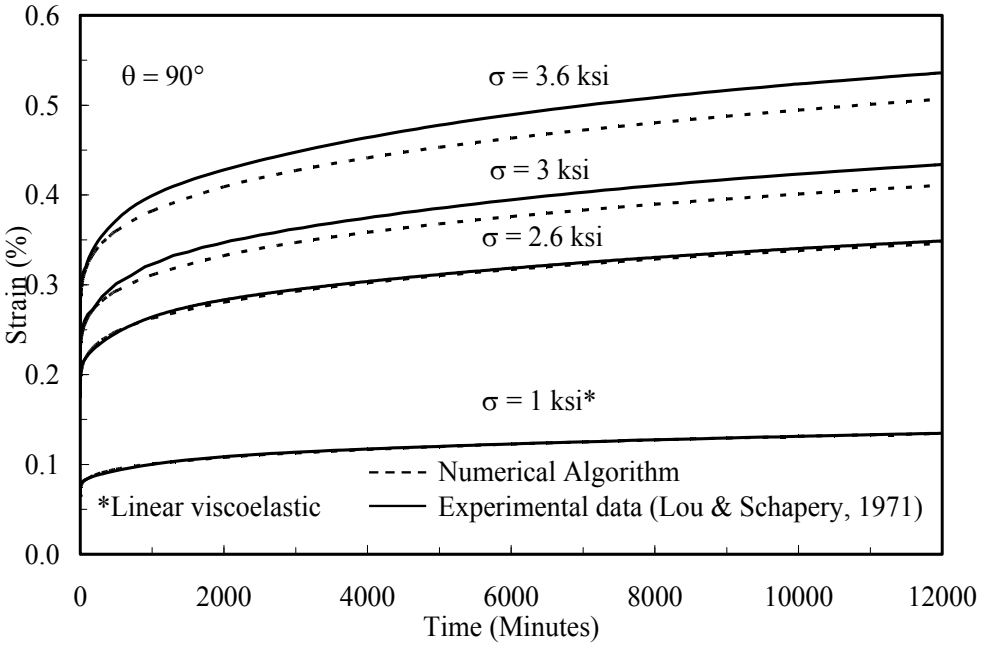

Fig. 2.6 Creep strain response for glass/epoxy ($\theta = 90°$)

2.3.3 Nonlinear viscoelastic response of glass/vinylester multi-layered composites

The creep data for glass/vinylester off-axis multi-layered specimens reported by Muliana et al. [57] is also used to verify the proposed numerical algorithm for combined stress and temperature dependent nonlinear behavior. The creep tests were performed for specimens with fiber orientations of 0°, 45° and 90° at various temperature and stress levels for 30 minutes. The stress levels were $0.2\,S_{ut}^{\theta}$, $0.4\,S_{ut}^{\theta}$ and $0.6\,S_{ut}^{\theta}$ (S_{ut}^{θ} is the ultimate compressive strength of specimen for fiber angle θ) and the temperatures were 75°F, 100°F, 125°F and 150°F. The orthotropic elastic properties for glass/vinylester are given in Table 2.5. The Prony parameters for principal compliances i.e. the axial, transverse and shear compliances are given in Table 2.6. The nonlinear stress-dependent parameters are modeled as functions of effective stress and temperature as given in Table 2.7.

Table 2.5 Elastic properties for glass/vinylester system

Modulus (MPa)				Poisson's ratio	
E_{11}	$E_{22}=E_{33}$	$G_{12}=G_{13}$	G_{23}	$\nu_{12}=\nu_{13}$	ν_{23}
19268	13210	4572	3700	0.31	0.35

Table 2.6 Prony parameters for glass/ vinylester system

N	λn (1/s)	Dn x 10^{-6} (1/MPa)		
		S_{1111}	S_{2222}	S_{1212}
1	1	1	0.3	0.9
2	10^{-1}	0.8	5.5	0.8
3	10^{-2}	0.25	1.8	5.8
4	10^{-3}	0.28	1.8	8
5	10^{-4}	0.05	1.9	13.8

Table 2.7 Stress and temperature dependent nonlinear parameters for glass/vinylester system

θ^o	$g_i(\sigma)$	Effective Stress dependency	$g_i(T)$	Temperature dependency
0°	$g_0(\sigma)$	$0.977e^{4.756\times10^{-4}\bar{\sigma}}$	$g_0(T)$	$-1.124\times10^{-5}T^2+3.71\times10^{-3}T+0.79$
	$g_1(\sigma)$	$-9.92\times10^{-5}\bar{\sigma}^2+2.524\times10^{-2}\bar{\sigma}-0.091$	$g_1(T)$	1
	$g_2(\sigma)$	$-5.866\times10^{-5}\bar{\sigma}^2+2.64\times10^{-2}\bar{\sigma}-0.281$	$g_2(T)$	$-9.94\times10^{-5}T^2+5.58\times10^{-2}T-2.63$
45°	$g_0(\sigma)$	$0.929e^{2.24\times10^{-3}\bar{\sigma}}$	$g_0(T)$	$2.86\times10^{-3}T+0.793$
	$g_1(\sigma)$	$-3.156\times10^{-5}\bar{\sigma}^2+1.0356\times10^{-2}\bar{\sigma}+0.692$	$g_1(T)$	1
	$g_2(\sigma)$	$9.48\times10^{-5}\bar{\sigma}^2+5.07\times10^{-4}\bar{\sigma}+0.913$	$g_2(T)$	$4.89\times10^{-6}T^3-1.24\times10^{-3}T^2$ $+0.107T-2.122$
90°	$g_0(\sigma)$	$0.955e^{1.399\times10^{-3}\bar{\sigma}}$	$g_0(T)$	$1.57\times10^{-3}T+0.885$
	$g_1(\sigma)$	$4.567\times10^{-5}\bar{\sigma}^2-5.84\times10^{-3}\bar{\sigma}+1.143$	$g_1(T)$	1
	$g_2(\sigma)$	$-2.04\times10^{-4}\bar{\sigma}^2+3.506\times10^{-2}\bar{\sigma}+0.063$	$g_2(T)$	$6.63\times10^{-5}T^2-2.55\times10^{-3}T+0.818$
Avg.	$g_0(\sigma)$	$1.0045e^{5.655\times10^{-4}\bar{\sigma}}$	$g_0(T)$	$1.872\times10^{-3}T+0.866$
	$g_1(\sigma)$	$3.55\times10^{-3}\bar{\sigma}+0.878$	$g_1(T)$	1
	$g_2(\sigma)$	$9.83\times10^{-6}\bar{\sigma}^2+9.77\times10^{-3}\bar{\sigma}+0.636$	$g_2(T)$	$1.259\times10^{-4}T^2-6.37\times10^{-3}T+0.77$

The numerical verifications are performed at different combinations of constant stress and constant temperature. Figs. 2.7-2.9 show the comparison of creep strains for various stress levels at temperature of 75F for 0°, 45° and 90° specimens, respectively. The temperature dependant nonlinear parameters are unity. The responses using the actual nonlinear parameters for 0°, 45° and 90° and the responses obtained using the

averaged nonlinear parameters are compared with the experimental data. Both the results show good correlation with the experimental data.

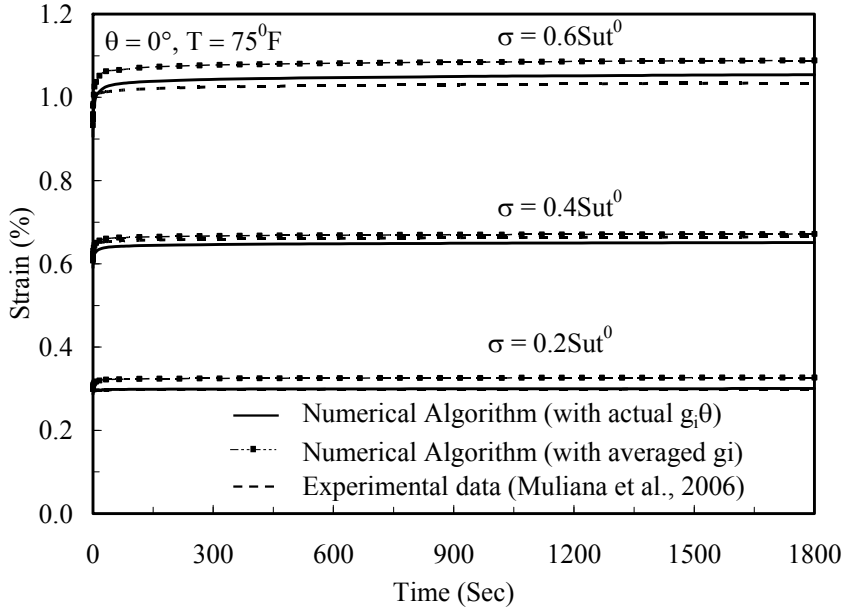

Fig. 2.7 Creep strain response for glass/vinylester ($\theta = 0°$) at different stresses at 75F

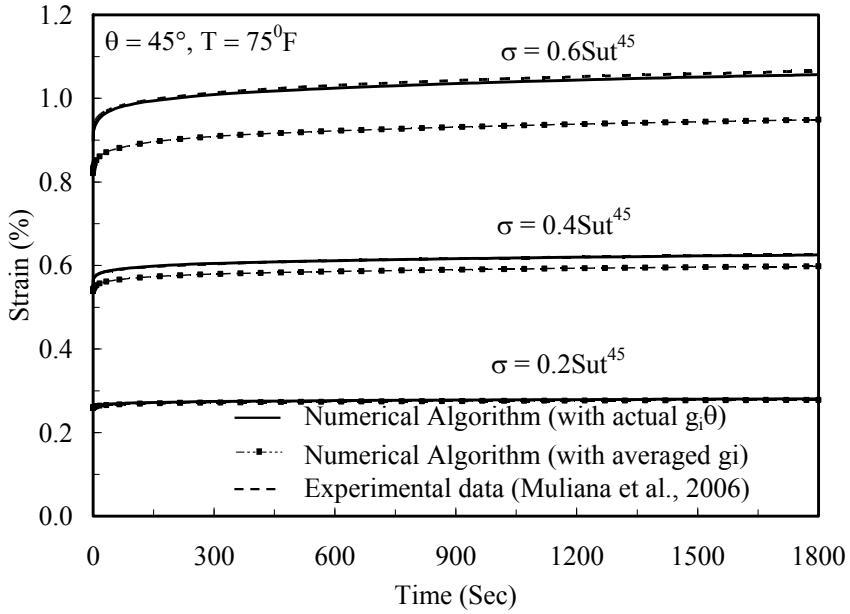

Fig. 2.8 Creep strain response for glass/vinylester ($\theta = 45°$) at different stresses at 75F

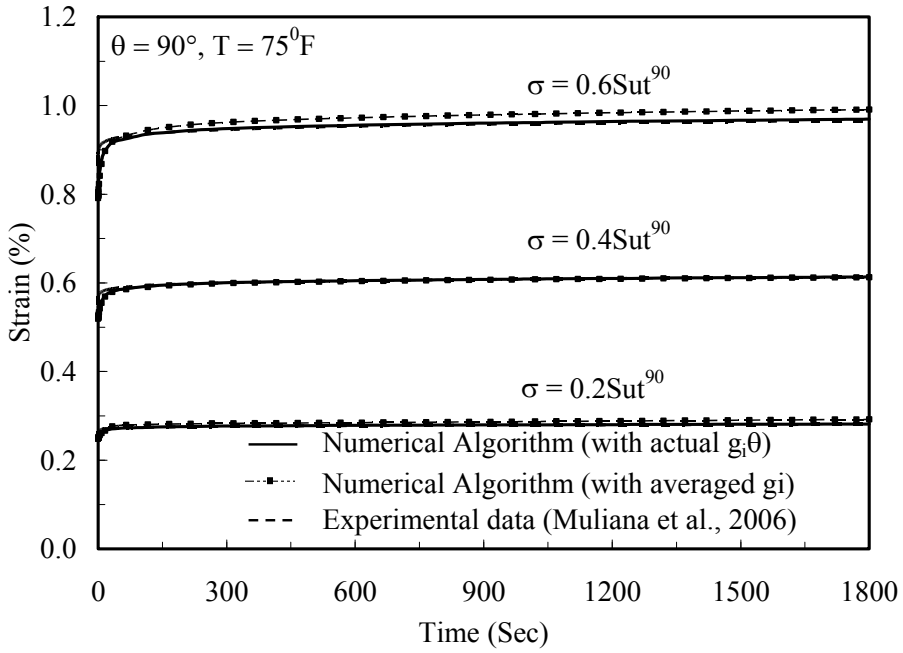

Fig. 2.9 Creep strain response for glass/vinylester ($\theta = 90°$) at different stresses at 75F

Figs. 2.10 to 2.12 show the responses for stress level of 0.2 S_{ut}^{θ} at various temperature levels. The stress dependant nonlinear parameters in this case are unity. The actual temperature dependant nonlinear parameters for 0°, 45° and 90° are used. The results indicate that the algorithm is able to predict the response under temperature loading.

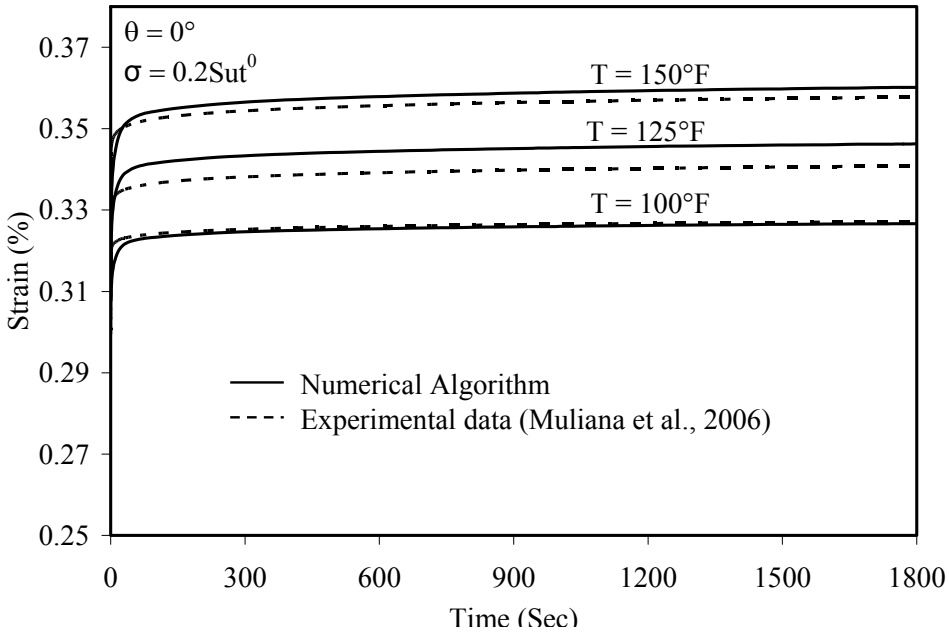

Fig. 2.10 Creep strain response for glass/vinylester (θ = 0°) at several temperatures and σ=0.2Sut^{0}

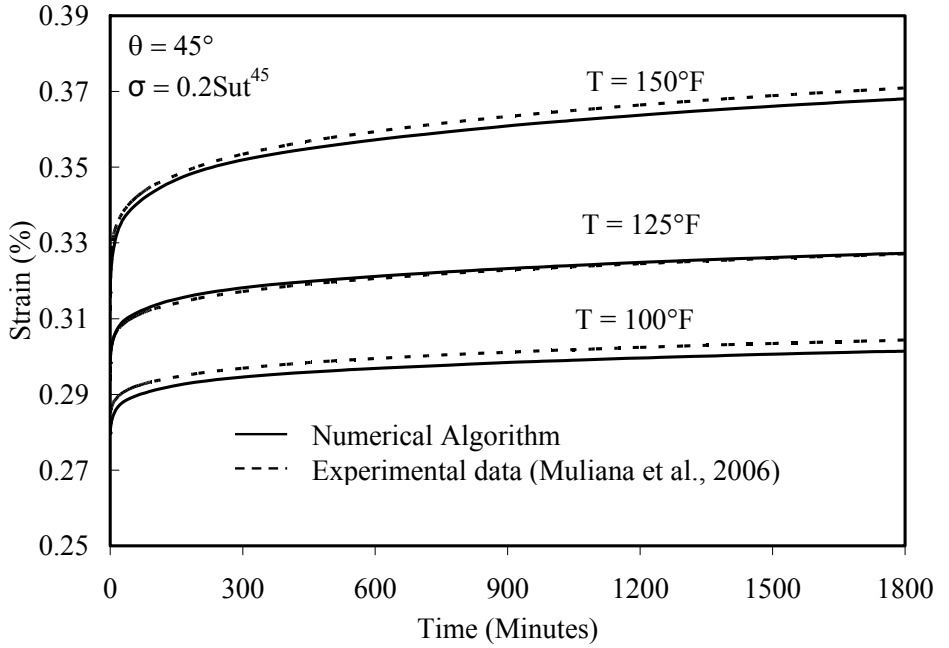

Fig. 2.11 Creep strain response for glass/vinylester (θ = 45°) at several temperatures and σ = 0.2Sut^{45}

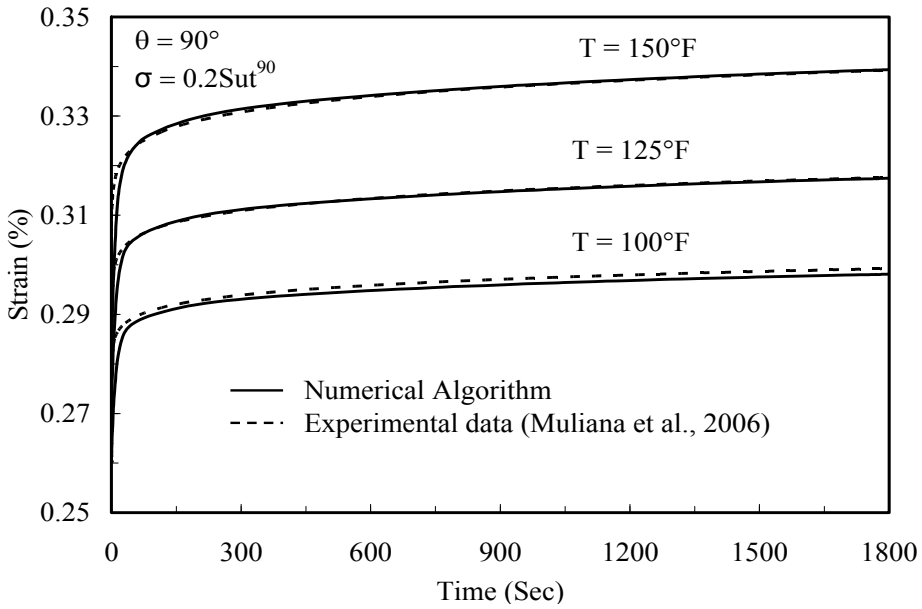

Fig. 2.12 Creep strain response for glass/vinylester ($\theta = 90°$) at several temperatures and $\sigma = 0.2Sut^{90}$

Figs. 2.13-2.16 show the creep responses at higher stress levels and several temperatures for the 45° and 90° specimens. The stress as well as the temperature dependant nonlinear parameters is not equal to one for these cases. Good agreements between the numerical and experimental results are observed.

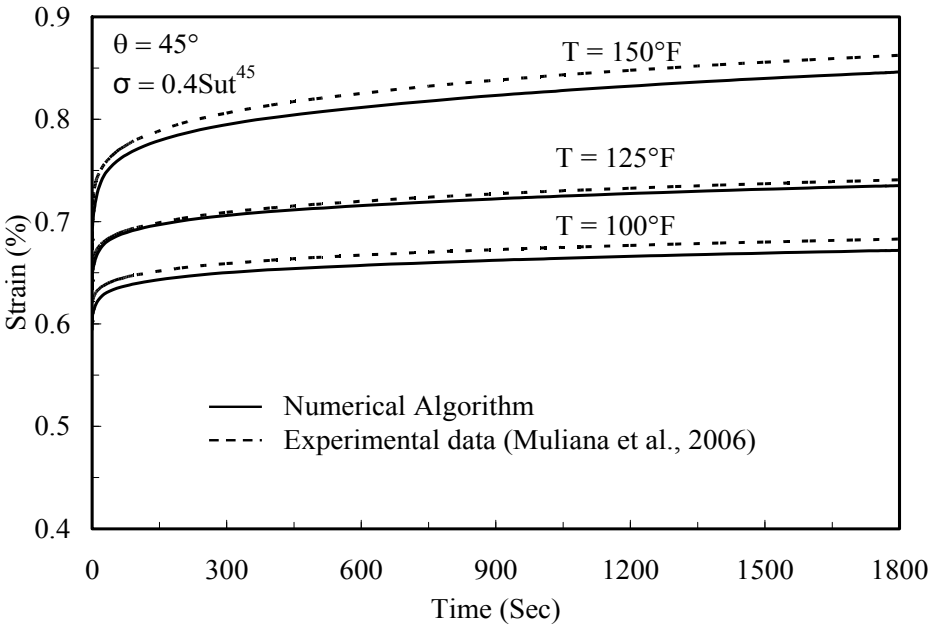

Fig. 2.13 Creep strain response for glass/vinylester ($\theta = 45°$) at several temperatures and $\sigma = 0.4Sut^{45}$

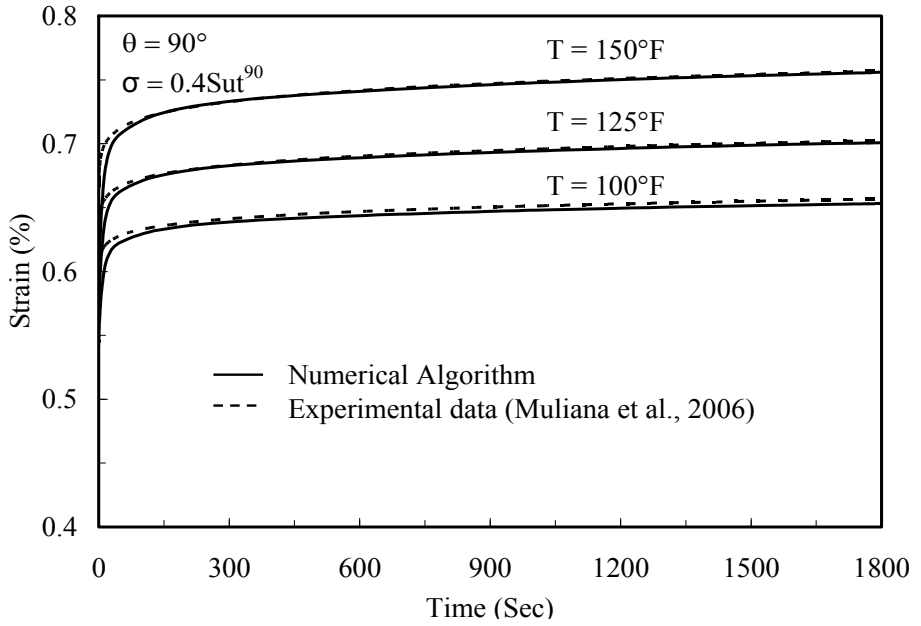

Fig. 2.14 Creep strain response for glass/vinylester ($\theta = 90°$) at several temperatures and $\sigma = 0.4Sut^{90}$

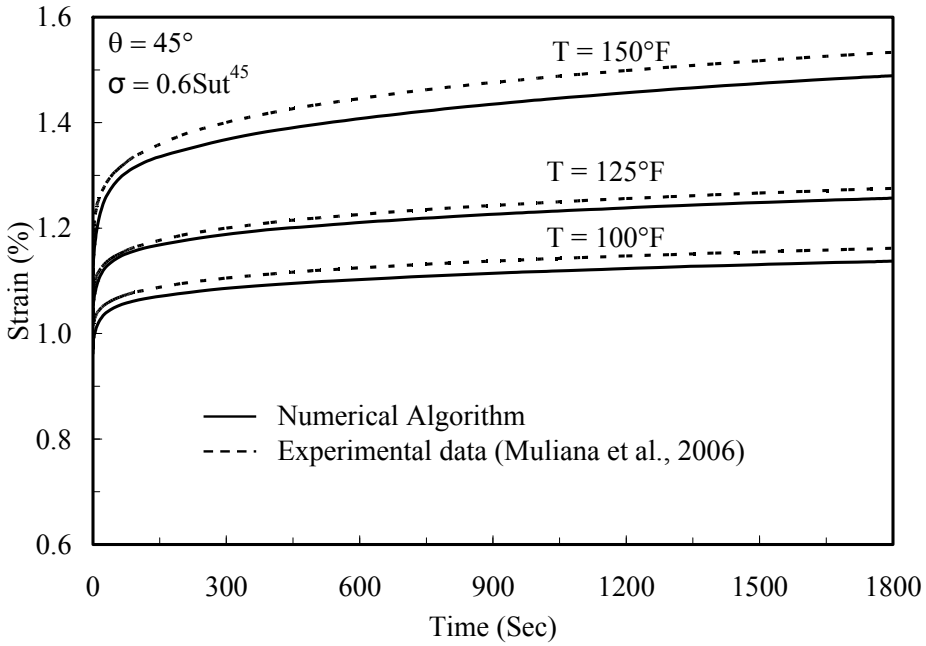

Fig. 2.15 Creep strain response for glass/vinylester ($\theta = 45°$) at several temperatures and $\sigma = 0.6Sut^{45}$

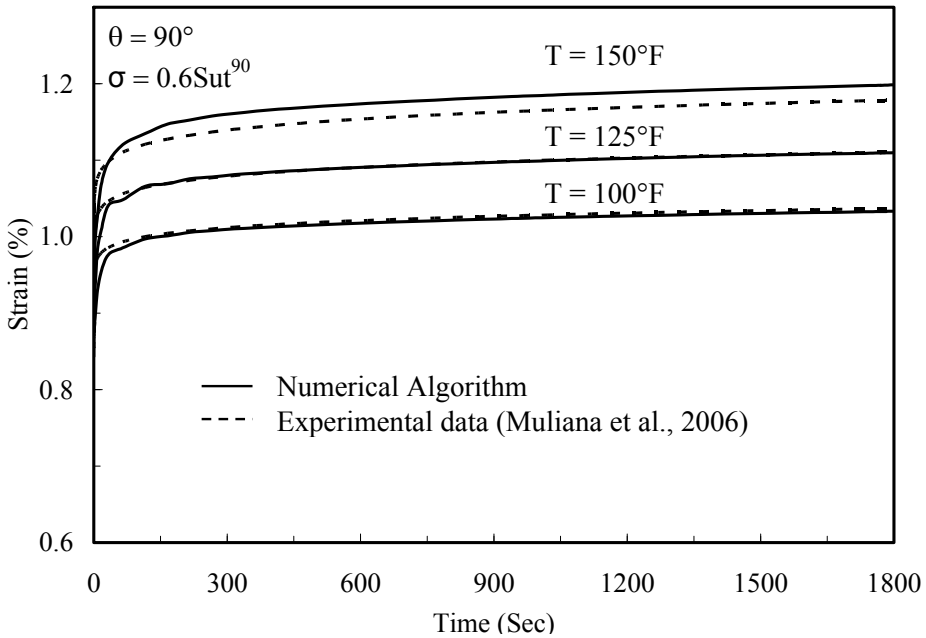

Fig. 2.16 Creep strain response for glass/vinylester ($\theta = 90°$) at several temperatures and $\sigma = 0.6Sut^{45}$

For the 90° specimens, at $0.6\,S_{ut}^{\theta}$, a slightly wavy pattern of strain instead of a monotone is observed at initial times due to the high nonlinearities and tight convergence tolerances in the analysis. Analysis for the 0° specimen at combination of higher stress levels and higher temperature levels results in specimen failures [57] due to a very high nonlinearity and hence is not presented here.

2.3.4 Isotropic material responses

The numerical algorithm is also validated for an isotropic nonlinear viscoelastic response of TCM. Peretz & Weitsman [63] reported the nonlinear viscoelastic behavior of FM-73 polymer adhesive. Thermo-mechanical tests were performed under several loading histories. The reported elastic properties for FM-73 resin are given in Table 2.8. The fitted Prony parameters are given in Table 2.9.

Table 2.8 Elastic properties for FM-73 resin

Modulus (MPa) E	Poisson's ratio ν
2710	0.35

Table 2.9 Prony parameters for FM-73

N	λn (1/s)	Dn x 10^{-6} (1/MPa)
1	1	21
2	10^{-1}	21.6
3	10^{-2}	11.8
4	10^{-3}	15.9
5	10^{-4}	21.6
6	10^{-5}	20.1

The stress dependant nonlinear parameters related to the effective stress and the temperature dependent parameters are given by the following functions:

$$g_0(\sigma) = 1 + 0.15\left(\frac{\bar{\sigma}}{\sigma_0}\right) \qquad g_0(T) = 1 + 0.91\frac{T - 303}{303}$$

$$g_1(\sigma) = 1 + 1.435\left(\frac{\bar{\sigma}}{\sigma_0}\right)^{2.4} \qquad g_1(T) = \exp\left(-8.5\frac{T - 303}{303}\right) \tag{2.38}$$

$$g_2(\sigma) = 1 + 0.75\left(\frac{\bar{\sigma}}{\sigma_0}\right)^{2} \qquad g_2(T) = \exp\left(12.12\frac{T - 303}{303}\right)$$

$$a(\sigma) = \exp\left(\frac{-1.75\bar{\sigma}}{\sigma_o}\right) \qquad a(T) = \exp\left(-5.0\frac{T - 303}{303}\right)$$

where σ_0=50 Mpa and T is in Kelvin

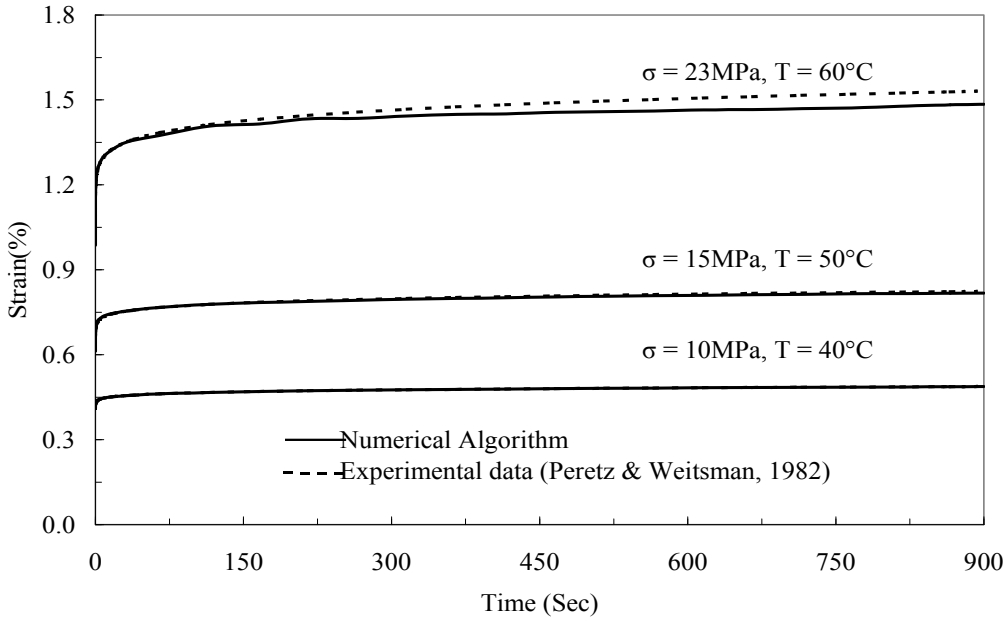

Fig. 2.17 Creep strain response for FM-73 resin at various constant temperatures and constant stresses

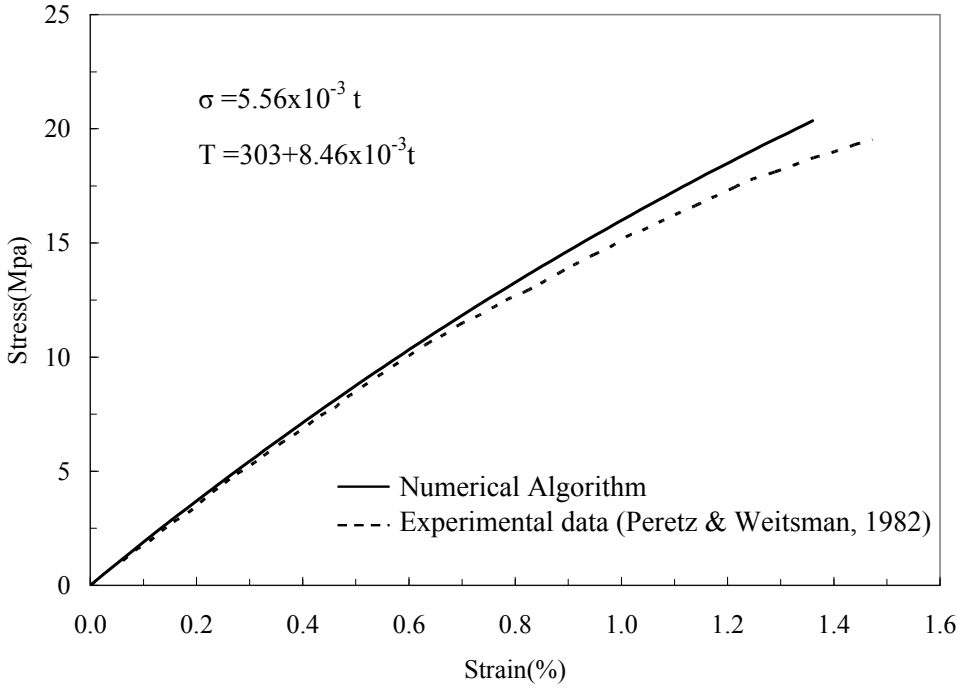

Fig. 2.18 Stress-strain response for FM-73 resin under linearly varying temperature and stress

The algorithm is verified for creep strains at different stress and temperature levels. Fig. 2.17 shows the thermo-mechanical creep responses from the numerical algorithm and experimental data. Finally the algorithm is verified for a combination of linearly varying temperature and stress. The stress-strain data, illustrated in Fig. 2.18, show excellent agreements between the numerical and experimental results. This verifies the capability and accuracy on the proposed recursive-iterative algorithm in modeling time-dependent responses for general thermo-mechanical loading.

2.4 INTEGRATION WITH FE STRUCTURAL ANALYSIS

The integrated thermo-mechanical viscoelastic algorithm in the FE analysis of practical structural components under multi-axial stresses is presented. For this purpose, a square plate with a central hole is analyzed. A state of multi-axial stress exists around the hole even for a uniaxial load applied at the two opposite ends. A thin square plate with a hole with D/w ratio of 0.05 is considered for the analysis. The schematic diagram of plate with hole is shown in Fig. 2.19.

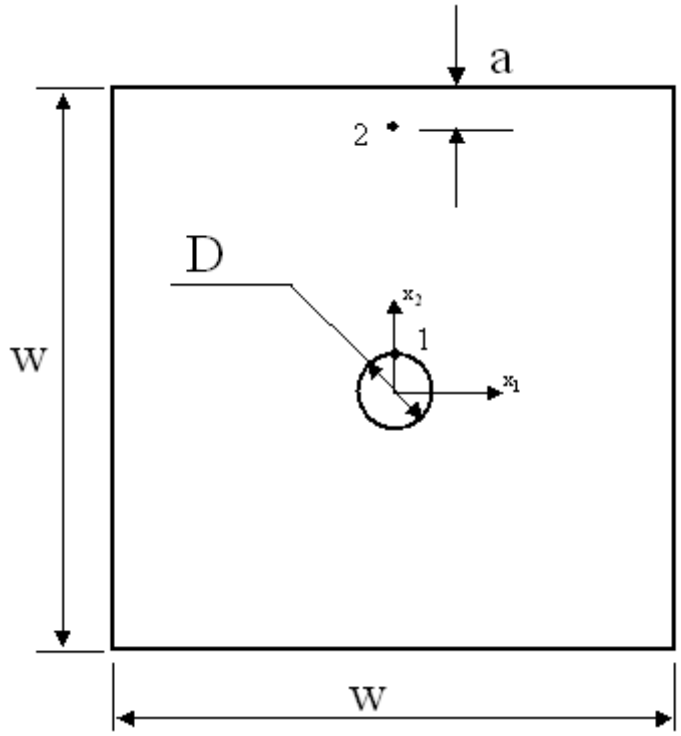

Fig. 2.19 Square plate with a hole with $D/w = 0.05$ and $a/w \approx 0.04$

The analysis is performed for an orthotropic glass/vinylester plate with a hole. The following two case studies are considered for the orthotropic plate with fiber angle θ=45°:

1. Isothermal temperatures T_0 = 100°F, 125°F & 150°F and a nominal creep stress σ_{11} along x_1 direction in the plate (away from the hole) is applied. The following boundary conditions are imposed:

$$\begin{aligned} &\sigma_{11}(x_1,x_2,t) = 0.2S_{ut}^{45} \quad \forall\, x_1 = -\frac{w}{2} \text{ and } x_1 = \frac{w}{2} \quad at \quad t \geq 0 \\ &\qquad\qquad -\frac{w}{2} \leq x_2 \leq \frac{w}{2} \\ &T(x_1,x_2,t) = T_0 \quad \forall\, -\frac{w}{2} \leq x_1 \leq \frac{w}{2} \quad at \quad t \geq 0 \\ &\qquad\qquad -\frac{w}{2} \leq x_2 \leq \frac{w}{2} \end{aligned} \tag{2.39}$$

2. Non-isothermal loading with temperature of 125°F is applied on the left side of the plate at time $t \geq 0$, where the rest of the plate is at a temperature of 75°F, and a nominal creep stress of $0.2\,S_{ut}^{45}$. The following initial and boundary conditions are imposed:

$$\begin{aligned} &\sigma_{11}(x_1,x_2,t) = 0.2S_{ut}^{45} \quad \forall\, x_1 = -\frac{w}{2} \text{ and } x_1 = \frac{w}{2} \quad at \quad t \geq 0 \\ &\qquad\qquad -\frac{w}{2} \leq x_2 \leq \frac{w}{2} \\ &T(x_1,x_2,0) = 75^o F \quad \forall\, -\frac{w}{2} < x_1 \leq \frac{w}{2} \\ &\qquad\qquad -\frac{w}{2} \leq x_2 \leq \frac{w}{2} \\ &T(x_1,x_2,t) = 125^o F \quad \forall\, x_1 = -\frac{w}{2} \\ &\qquad\qquad -\frac{w}{2} \leq x_2 \leq \frac{w}{2} \end{aligned} \tag{2.40}$$

Figs. 2.20 and 2.21 show the strain-time responses for plate with fiber angle 45° subjected to a nominal creep stress of $0.2\,S_{ut}^{45}$ and three isothermal temperature loadings of 100°F, 125°F and 150°F at location away from and near the hole, respectively. For all the cases, though the nominal stresses in the plate are in the linear viscoelastic range, the stresses near the hole are in the nonlinear viscoelastic range. A stress relaxation behavior

in the vicinity of the hole occurs for the orthotropic plate. The analytical results for strain are calculated using the stresses obtained through the FE analysis. Thus this analysis represents a successful integration of the algorithm with structural analysis.

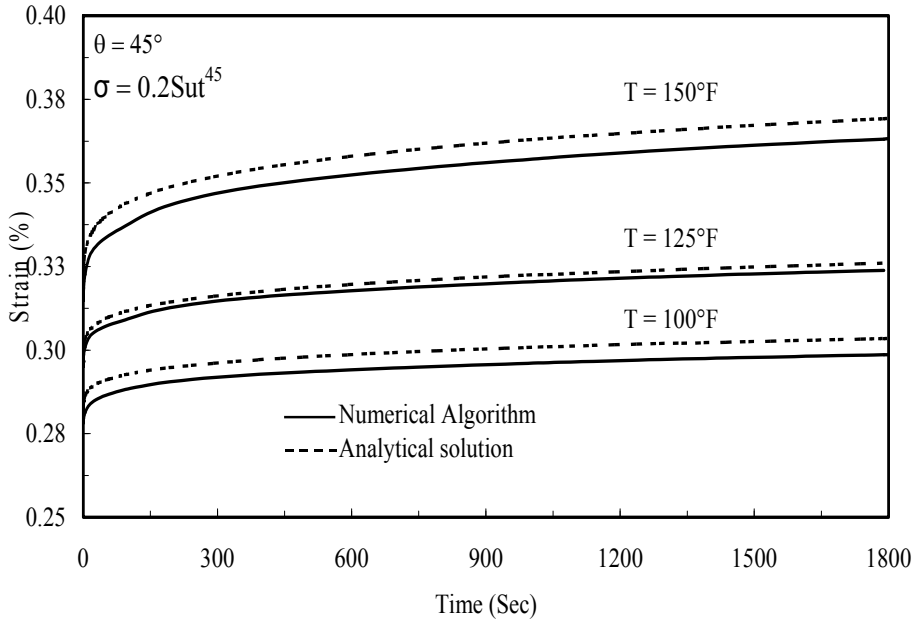

Fig. 2.20 Strain (ε_{11}) time response for GVFRP plate subjected to isothermal loading for various temperatures at location away from the hole. (x_1=0, $x_2 \approx$0.46w)

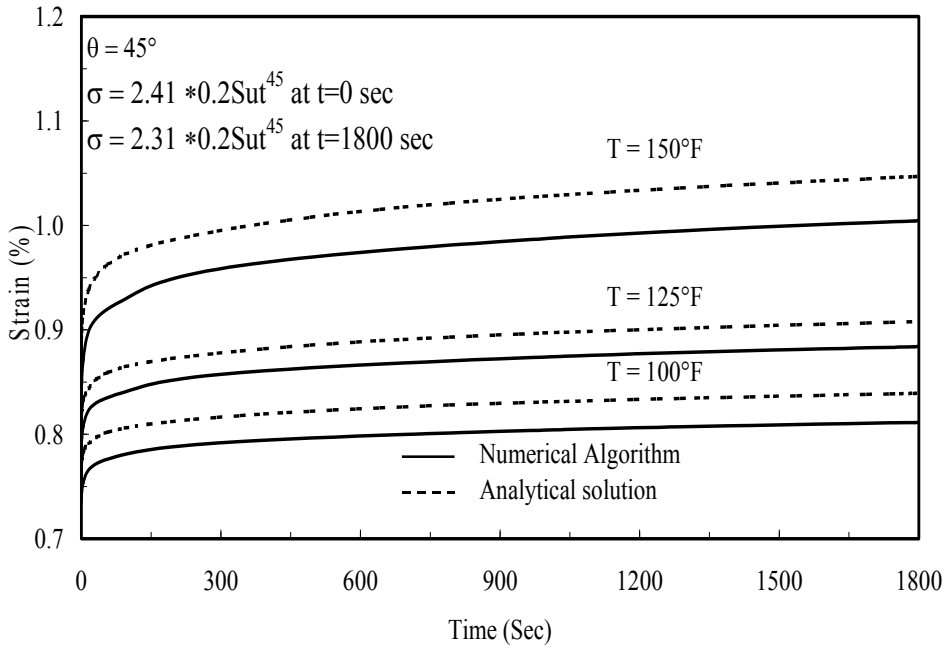

Fig. 2.21 Strain (ε_{11}) time response for GVFRP plate subjected to isothermal loading for various temperatures at location near the hole (x_1=0, x_2=D/2)

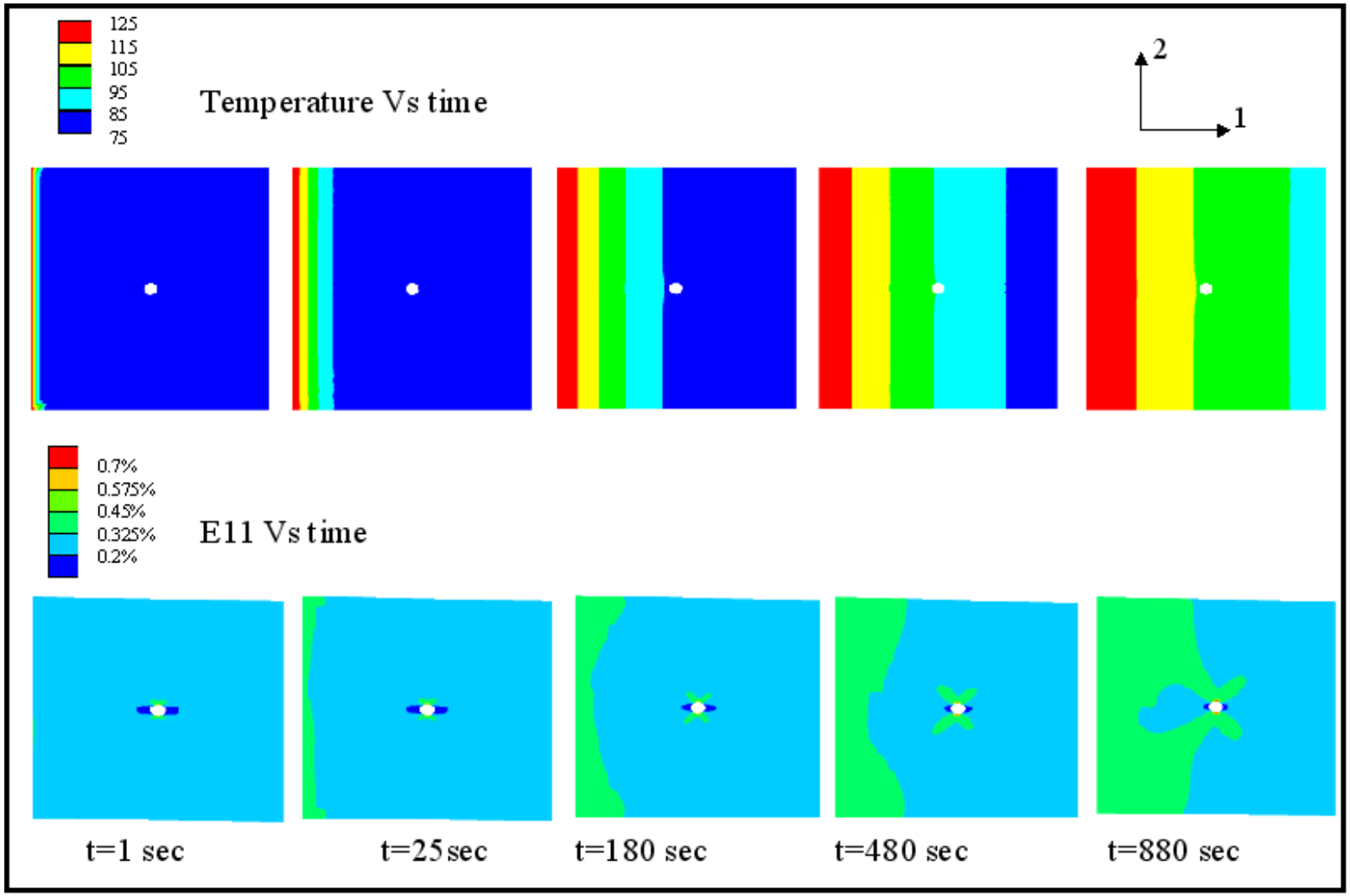

Fig. 2.22 Temperature and strain plots for various times when a temperature loading of 125F is applied to one end of a plate at 75F (GVFRP plate with $\theta = 45°$)

For the second case, an uncoupled sequential thermo-mechanical analysis is carried out. First a transient heat transfer analysis is performed to obtain the temperature distribution at various times in the plate. This is then used as an input to the mechanical viscoelastic analysis. The temperature and strain plots at various times are shown in Fig. 2.22. This illustrates a non-isothermal uncoupled thermo-mechanical analysis of orthotropic structures where the algorithm can be suitably used.

CHAPTER III

A MICROMECHANICAL HOMOGENIZATION METHOD FOR UNIDIRECTIONAL FRP WITH TWO VISCOELASTIC CONSTITUENTS[†]

The time dependent response of fiber and polymer matrix constituents can be related to the overall time dependent responses of the FRP using of suitable micromechanical models. Extensive studies on homogenization of time dependent behaviors of FRP have considered linear elastic fibers and viscoelastic polymeric matrix. The development of synthetic (polymer) reinforcements such as Kevlar and polyethylene, which exhibit a time dependent behavior, provides a motivation for development of a micromechanical model that accounts for the viscoelastic behavior of the fiber as well. The micromechanical model must also take into account the anisotropic behavior of the fiber.

This chapter presents a formulation of a concurrent micromechanical model for predicting effective nonlinear viscoelastic responses of FRP composites with both fiber and matrix constituents exhibiting different thermo-viscoelastic behaviors. An orthotropic unidirectional fibrous reinforcement and a isotropic matrix is considered in the FRP. The viscoelastic material properties for the fiber and matrix are allowed to change with stress and temperature fields and they are assumed to follow the thermo-rheologically (TCM) behaviors. The time integration algorithm developed in chapter II

[†]With kind permission from Springer Science + Business Media: Acta Mechanica, Responses of viscoelastic polymer composites with temperature and time dependent constituents (Accepted for publication), Muliana A.H., Sawant S. P. © Springer-Verlag 2008

is used within this micromodel to obtain the nonlinear viscoelastic responses for the fiber and the matrix. The numerical implementation and verification of the micromodel are also discussed. Available experimental data from the literature are used for comparisons. Furthermore, detailed FE models of the FRP microstructures are generated and the global responses obtained from the micromodel formulation are compared to the ones obtained from the detailed FE models.

3.1 MICROMECHANICAL FORMULATION

Extensive studies on the micromechanical formulations deal with combining linear elastic fiber and nonlinear viscoelastic matrix to obtain effective viscoelastic responses of FRP composites. In such case, the overall nonlinear and time-dependent characteristics of the composites are controlled by the time-dependent function of the polymers. In this study, the previously developed unit-cell model of unidirectional FRP composites (Haj-Ali and Muliana [30]) is modified to incorporate different nonlinear time-dependent functions for the fiber and matrix constituents. The constituent viscoelastic and thermal properties are also allowed to change with the stress and temperature fields. Thus, the overall composite responses are time, stress and temperature dependent. It is also possible to incorporate strain, strain rate, and moisture dependent parameters in the micromechanical formulation. To accurately analyze the nonlinear time-dependent responses of the composites, one requires two-way micromechanical relations that provide effective composite behaviors by homogenizing properties of the fiber and matrix constituents, and simultaneously transfer the external

mechanical and thermal stimuli from the global structures to the fiber and matrix constituents.

A simplified micromechanical relation is derived from the idealized FRP microstructures, which are modeled as periodic distributed arrays of square fibers embedded in a polymeric matrix (Fig. 3.1). A composite representative volume element (RVE) is defined by a square fiber placed in the center of a square matrix domain. A one fourth unit-cell micromechanical model consisting of four subcells is generated due to the two-plane symmetry of the RVE.

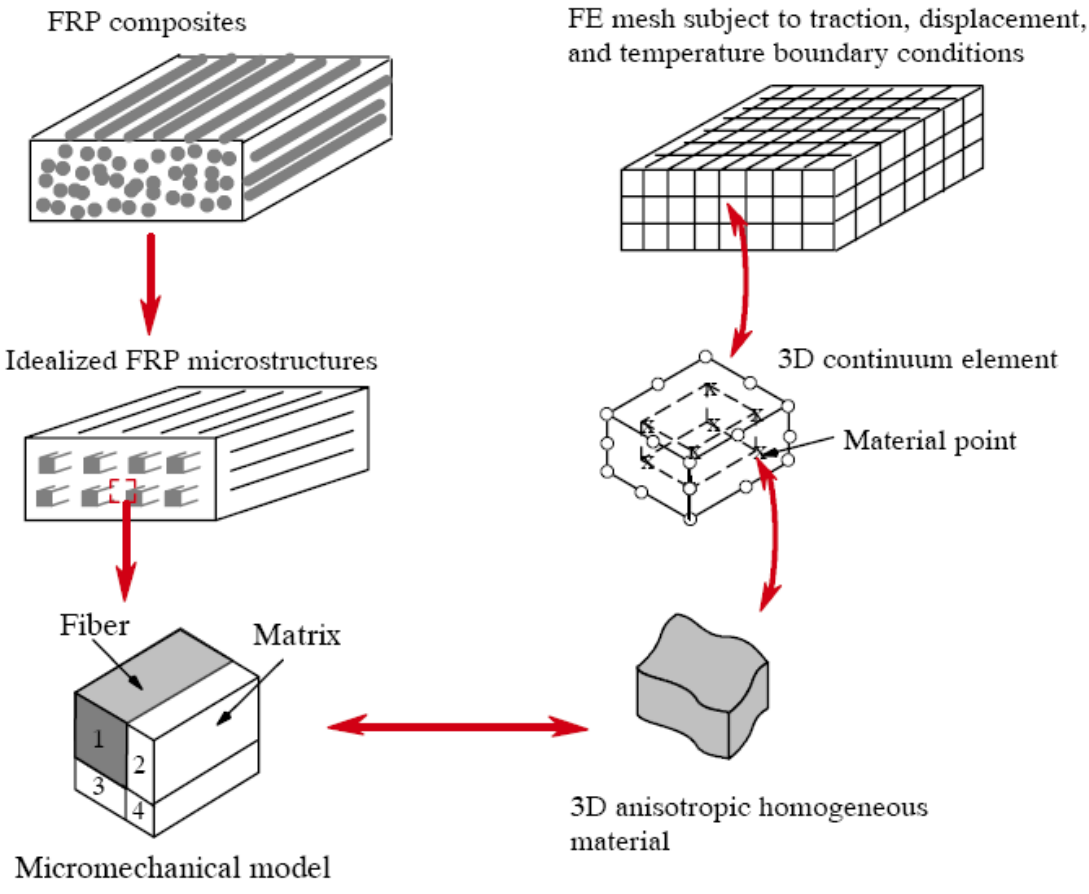

Fig. 3.1 Idealized micromechanical model for fiber reinforced polymers

The viscoelastic constitutive relations with stress and temperature dependent material parameters are examined at the fiber and matrix subcells. The micromechanical relations are formulated by assuming perfect bond between the interphase fiber and matrix. The result from the micromechanical relations is a 3D effective anisotropic viscoelastic response of a homogenous composite medium. This micromodel is integrated to FE framework for analyzing thermo-viscoelastic responses of composite structures. The 3D effective anisotropic response is implemented at every material point in a FE mesh. It is also necessary to determine stress, strain, and temperature fields in the fiber and matrix subcells from the external thermal and mechanical stimuli applied at the composite or global structural level. This is achieved by formulating concentration matrices that relate the composite effective field quantities to the constituent field quantities.

The nonlinear and time-dependent responses are solved in an iterative manner with linearized incremental stress-strain relation and iterative correction schemes within an incremental time step. Stress or strain correction schemes have to be performed simultaneously in the unit-cell (micromechanical) model and in the fiber and matrix constituents. This is done in order to minimize residual due to linearization. At every incremental time step, the concentration matrices are formulated and the consistent tangent stiffness of the fiber, matrix, and composites are updated once convergence is achieved.

3.1.1 Linearized micromechanical relations

At current time *t*, the total effective stresses and strains are given as:

$$\begin{aligned} \bar{\sigma}_{ij}^{t} &= \bar{\sigma}_{ij}^{t-\Delta t} + \Delta\bar{\sigma}_{ij}^{t} \\ \bar{\varepsilon}_{ij}^{t} &= \bar{\varepsilon}_{ij}^{t-\Delta t} + \Delta\bar{\varepsilon}_{ij}^{t} \end{aligned} \tag{3.1}$$

The superscript t-Δt denotes the field quantities from the previous converged step, which are stored as history variables. A basic unit-cell that represents geometrical and material characteristics is defined. The unit-cell is divided into a number of subcells and the spatial variation of the displacement field in each subcell is assumed such that the stresses and deformations are spatially uniform. Traction continuity and displacement compatibility at an interface between subcells are satisfied in an average sense. Thus, the incremental average stresses and strains in the unit-cell model at time t are defined by:

$$\Delta\bar{\sigma}_{ij}^{t} = \frac{1}{V}\sum_{\alpha=1}^{N}\int_{V^{(\alpha)}} \Delta\sigma_{ij}^{t,(\alpha)}(x_k^{(\alpha)})dV^{(\alpha)} \approx \frac{1}{V}\sum_{\alpha=1}^{N} V^{(\alpha)}\Delta\sigma_{ij}^{t,(\alpha)} \tag{3.2}$$

$$\Delta\bar{\varepsilon}_{ij}^{t} = \frac{1}{V}\sum_{\alpha=1}^{N}\int_{V^{(\alpha)}} \Delta\varepsilon_{ij}^{t,(\alpha)}(x_k^{(\alpha)})dV^{(\alpha)} \approx \frac{1}{V}\sum_{\alpha=1}^{N} V^{(\alpha)}\Delta\varepsilon_{ij}^{t,(\alpha)} \tag{3.3}$$

The superscript α denotes the subcell number and N is the number of subcells. The stress $\Delta\sigma_{ij}^{(\alpha)}$ and strain $\Delta\varepsilon_{ij}^{(\alpha)}$ are the incremental average stress and strain within each subcell. The unit-cell volume V is:

$$V = \sum_{\alpha=1}^{N} V^{(\alpha)} \tag{3.4}$$

Detailed micromechanical stress and strain relations within the subcells for the unidirectional FRP are summarized in Appendix A. Next, concentration matrices that

relate the global average (macro) quantities to the local (micro) quantities are formulated. A stress-concentration matrix is formulated when the stresses are prescribed at the macro level. When the macrostrains are given, a strain-concentration matrix is defined. In this study, the micromechanical model is designed to be compatible with displacement based FE structural analyses, in which the effective incremental strain $\Delta\bar{\boldsymbol{\varepsilon}}^{t}$ is chosen as the independent tensor. Thus, the subcell strain-interaction matrix ($\boldsymbol{B}^{t,(\alpha)}$), which relates the subcell average strains, $\Delta\boldsymbol{\varepsilon}^{t,(\alpha)}$, to the unit-cell average strain, $\Delta\bar{\boldsymbol{\varepsilon}}^{t}$, is:

$$\Delta\varepsilon_{ij}^{t,(\alpha)} = B_{ijkl}^{t,(\alpha)}\Delta\bar{\varepsilon}_{kl}^{t} \tag{3.5}$$

Substituting Eq. (3.5) to (3.3) gives:

$$\Delta\bar{\varepsilon}_{ij}^{t} = \frac{1}{V}\sum_{\alpha=1}^{N} V^{(\alpha)} B_{ijkl}^{t,(\alpha)}\Delta\bar{\varepsilon}_{kl}^{t} \tag{3.6}$$

Equation (3.6) must hold for an arbitrary average strain $\Delta\bar{\boldsymbol{\varepsilon}}^{t}$, which requires the following relations be satisfied:

$$\frac{1}{V}\sum_{\alpha=1}^{N} V^{(\alpha)} B_{ijkl}^{t,(\alpha)} = \delta_{ik}\delta_{jl} \tag{3.7}$$

which also implies that:

$$\frac{1}{V}\sum_{\alpha=1}^{N} V^{(\alpha)} (B_{ijkl}^{t,(\alpha)} - \delta_{ik}\delta_{jl}) = 0 \tag{3.8}$$

Using the strains defined in Eq. (3.5), the constitutive equation for linearized stress-strain relations in each subcell is expressed as:

$$\Delta\sigma_{ij}^{t,(\alpha)} = C_{ijkl}^{t,(\alpha)}\Delta\varepsilon_{kl}^{t,(\alpha)} = C_{ijkl}^{t,(\alpha)} B_{klrs}^{t,(\alpha)}\Delta\bar{\varepsilon}_{rs}^{t} \tag{3.9}$$

where $\boldsymbol{C}^{t,(\alpha)}$ is the consistent tangent stiffness matrix of the subcell (α), which is defined in Eq. (2.31). Substituting Eqs. (3.9) into (3.2) gives:

$$\Delta\bar{\sigma}_{ij}^{t} = \frac{1}{V}\sum_{\alpha=1}^{N} V^{(\alpha)} C_{ijkl}^{t,(\alpha)} B_{klrs}^{t,(\alpha)} \Delta\bar{\varepsilon}_{rs}^{t} \tag{3.10}$$

The unit-cell effective tangent stiffness matrix $\bar{\boldsymbol{C}}^{t}$ is determined by:

$$\bar{C}_{ijrs}^{t} = \frac{1}{V}\sum_{\alpha=1}^{N} V^{(\alpha)} C_{ijkl}^{t,(\alpha)} B_{klrs}^{t,(\alpha)} \tag{3.11}$$

It is also possible to define a stress interaction matrix $\boldsymbol{F}^{(\alpha)}$, which relates the subcell average stress, $\boldsymbol{\Delta\sigma}^{t,(\alpha)}$, to the unit-cell average stress, $\boldsymbol{\Delta\bar{\sigma}}^{t}$:

$$\Delta\sigma_{ij}^{t,(\alpha)} = F_{ijkl}^{t,(\alpha)} \Delta\bar{\sigma}_{kl}^{t} \tag{3.12}$$

Using the constitutive equation for each subcell, the incremental strains at each subcell can be determined by:

$$\Delta\varepsilon_{ij}^{t,(\alpha)} = [C_{ijkl}^{t,(\alpha)}]^{-1} F_{klmn}^{t,(\alpha)} \Delta\bar{\sigma}_{mn}^{t} \tag{3.13}$$

Substituting Eqs. (3.13) into (3.3) gives:

$$\Delta\bar{\varepsilon}_{ij}^{t} = \sum_{\alpha=1}^{N} V^{(\alpha)} [C_{ijkl}^{t,(\alpha)}]^{-1} F_{klmn}^{t,(\alpha)} \Delta\bar{\sigma}_{mn}^{t} \tag{3.14}$$

Finally, the unit-cell effective tangent stiffness matrix $\bar{\boldsymbol{C}}^{t}$ is determined by:

$$[\bar{C}_{ijmn}^{t}]^{-1} = \sum_{\alpha=1}^{N} V^{(\alpha)} [C_{ijkl}^{t,(\alpha)}]^{-1} F_{klmn}^{t,(\alpha)} \tag{3.15}$$

The RVE's length scale is assumed to be much smaller than the macrostructural scale such that the steady state condition in each unit-cell (represented by a material point) is reached in a very short period in comparison to the overall time responses.

Therefore, the transient heat conduction analysis in each unit-cell of the RVE is bypassed and temperatures are assumed to vary only within the global material points. The total temperature in each unit-cell at the steady-state condition is defined by:

$$\begin{aligned} \Delta T^{t,(\alpha)} &= \Delta \overline{T}^{t} \\ T^{t+\Delta t,\alpha} &= T^{t,(\alpha)} + \Delta T^{t,(\alpha)} \end{aligned} \tag{3.16}$$

In the case of temperature boundary conditions are considered, the micromechanical relations in Appendix A are defined in terms of total mechanical and thermal quantities. This allows calculating thermal stresses due to mismatch in the coefficient of thermal expansions of the fiber and matrix constituents.

3.1.2 Formulations of the B and F matrices

Up to this point, the strain-interaction matrices $\boldsymbol{B}^{t,(\alpha)}$ or the stress-interaction matrices $\boldsymbol{F}^{t,(\alpha)}$ have not been determined. In order to derive the strain-interaction matrices or the stress-interaction matrices for all subcells, the micromechanical relations in Appendix A together with the subcells' constitutive material models are used. In the case of $\boldsymbol{B}^{t,(\alpha)}$ matrices are formulated, six components of strains need to be determined in every subcell. Thus, total of 24 strain components are defined, which requires forming 24 equations. The first set of equations is formulated from the strain compatibility equations, which are:

$$\underset{(13\times1)}{\left\{\boldsymbol{R}_{\varepsilon}^{t}\right\}}=\underset{(13\times24)}{\left[\boldsymbol{A_1}\right]}\underset{(24\times1)}{\left\{\begin{matrix}\Delta\varepsilon^{t,(1)}\\ \Delta\varepsilon^{t,(2)}\\ \Delta\varepsilon^{t,(3)}\\ \Delta\varepsilon^{t,(4)}\end{matrix}\right\}}-\underset{(13\times6)}{\left[\boldsymbol{D_1}\right]}\underset{(6\times1)}{\left\{\Delta\bar{\varepsilon}^{t}\right\}} \tag{3.17}$$

where $\boldsymbol{R}_{\varepsilon}^{t}$ is the residual vector arising from imposing linearized strain compatibility relations with nonlinear constitutive relations in all subcells. In the case of linear elastic responses are exhibited for all subcells, the vector $\boldsymbol{R}_{\varepsilon}^{t}$ is automatically reduced to zero. The components of matrices $\boldsymbol{A_1}$ and $\boldsymbol{D_1}$ in Eq. (3.17) are given in Appendix B. The second set of equations is formed by satisfying the traction continuity relations. Up to this stage, the components of effective stress tensor σ_{ij}^{t} remain unknown. Equations based on the traction continuity relations within subcells should avoid the presence of σ_{ij}^{t}, which are written as:

$$\underset{(11\times1)}{\left\{\boldsymbol{R}_{\sigma}^{t}\right\}}=\underset{(11\times24)}{\left[\boldsymbol{A}_{\boldsymbol{2}}^{\boldsymbol{t}}\right]}\underset{(24\times1)}{\left\{\begin{matrix}\Delta\varepsilon^{t,(1)}\\ \Delta\varepsilon^{t,(2)}\\ \Delta\varepsilon^{t,(3)}\\ \Delta\varepsilon^{t,(4)}\end{matrix}\right\}}-\underset{(11\times6)}{\left[\boldsymbol{O}\right]}\underset{(6\times1)}{\left\{\Delta\bar{\varepsilon}^{t}\right\}} \tag{3.18}$$

The residual vector $\boldsymbol{R}_{\sigma}^{t}$ is due to the traction continuity relations, which for linear elastic constituents its components are zero. The matrix **O** is the zero matrix and the components matrix $\boldsymbol{A}_{\boldsymbol{2}}^{\boldsymbol{t}}$ are given in Appendix B. The $\boldsymbol{B}^{t,(\alpha)}$ matrices in Eq. (3.5) are then formed using Eqs. (3.17) and (3.18), which in linearized relations are:

$$\underset{(24\times 6)}{\begin{Bmatrix} \boldsymbol{B}^{t,(1)} \\ \boldsymbol{B}^{t,(2)} \\ \boldsymbol{B}^{t,(3)} \\ \boldsymbol{B}^{t,(4)} \end{Bmatrix}} = \underset{(24\times 24)}{\begin{bmatrix} \boldsymbol{A_1} \\ \boldsymbol{A_2^t} \end{bmatrix}^{-1}} \underset{(24\times 6)}{\begin{bmatrix} \boldsymbol{D_1} \\ \boldsymbol{O} \end{bmatrix}} \tag{3.19}$$

Once the $\boldsymbol{B}^{t,(\alpha)}$ matrices are determined, the strain components in each subcell are also known and the nonlinear constitutive relations in each subcell can be calculated. Finally, the effective homogenized stresses and tangent stiffness matrix can be solved using Eqs. (3.10) and (3.11), respectively.

When incremental effective stresses are the given variables, the stress-interaction matrices $\boldsymbol{F}^{t,(\alpha)}$ are formulated. Six scalar components of stress tensor are determined for each subcell. The traction continuity and displacement compatibility lead to the following relations:

$$\underset{(11\times 1)}{\begin{Bmatrix} \boldsymbol{R_\sigma^t} \end{Bmatrix}} = \underset{(11\times 24)}{\begin{bmatrix} \boldsymbol{A_3} \end{bmatrix}} \underset{(24\times 1)}{\begin{Bmatrix} \Delta\sigma^{t,(1)} \\ \Delta\sigma^{t,(2)} \\ \Delta\sigma^{t,(3)} \\ \Delta\sigma^{t,(4)} \end{Bmatrix}} - \underset{(11\times 6)}{\begin{bmatrix} \boldsymbol{D_2} \end{bmatrix}} \underset{(6\times 1)}{\begin{Bmatrix} \Delta\bar{\sigma}^{t} \end{Bmatrix}} \tag{3.20}$$

$$\underset{(11\times 1)}{\begin{Bmatrix} \boldsymbol{R_\varepsilon^t} \end{Bmatrix}} = \underset{(13\times 24)}{\begin{bmatrix} \boldsymbol{A_4^t} \end{bmatrix}} \underset{(24\times 1)}{\begin{Bmatrix} \Delta\sigma^{t,(1)} \\ \Delta\sigma^{t,(2)} \\ \Delta\sigma^{t,(3)} \\ \Delta\sigma^{t,(4)} \end{Bmatrix}} - \underset{(13\times 6)}{\begin{bmatrix} \boldsymbol{O} \end{bmatrix}} \underset{(6\times 1)}{\begin{Bmatrix} \Delta\bar{\sigma}^{t} \end{Bmatrix}} \tag{3.21}$$

The $\boldsymbol{F}^{t,(\alpha)}$ matrices are then formed using:

$$\underset{(24\times 6)}{\begin{Bmatrix} \boldsymbol{F}^{t,(1)} \\ \boldsymbol{F}^{t,(2)} \\ \boldsymbol{F}^{t,(3)} \\ \boldsymbol{F}^{t,(4)} \end{Bmatrix}} = \underset{(24\times 24)}{\begin{bmatrix} \boldsymbol{A}_3 \\ \boldsymbol{A}_4^t \end{bmatrix}^{-1}} \underset{(24\times 6)}{\begin{bmatrix} \boldsymbol{D}_1 \\ \boldsymbol{O} \end{bmatrix}} \tag{3.22}$$

Once the $\boldsymbol{F}^{t,(a)}$ matrices are determined, the stress components and nonlinear constitutive relations can be calculated, and the effective homogenized strain and tangent stiffness matrix can be solved using Eqs. (3.14) and (3.15), respectively.

3.1.3 Iterative correction schemes

The linearized micromechanical relations will give exact solutions when the constitutive material models for all subcells are linear elastic. In this study, the fiber and matrix subcells experience different nonlinear and time-dependent behaviors, in which upon imposing the micromechanical relations in Appendix A leads to nonzero residual strain and stress as defined in Eqs. (3.17) and (3.18) or in Eqs. (3.20) and (3.21). An iterative corrector scheme is formulated at every incremental time step to satisfy both the micromechanical constraints and the nonlinear viscoelastic constitutive equations. The residual vector is defined using Eqs. (3.17) and (3.18) in the case of components of the effective strain are chosen as independent variables, which is presented in this study. To minimize the 24 components of the residual vector, the subcells' stress-strain components need to be corrected, which involves a total of 48 stress and strain scalar variables in the four subcells. These scalar variables are related via constitutive relations

leading to only 24 independent variables. In this study, the components of strains in each subcell $\varepsilon_{ij}^{(\alpha)}$ are chosen as independent variables, which are:

$$X^{t,T} = \left\{ \varepsilon^{t,(1)} \quad \varepsilon^{t,(2)} \quad \varepsilon^{t,(3)} \quad \varepsilon^{t,(4)} \right\}_{(1\times 24)} \tag{3.23}$$

The stress components in the subcells are defined as functions of independent variables X_{ij}^{t}. The Newton Raphson (NR) iterative method is used to minimize residual vector and find solutions of the independent variables X_{ij}^{t}:

$$\begin{aligned} X^{t,k+1} &= X^{t,k} + \left[\frac{\partial \boldsymbol{R}^{t,k}}{\partial X} \right]^{-1} \boldsymbol{R}^{t,k} \\ \left[\frac{\partial \boldsymbol{R}^{t,k}}{\partial X} \right] &= \begin{bmatrix} A_1^k \\ A_2^{t,k} \end{bmatrix} \qquad k = \textit{iteration counter} \end{aligned} \tag{3.24}$$

A converged solution is achieved when the residual vectors $\boldsymbol{R}_{\varepsilon}^{t}$ and $\boldsymbol{R}_{\sigma}^{t}$ defined in the micromechanical model and in the viscoelastic constitutive equations are diminished. Once convergence is achieve the current incremental stresses and consistent tangent stiffness matrix in Eqs. (3.10) and (3.11), respectively, are updated. To perform structural analyses using the FE framework, these variables are sampled at each material point and sent to the upper FE structural level.

3.2 NUMERICAL IMPLEMENTATION AND VERIFICATION

The thermo-viscoelastic responses obtained from the micromechanical model are first verified using limited experimental data on unidirectional fiber reinforced polymer

composites of carbon-polyimide and Kevlar-epoxy systems. Elastic material properties of carbon-polyimide composites with 56% volume fractions at various temperatures are obtained from Kumosa and collaborators (Odegard and Kumosa [60], Benedikt et al. [5], Rupnowski et al. [71]). Creep compliances of Kevlar-epoxy systems having 63% volume fractions studied by Walruth [83] are also used to verify the micromodel prediction of the overall time-dependent responses. Furthermore, detailed FE meshes of composite's representative volume elements (RVE) at several fiber volume fractions (20%, 40%, and 50%) are generated. Thermo-viscoelastic responses from the simplified micromodel formulation are compared to the ones obtained using the detailed FRP meshes.

3.2.1 Temperature dependent elastic properties of graphite T360/ PMR-15 polyimide systems

The micromechanical model is used to determine effective elastic stiffness of carbon-polyimide composites with 56% volume fractions. The in-situ elastic properties for the transversely isotropic carbon fiber and isotropic polyimide matrix measured at room temperature are given in Table 3.1.

Table 3.1 Elastic properties for T650 graphite and PMR-15 matrix

Material	Modulus Gpa (ksi)				Poisson's ratio	
	E_{11}	$E_{22}=E_{33}$	$G_{12}=G_{13}$	G_{23}	$\nu_{12}=\nu_{13}$	ν_{23}
Fiber (T650-35 Graphite)	5.8(841)	224(32480)	15.4(2233)	21.1(3060)	0.40	0.40
Matrix (PMR15 polyimide)	3.97 (576)				0.36	

The temperature dependent elastic modulus for the polyimide system, reported by Rupnowski et al. [71], is illustrated in Fig. 3.2.

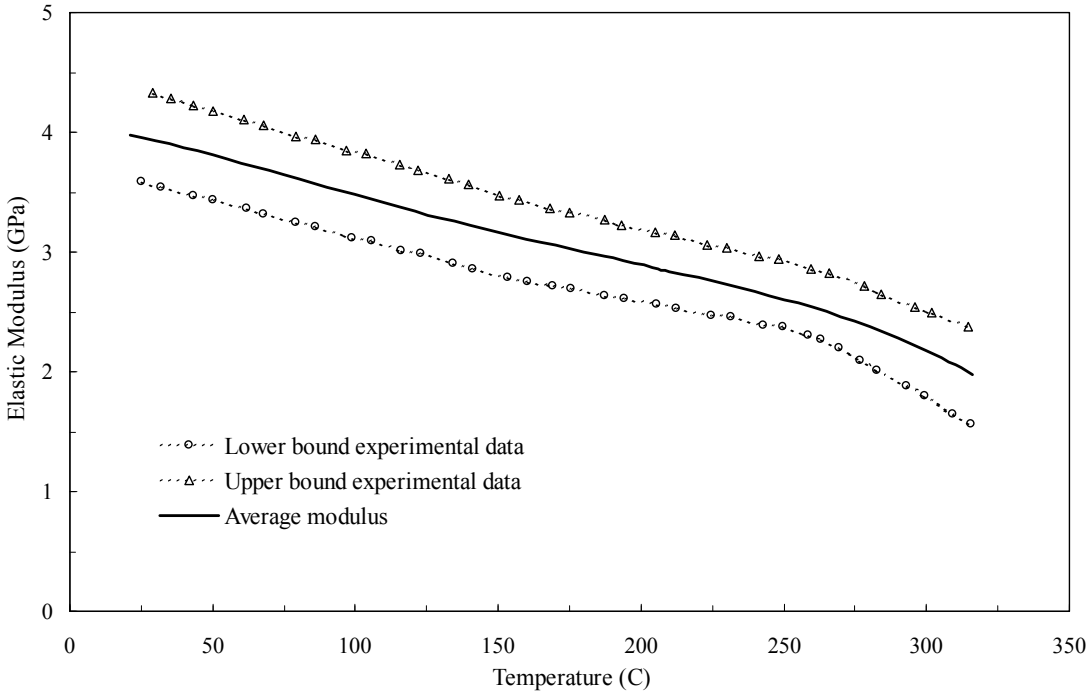

Fig. 3.2 Temperature dependent elastic modulus of PMR-15 polyimide matrix

Within the studied temperature ranges the elastic properties of the carbon fiber is assumed independent on temperatures. The temperature dependent elastic moduli for the polyimide matrix are calibrated using the average values in Fig. 3.2. The fitted function in terms of the temperature-dependent compliance, as shown in Eq. (2.7), is given as:

$$g_0(T) = 5.59\times10^{-8}T^3 - 1.97\times10^{-5}T^2 + 4\times10^{-3}T + 0.9 \tag{3.25}$$

Fig. 3.3 depicts micromodel predictions of the elastic properties of graphite/PMR-15 polyimide unidirectional composites at different temperatures. The elastic moduli of the polyimide are allowed to degrade as the temperature increases, while the fiber moduli

remain constant within the studied temperature range. Overall, good predictions are observed.

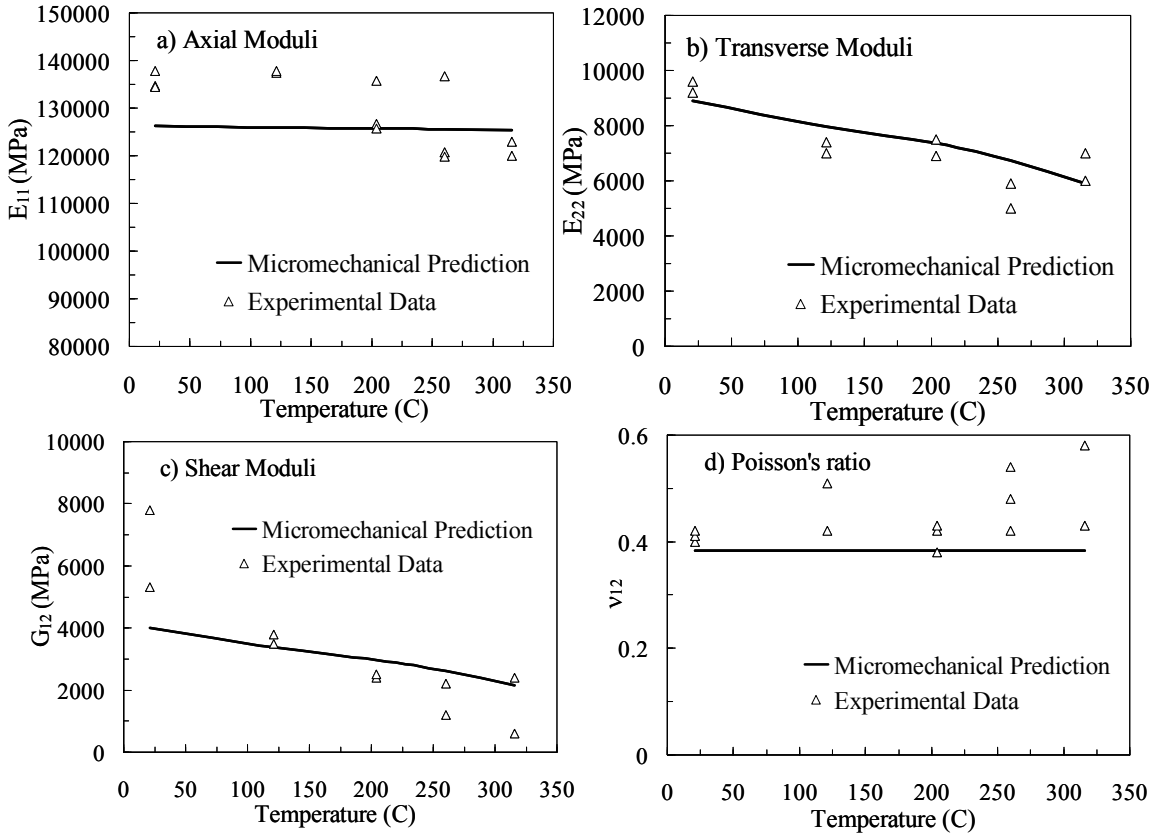

Fig. 3.3 Micromodel predictions of temperature-dependent elastic properties of carbon-polyimide systems with 56% fiber volume fraction

3.2.2 Time-dependent responses of Kevlar-49/epoxy composites

The effective time-dependent responses of FRP composites obtained from the micromechanical model is verified using experimental data of Kevlar-49/epoxy 3501 (KFRP) composites with 63% fiber volume fraction reported by Walruth [83]. Kevlar fiber and epoxy matrix exhibit different time-dependent material responses. Since the

reported data in Walruth [83] are for the effective KFRP composites, as inputs to the micromechanical model we use existing data for the elastic and viscoelastic properties of Kevlar-49 and epoxy-3501. The elastic properties for Kevlar fiber and epoxy matrix are given in Table 3.2.

Table 3.2 Elastic properties for Kevlar-49 and epoxy-3501 matrix

Material	Modulus (GPa)				Poisson's ratio	
	E_{11}	$E_{22}=E_{33}$	$G_{12}=G_{13}$	G_{23}	$\nu_{12}=\nu_{13}$	ν_{23}
Fiber (Kevlar –49)	113-129	6	4.14	3.3	0.40	0.40
Matrix (Epoxy –3501)	4.34				0.36	

A wide variation in axial moduli of the Kevlar-49 fibers between 113-129 GPa is observed in the existing literatures (Wang & Dillard [85]; Walton & Majumdar [84]). The axial modulus of fiber can significantly affect the effective elastic modulus of composites along the axial fiber direction. The proposed micromechanical model is used to obtain effective elastic material properties of the KFRP composites. The axial modulus of the Kevlar-49 is taken as 121 GPa, which is the average value of the upper and lower moduli. The predictions of the effective elastic properties are well compared with the ones reported by [83], which are shown in Table 3.3.

Table 3.3 Effective elastic properties for KFRP composites with 63% volume fraction

Material	Modulus (GPa)				Poisson's ratio
	E_{11}	$E_{22}=E_{33}$	$G_{12}=G_{13}$	G_{23}	. $\nu_{12}=\nu_{13}$
Micromodel	78.1	5.61	2.86	2.65	0.385
Experiment*	77.9	5.60	2.2	1.90	0.4

*Experimental data is obtained from [83]

The Kevlar fiber exhibits transversely isotropic linear viscoelastic responses, while the matrix experiences isotropic viscoelastic response. The creep compliance for the Kevlar-49 fiber in the longitudinal fiber direction is obtained from Walton and Majumdar [84]. The creep compliance for epoxy-3501 resin is obtained from White and Hartman [87]. Prony parameters are used to fit the creep compliances, which are given in Table 3.4.

Table 3.4 Prony parameters for Kevlar-49 and epoxy-3501

		Kevlar-49		Epoxy-3501
N	λn (1/min)	Dn x 10^{-6} (1/MPa)		Dn x 10^{-6} (1/MPa)
		S_{1111}	$S_{2222}=S_{3333}$	S
1	1	0.73	0.07	176
2	10^{-1}	0.071	0.1	5
3	10^{-2}	0.31	2.8	29
4	10^{-3}	0.03	0.44	25
5	10^{-4}	0.48	4.2	35
6	10^{-5}	0.38	0.4	6.8

The axial fiber direction follows time-dependent response, while along the transverse direction, an elastic behavior is assumed. The effective creep compliance in the axial and transverse directions for the KFRP composites is illustrated in Fig. 3.4.

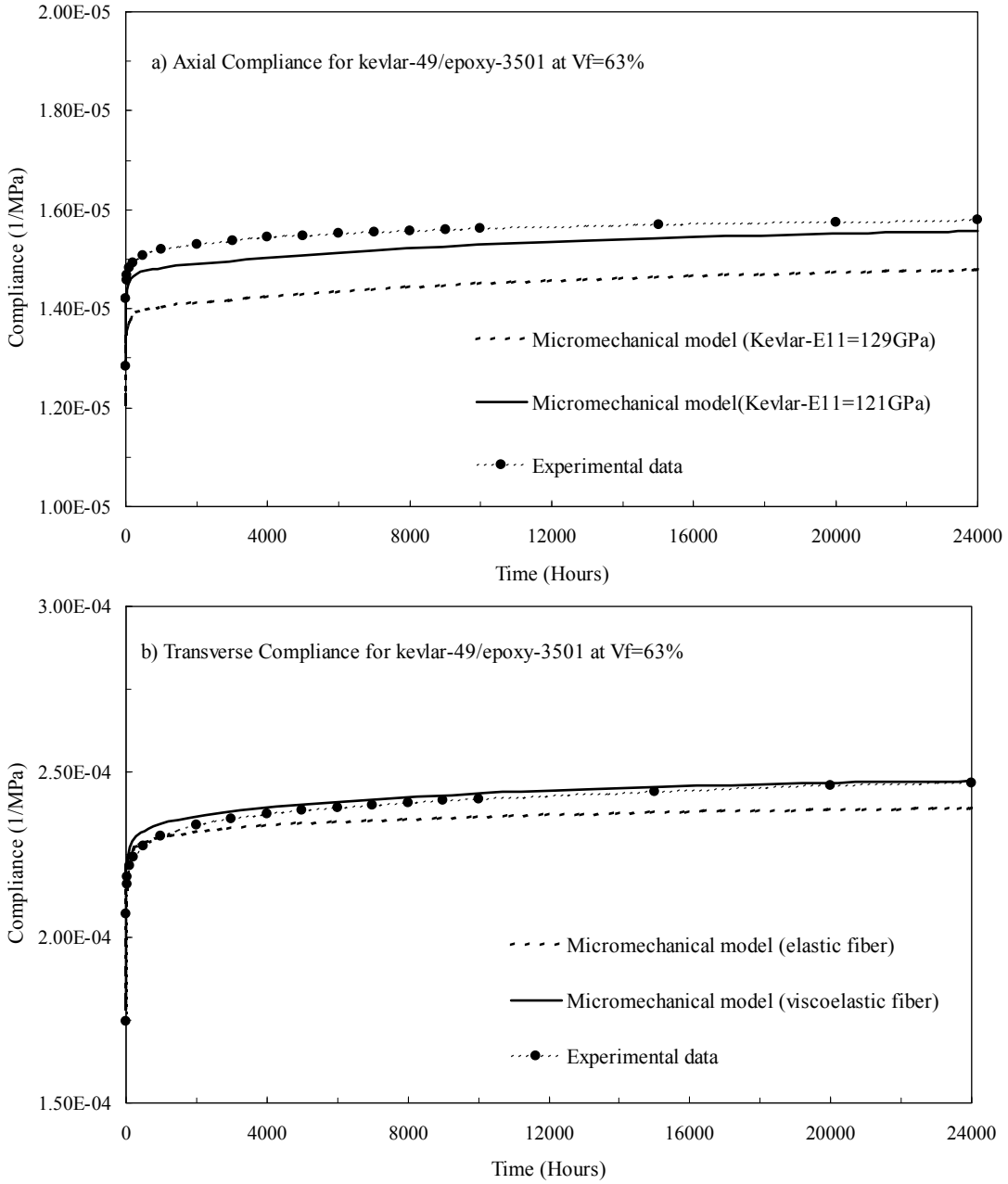

Fig. 3.4 Effective compliances for Kevlar-49/epoxy-3501 composites

The micromechanical model shows good prediction capabilities in the axial fiber direction. Slight mismatch is found in the transverse compliance due to the assumption of linear elastic transverse modulus of Kevlar fibers. As experimental data on the viscoelastic properties of Kevlar in the transverse fiber direction are not available, we calibrated the time-dependent transverse compliance of the fibers by changing the time-dependent parameters in $S_{2222}(t)$ compliance for Kevlar until the overall responses from the micromechanical model match with the ones from the experiments. The calibrated $S_{2222}(t)$ is shown in Table 3.4.

Furthermore, to verify the micromechanical creep responses of KFRP composites at different fiber volume fractions, i.e., 20%, 40%, and 50%, detailed FE meshes of the composite microstructures are generated. Two unit-cell models of the FRP microstructures are considered, as shown in Fig. 3.5. The first unit-cell consists of one-fourth symmetry of one cylindrical fiber embedded in a matrix of a rectangular solid. The second unit-cell consists of two one-quarter fibers placed in a matrix of a rectangular solid. Fig. 3.5 also shows detailed FE model of the idealized FRP microstructures using 3D continuum (C3D8) elements.

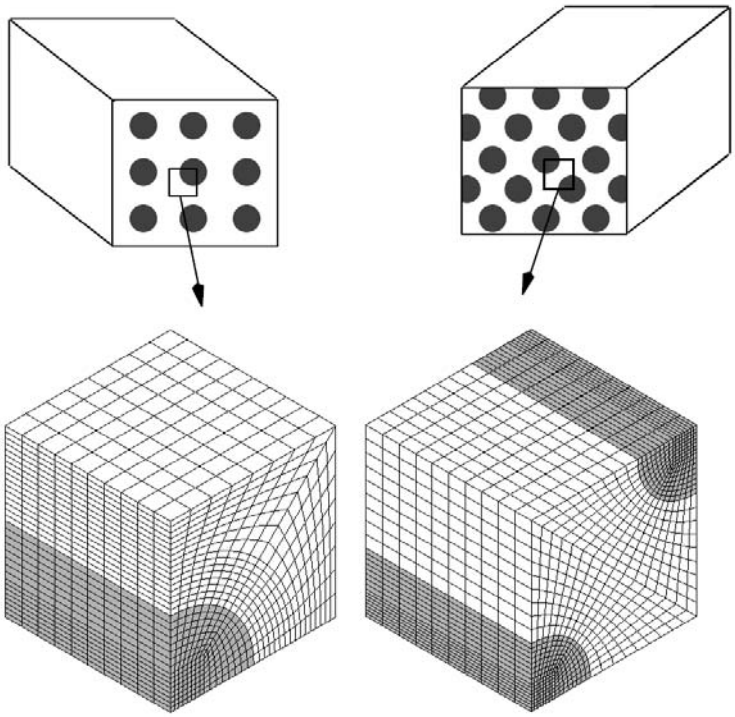

Fig. 3.5 FE model for unidirectional FRP microstructures (idealized microstructures, Vf=20%)

Material parameters for the Kevlar fiber and epoxy matrix are given in Tables 3.2 and 3.4. The time-integration algorithm for nonlinear viscoelastic materials are implemented at each material (Gaussian) points in the finite elements. Creep responses of the composites along axial and transverse fiber directions, which are determined at fixed temperatures, are illustrated in Fig. 3.6.

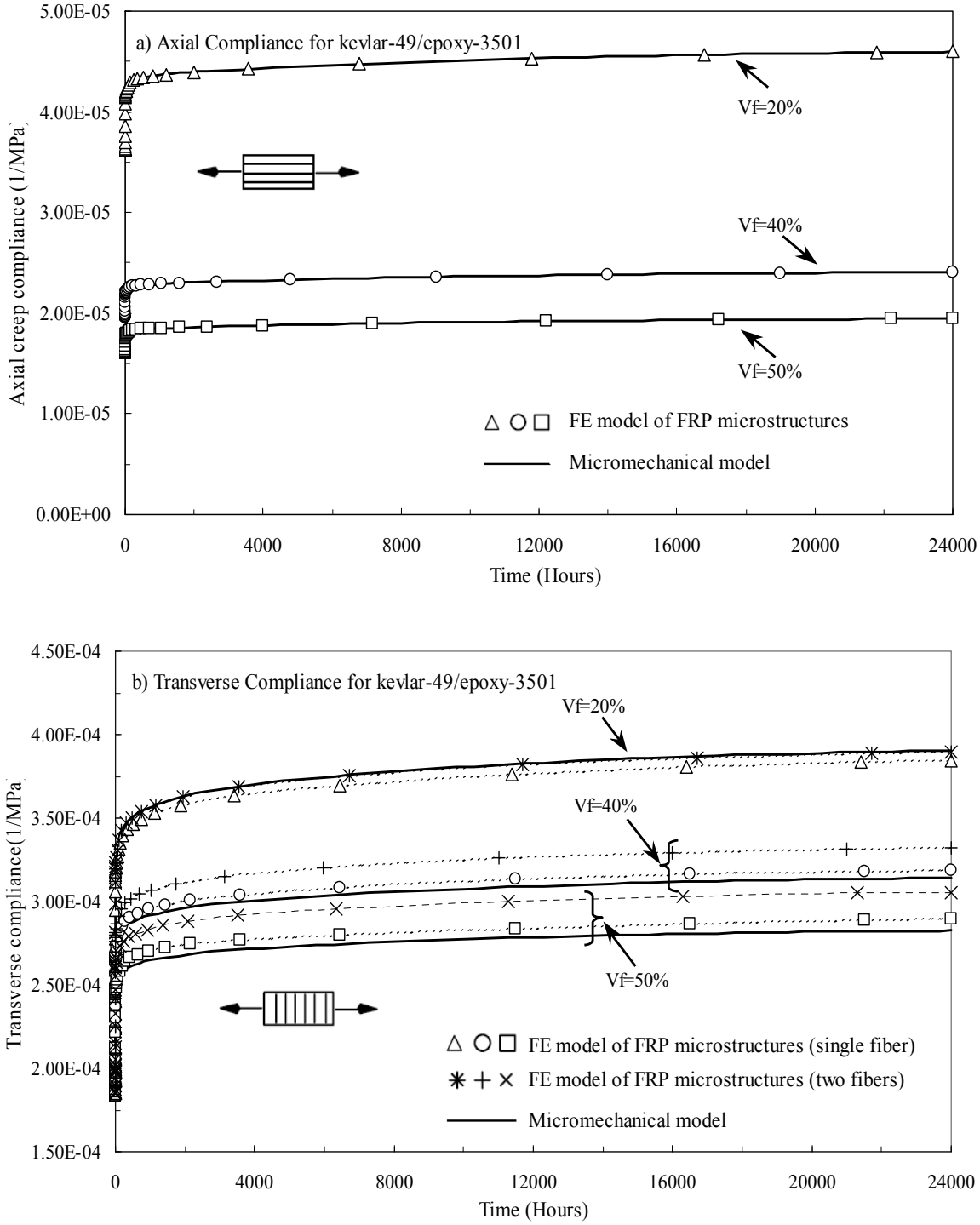

Fig. 3.6 Axial and transverse creep compliances of KFRP composites at 20%, 40% and 60% fiber volume fractions

The axial creep responses obtained from the simplified micromechanical model match very well with the ones generated using the detailed FE microstructures having single and two fibers. The transverse creep compliances generated using the simplified micromodel are in good correlations with the detailed FE micromodel with single fiber inclusion. Slight mismatches are shown in the transverse compliances generated using the simplified micromodel and detailed FE microstructures with two fibers for higher volume fractions. The deviations are between 5.5-8.5%. In the two-fiber FE unit-cell model, as the volume content increases the distant between the two fibers (spacing) is smaller and the transverse loading creates high localized stresses around the fiber spacing. This might be due to the fiber interactions, as shown in Fig. 3.7. It is seen that for composites with 50% fiber volume fractions, the stress gradient in the fiber constituents in the two-fiber model is high compared to the one in the single fiber model. In a single fiber model, a relatively uniform stress is observed in the fiber constituents. The simplified micromechanical model relations are formulated in terms of average stress tensor in the fiber subcell and do not incorporate stress variations in the fibers.

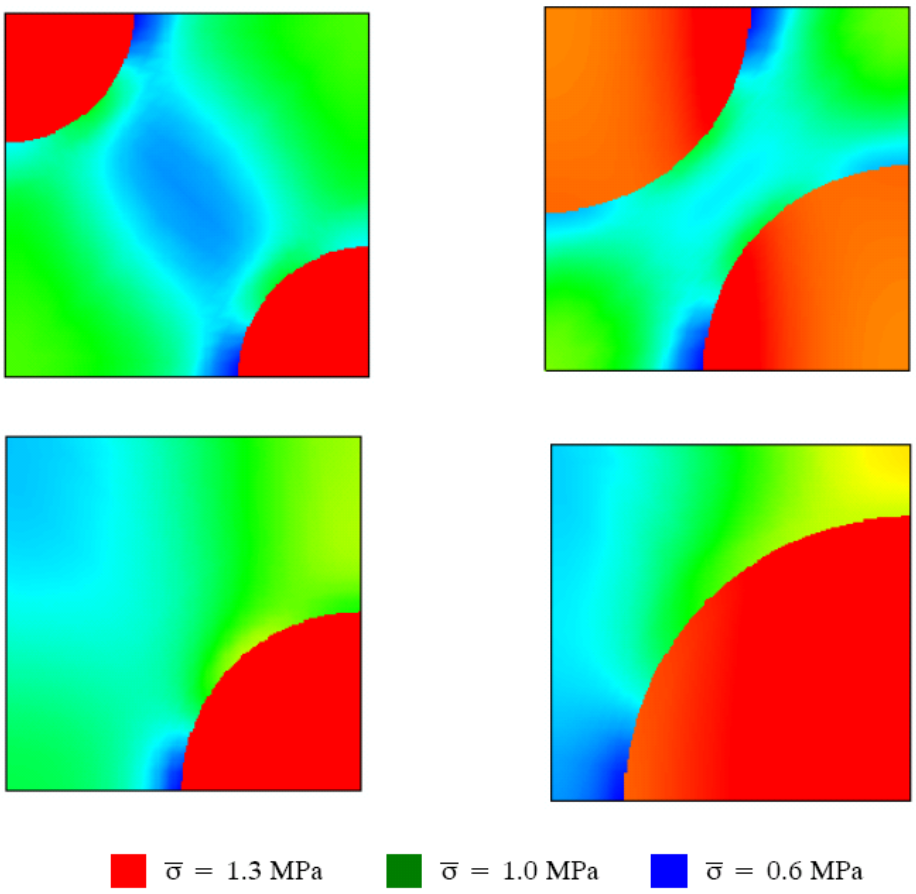

Fig. 3.7 Comparisons of the Von Mises stress contour of FRP microstructures with 20% and 50% fiber volume fractions (results from detailed FE model)

The stress-strain behaviors of the KFRP/epoxy composites at various constant stress rates are also presented. Responses from the micromechanical model are compared with the ones obtained from the detailed FE microstructures having single fiber for composites with 20%, 40%, and 60% volume fractions. Three different stress rates: 0.01, 0.1, and 0.5 MPa/hr are considered. The maximum stress applied is 25% of the ultimate tensile strength at the respective fiber volume fractions. The stress responses against the axial and transverse strains are reported. Fig. 3.8 shows response predictions under loading along fiber directions.

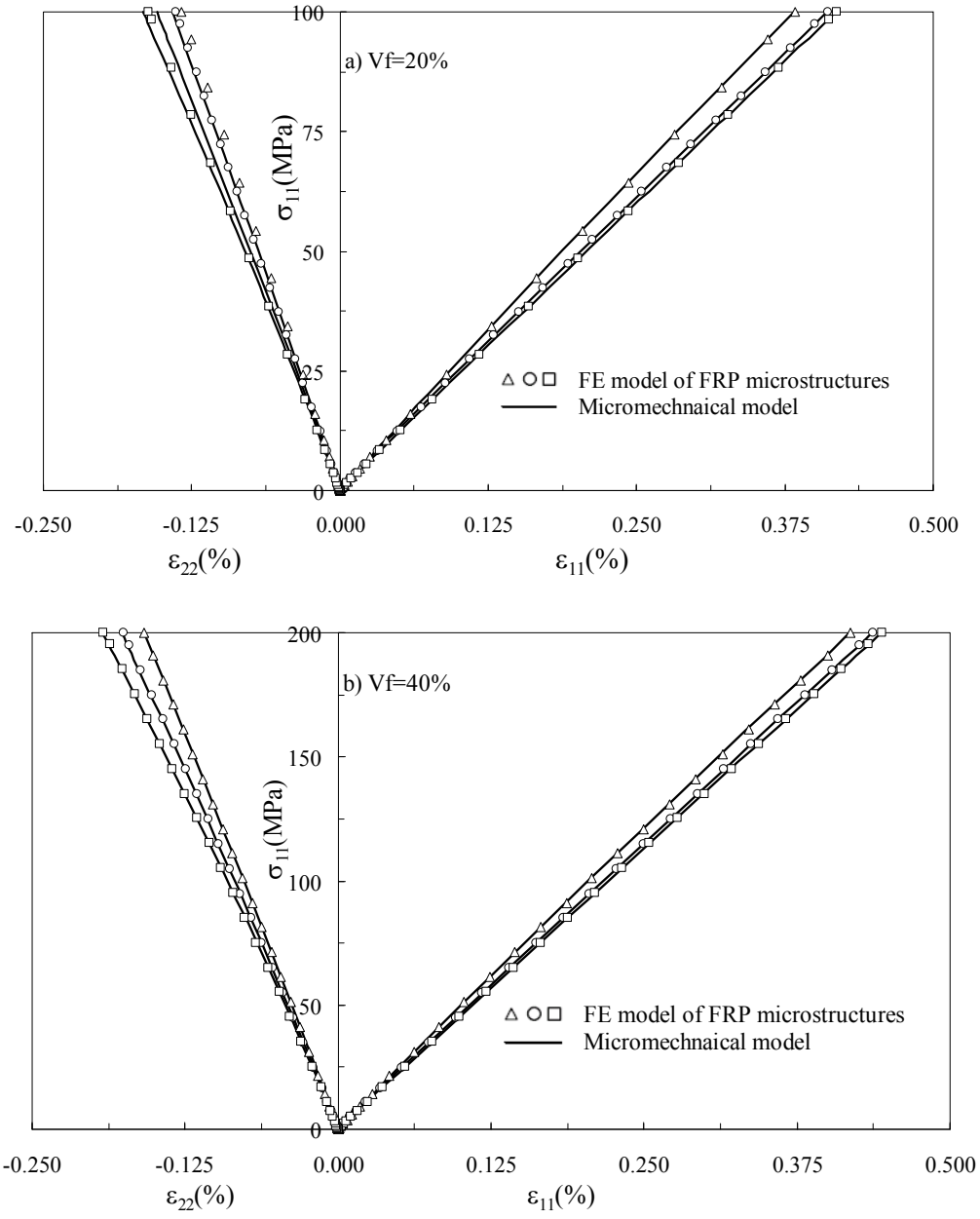

Fig. 3.8 Stress-strain behaviors of Kevlar-49/epoxy composites at various constant stress rates (Δ ≡ r=0.5 MPa/hr, O≡ r=0.1MPa/hr, □≡ r=0.01 MPa/hr)

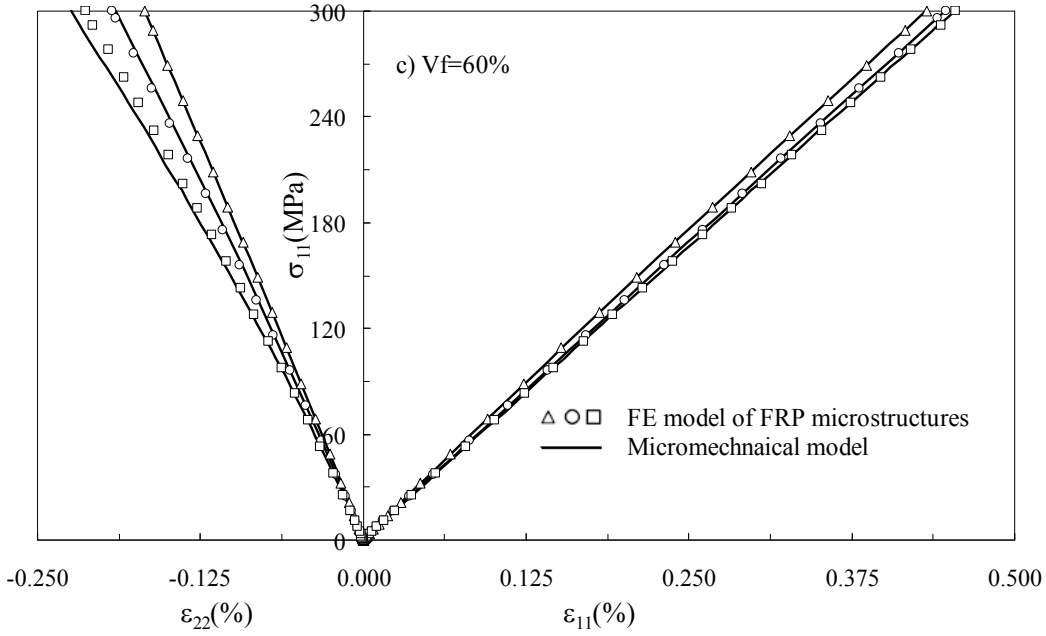

Fig. 3.8 (Continued)

Fig. 3.9 presents stress-strain responses due to loading in the transverse fiber direction. A maximum loading of 10 MPa (~ 25% of ultimate tensile strength of PMR-15 at 250°C) is applied for all fiber volume fractions. The ε_{11} strains due to Poisson's effect are not shown as the rate effects in the axial direction due to transverse loading are found to negligible and the results for all rates overlap each other. The micromodel predictions of the stress-strain responses at different loading rates are comparable to the responses from the FE model of the FRP microstructures.

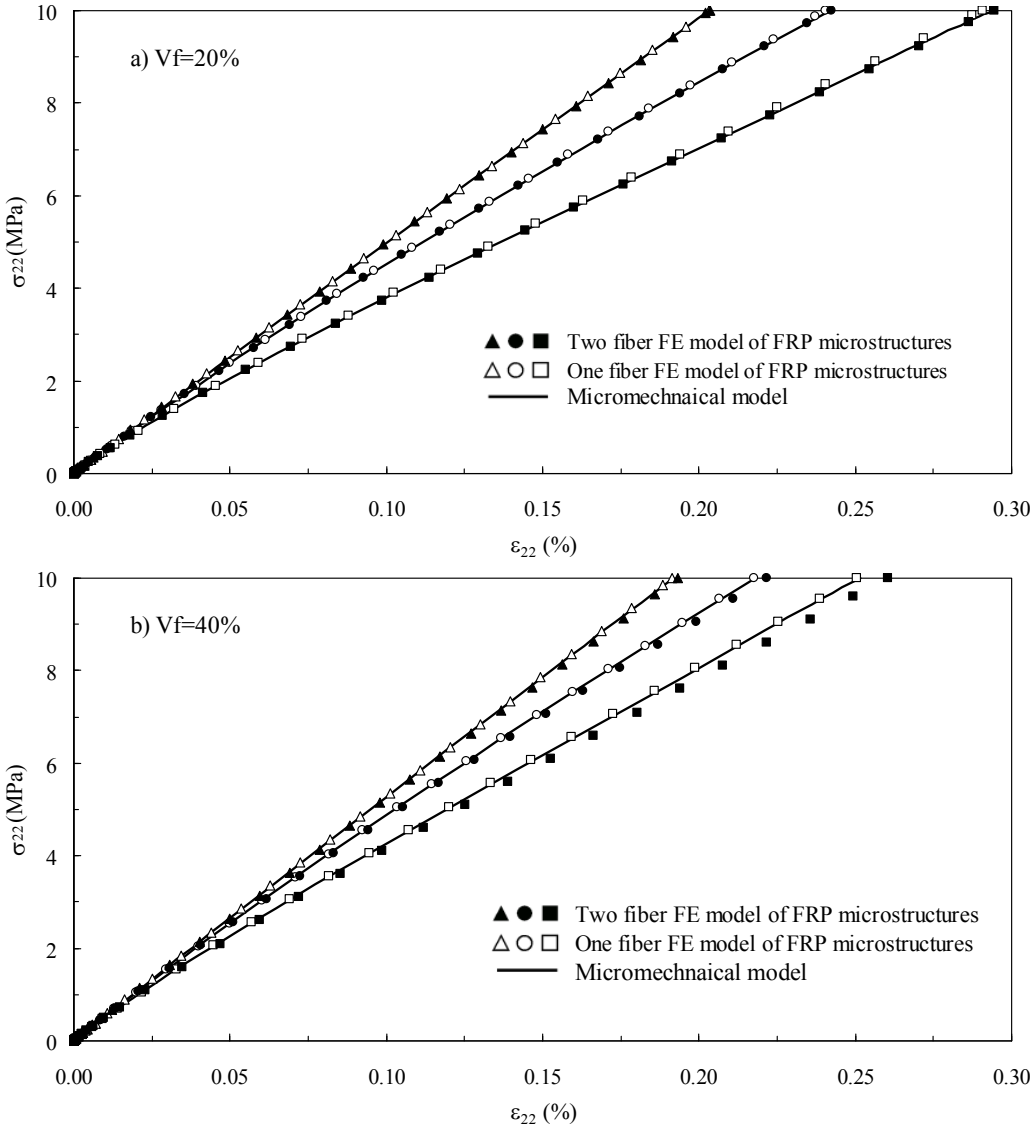

Fig. 3.9 Stress-strain behaviors of Kevlar-49/epoxy composites at various constant stress rates (Δ ≡ r=0.5 MPa/hr, O ≡ r=0.1MPa/hr, □ ≡ r=0.01 MPa/hr)

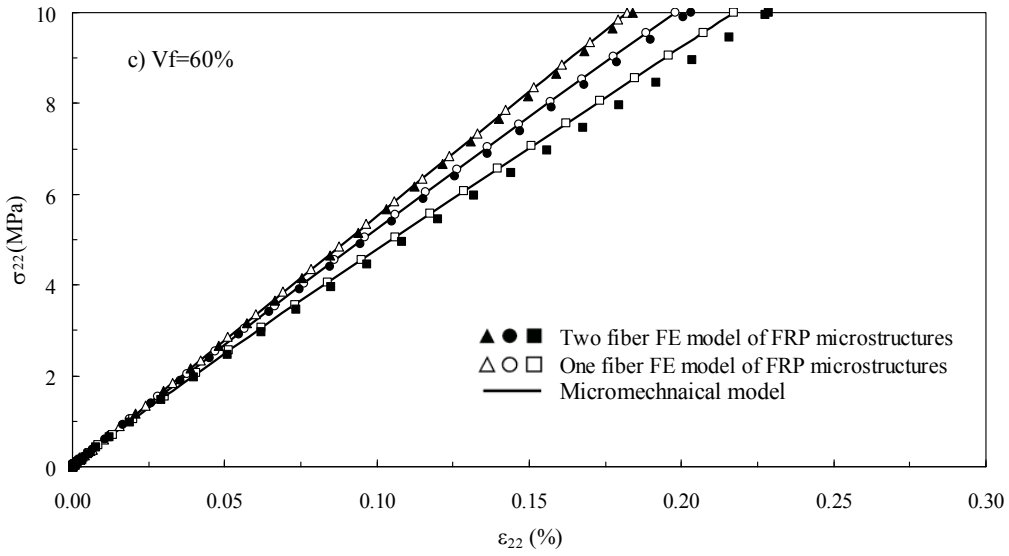

Fig. 3.9 (Continued)

3.2.3 Effective viscoelastic responses of composites subject to mechanical and thermal stimuli

The capability of the simplified micromechanical model in incorporating different time-dependent behaviors of the constituents at various temperatures is presented. The studied FRP systems consist of Kevlar-49 fibers and PMR-15 polyimide matrix, which exhibit different time-dependent properties. Hanson [34] has studied the feasibility of Kevlar-49/PMR-15 composite for high temperature aerospace structures. It was observed that polyimide resin PMR-15 provides thermo-oxidative and hydrothermal stability even at relatively high temperatures. A significant reduction in baseline flexural modulus and strength was observed with increase in temperature from 25^{o}C to 316^{o}C. Degradation in the FRP modulus was also observed during a long-term exposure (1500 hrs) at 285^{o}C. In this study, time-dependent material properties for the Kevlar-49 fibers, given in Table 3.4, are used, while the viscoelastic responses of the PMR-15 are taken

from [48]. Marias and Villoutreix [48] has characterized 5-hour creep behavior of PMR-15 at several temperatures (250°C-300°C). Experimental creep responses of PMR-15 polyimide at temperatures: 250°C, 275°C, 285°C, and 300°C are illustrated in Fig. 3.10. The elastic properties of the PMR-15 at room temperature are E=3625 MPa and ν=0.3 and the calibrated time-dependent properties (Prony parameters) of the PMR-15 are given in Table 3.5.

Table 3.5 Prony parameters for PMR-15 matrix

N	λn (1/hour)	Dn x 10^{-6} (1/MPa)
1	30	7.5
2	10	7
3	2	20
4	1	10
5	0.5	2
6	0.1	19
7	0.01	190
8	0.001	850

The temperature-dependent parameters for the PMR-15 are:

$$\begin{aligned} g_0(T) &= 5.59\times10^{-8}T^3 - 1.97\times10^{-5}T^2 + 4.01\times10^{-3}T + 0.9 \quad T \text{ is in } {}^0C \\ g_1(T)g_2(T) &= 3.116\times10^{-5}T^3 + 2.777\times10^{-2}T^2 - 8.1196T + 782.01 \\ a(T) &= 1.333\times10^{-5}T^3 - 1.1\times10^{-2}T^2 + 3.0087T - 272 \end{aligned} \tag{3.26}$$

Instead of recalibrating parameter g_0(T), which describes the variation of the elastic (instantaneous) modulus of PMR-15 with temperature, previously calibrated $g_0(T)$ parameter in Eq. (3.25) from Rupnowski et al. [71] is used. This is done to evaluate the

consistency of the temperature-dependent material parameters obtained from different sets of experimental data. To calibrate temperature-dependent parameters $g_1g_2(T)$ and $a(T)$, first attempt is to use only the time-temperature shifting parameter $a(T)$ for representing experimental creep responses at various temperatures reported in [48]. This describes thermo-rheologically simple behaviors. However, using only $a(T)$ parameter does not provide a good fit in representing creep responses at higher temperatures (285°C & 300°C). The second attempt is to include temperature dependent parameters $g_0(T)$ and $g_1g_2(T)$ described in Eq. (2.11). A good fit to experimental data is achieved even at high temperatures. The capability of the time-integration algorithm presented in Eqs. (2.11) and (2.31) in predicting creep responses at various temperatures is illustrated in Fig. 3.10. Good response predictions are shown.

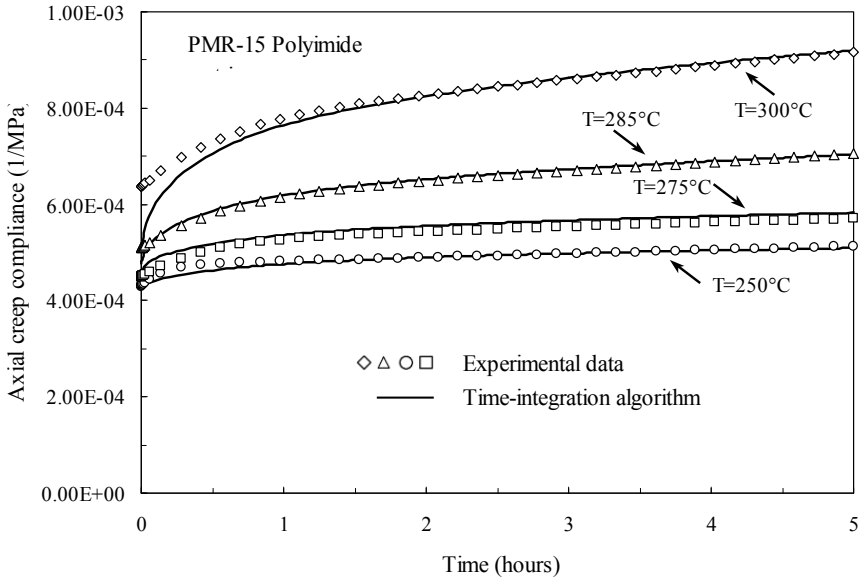

Fig. 3.10. Creep compliance for PMr-15 matrix at various temperatures

FE model of detailed FRP microstructures, shown in Fig. 3.5, is used to simulate creep responses of Kevlar-49/PMR-15 composites having 20% fiber volume fraction at various temperatures. The viscoelastic properties of the Kevlar fiber are assumed independent on temperatures and stresses, while the temperature dependent viscoelastic properties of PMR-15 are taken from [48]. The purpose is to verify the capability of the simplified micromodel in predicting effective thermo-viscoelastic responses of Kevlar-49/PMR-15 composites. Fig. 3.11 shows micromodel predictions of thermo-viscoelastic responses of Kevlar-49/PMR-15 composites in axial and transverse fiber directions. The responses from the simplified micromodel are comparable to the ones obtained from the detailed FE microstructures.

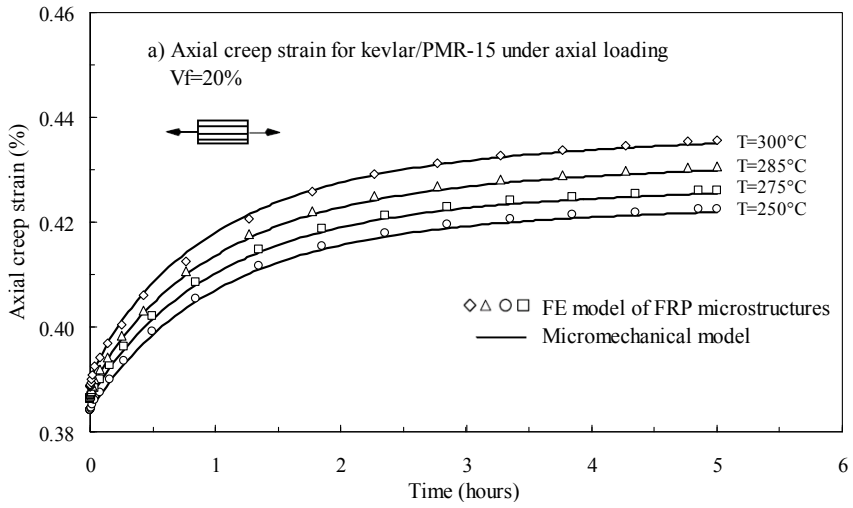

Fig. 3.11 Axial and transverse creep strains for Kevlar-49/PMR-15 composites at volume fraction 20% and T=250, 275, 285 and 300°C

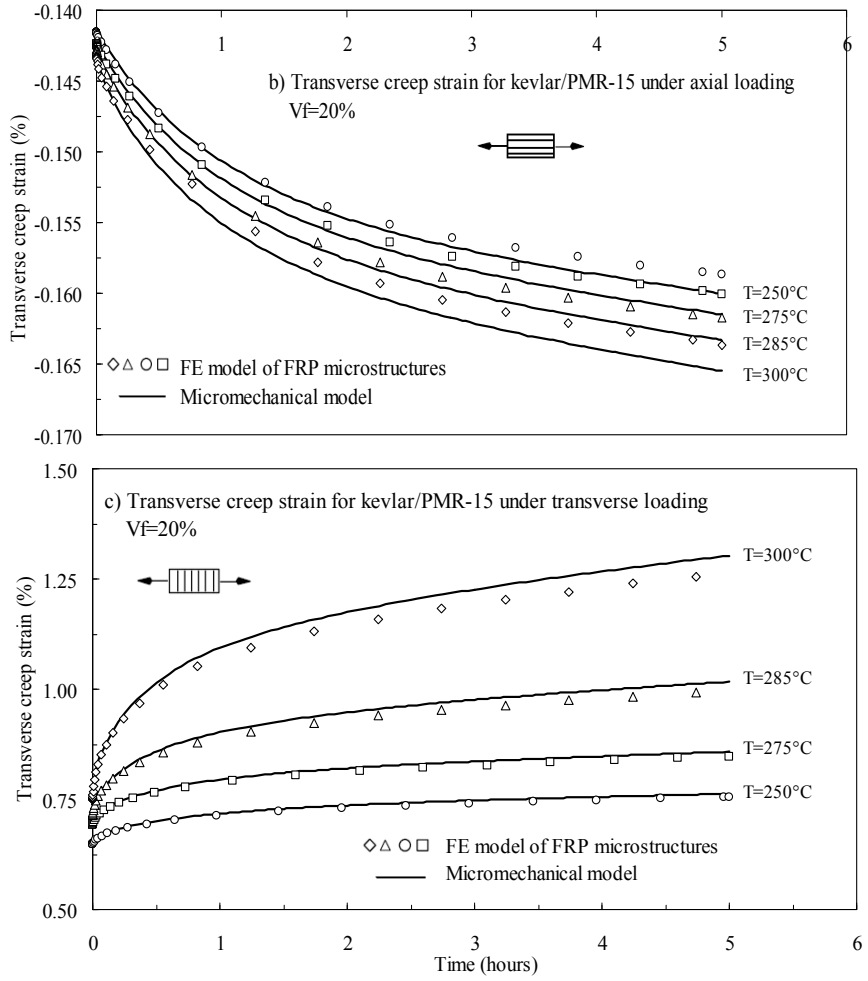

Fig. 3.11 (Continued)

3.2.4 Effective viscoelastic responses of composites with linear viscoelastic fiber and nonlinear stress and temperature dependent viscoelastic matrix

The verifications are also performed for a FRP composite with linear viscoelastic fiber and a stress-temperature dependent nonlinear viscoelastic matrix. For this purpose, Kevlar-49 fiber and epoxy AF-191 resin is considered. The elastic and time dependent properties of the constituents are obtained from literature (Walton & Majumdar [84],

Peretz and Weitsman [63]). The elastic and linear viscoelastic properties (in terms of Prony series) for the fiber and matrix constituents are already mentioned in Tables 2.8, 2.9, 3.2 and 3.4. The nonlinear stress and temperature dependent parameters for epoxy are already given in Eqs. (2.38).

The analysis is carried for a time of 3600 seconds at different values of axial creep loading for different fiber volume fractions as given in Fig. 3.12. The responses from the micromechanical models are compared to the ones from the detailed FE models of FRP microstructures. The verification is also performed for same value of creep load ($0.6Sut_{matrix}$) in the transverse fiber direction for different fiber volume fractions. The available experimental data for epoxy resin in [63] is for a maximum temperature of 60°C and epoxy shows a high nonlinearity at this temperature. The verifications are performed for this temperature. The results are shown in Fig 3.12. For both the cases, the results of the micromechanical analysis compare very well with the detailed 3D analysis.

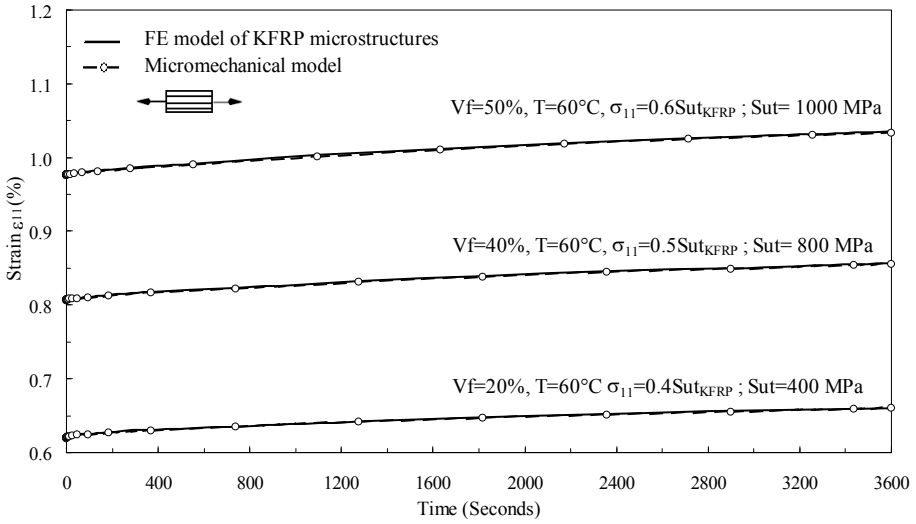

Fig. 3.12 Axial and transverse creep strains for Kevlar-49/AF-191 epoxy composites with stress-temperature dependent nonlinear viscoelastic matrix

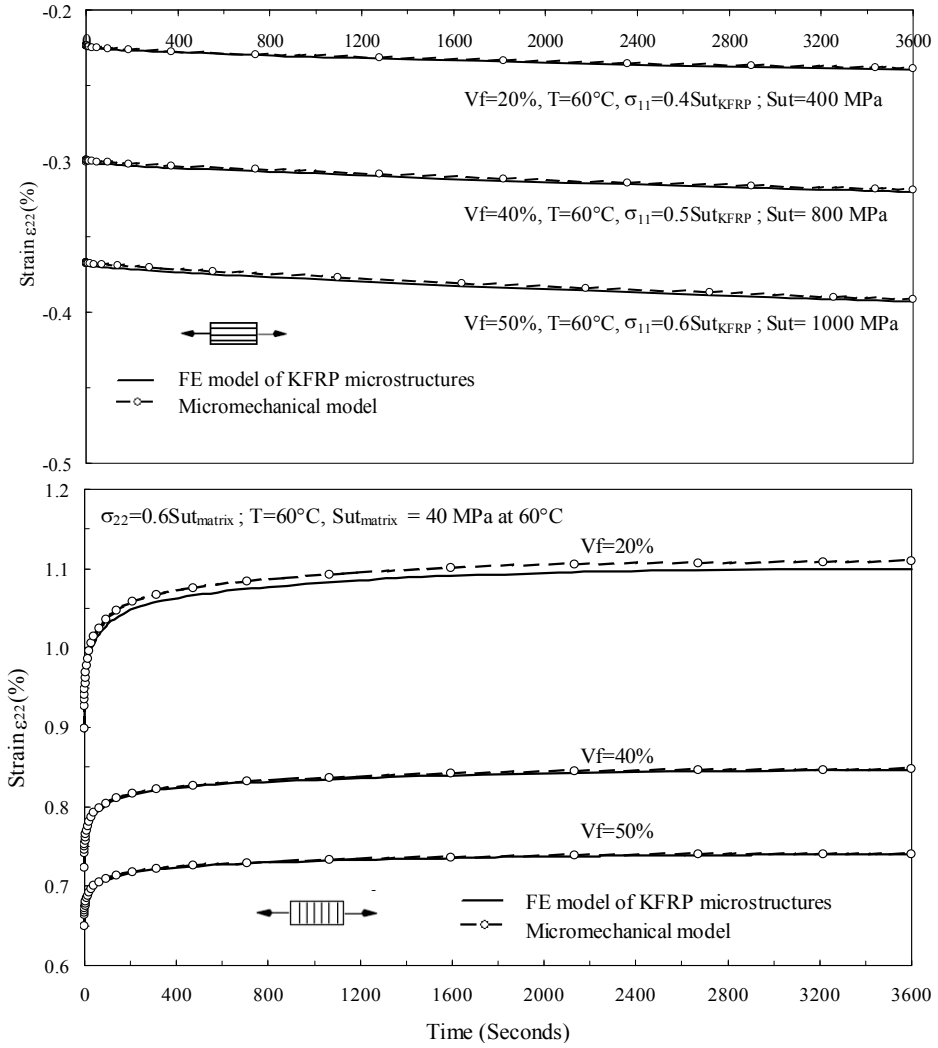

Fig. 3.12 (Continued)

3.2.5 Effective viscoelastic responses of composites with stress dependent nonlinear viscoelastic fiber and nonlinear stress and temperature dependent viscoelastic matrix

The final verification is performed for a unidirectional composite with stress dependent nonlinear viscoelastic fiber and stress and temperature dependent nonlinear viscoelastic matrix. The fiber-matrix system considered is same as that for the previous

analysis i.e. Kevlar-49 and epoxy AF-191 resin. Due to limited experimental data for nonlinearity of fiber, reasonable hypothetical nonlinear data for Kevlar-49 fiber is used and the nonlinear parameters are given by the following equations:

$$g_0(\bar{\sigma}) = \begin{cases} 1 & for\ \bar{\sigma} < 500\text{MPa} \\ 1 + 0.05\left(\dfrac{\bar{\sigma}}{\sigma_o}\right) & for\ \bar{\sigma} \geq 500\text{MPa} \end{cases}$$

$$g_1 g_2(\bar{\sigma}) = \begin{cases} 1 & for\ \bar{\sigma} < 500\text{MPa} \\ 1 + 0.75\left(\dfrac{\bar{\sigma}}{\sigma_o}\right)^2 & for\ \bar{\sigma} \geq 500\text{MPa} \end{cases} \qquad (3.27)$$

$$a(\bar{\sigma}) = \begin{cases} 1 & for\ \bar{\sigma} < 500\text{MPa} \\ e^{-0.2\left(\frac{\bar{\sigma}}{\sigma_o}\right)} & for\ \bar{\sigma} \geq 500\text{MPa} \end{cases}$$

where σ_o = 500MPa

The analysis is carried for axial creep loading under the same stress levels and temperature level (60°C) as the previous analysis. The results of simplified micromodel shown in Fig. 3.13 indicate a good match with those from detailed FE microstructures.

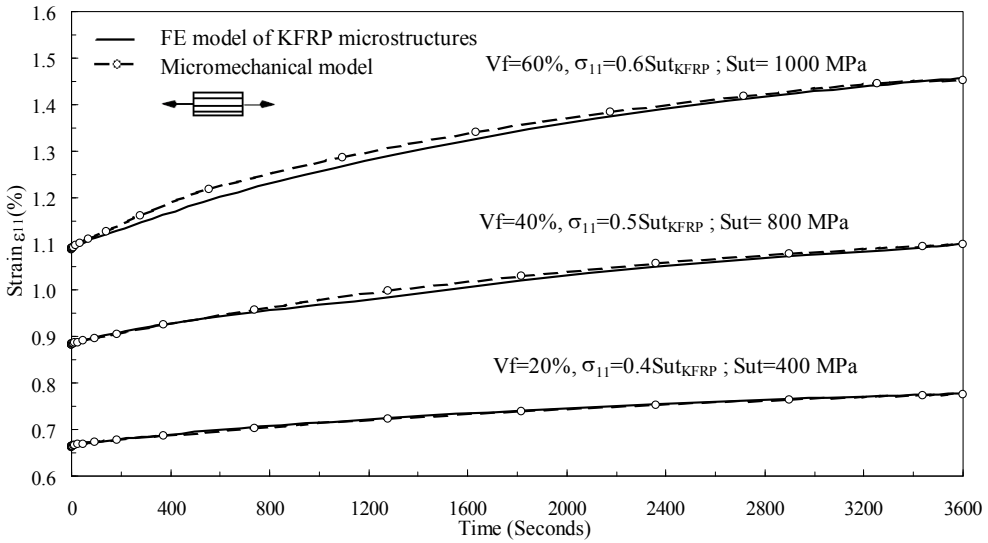

Fig. 3.13 Axial and transverse creep strains for Kevlar-49/AF-191 epoxy composites with stress dependent nonlinear viscoelastic fiber and stress-temperature dependent nonlinear viscoelastic matrix

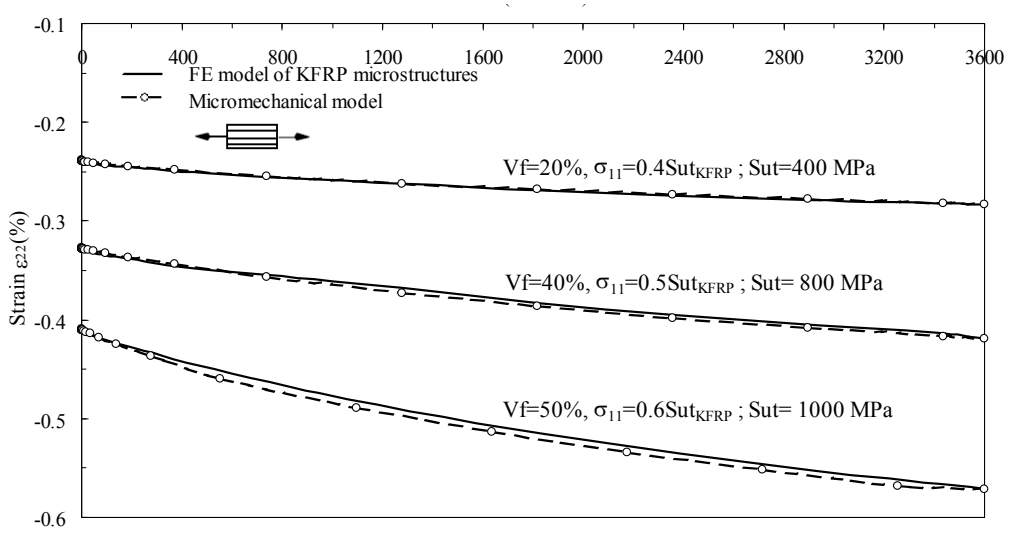

Fig. 3.13 (Continued)

3.3 PREDICTION OF VISCOELASTIC RESPONSE UNDER A GENERAL STRESS AND TEMPERATURE HISTORY

In this section, the viscoelastic response under a various general stress and temperature histories of loading is predicted. The FRP system considered here is Kevlar-49/epoxy AF191 with similar nonlinearity as in the previous verification. A fiber volume fraction of 40% is assumed. The general loading histories for stress along fiber direction and temperature histories are shown in Figs. 3.14 and 3.15 respectively. Similar loading histories are used along transverse fiber direction but the maximum stress applied is 30 MPa instead of 480 MPa.

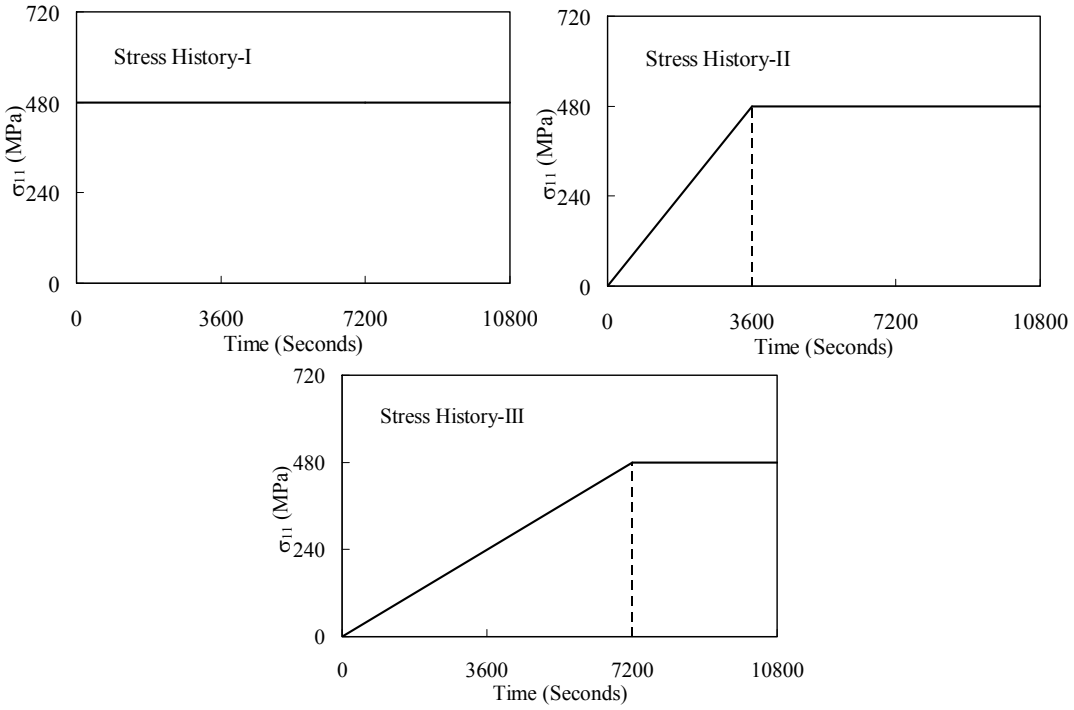

Fig. 3.14 General loading history for stress applied along fiber direction

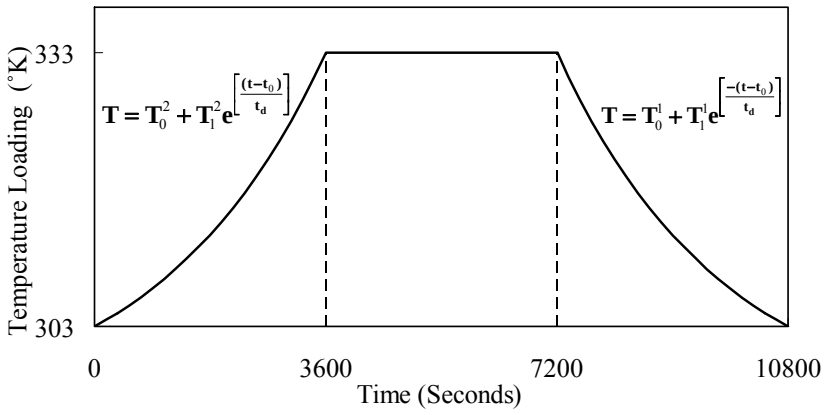

Fig. 3.15 General temperature loading histories

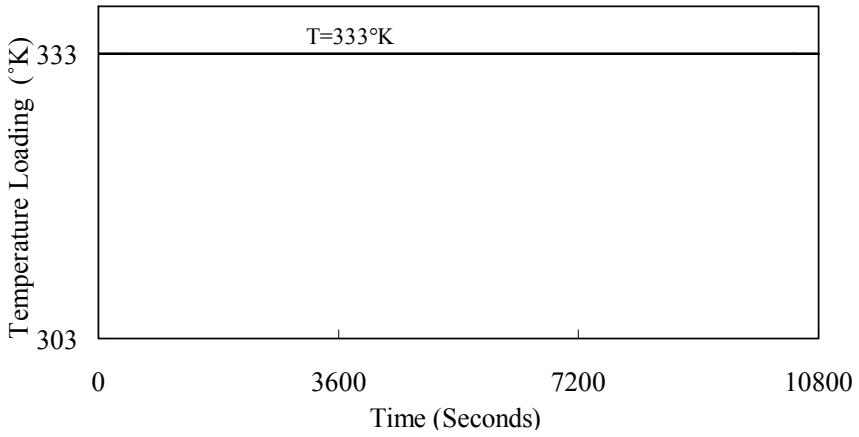

Fig. 3.15 (Continued)

The strain-time curves for combined stress and temperature loading with stress applied along fiber direction is shown in Fig. 3.16. The effect of the two different temperature histories for fiber direction loading is observed to be negligible (and hence the results are reported for only one temperature history). This is because in this case, the response is governed by the fiber properties and a temperature independent fiber is assumed. The three responses for the three different stress histories show the effect of loading history on the responses. It is observed that creep strains are accumulated during the gradual ramp-up of loading to maximum level. The difference in the strain at the final time also indicates the effect of stress history on the responses.

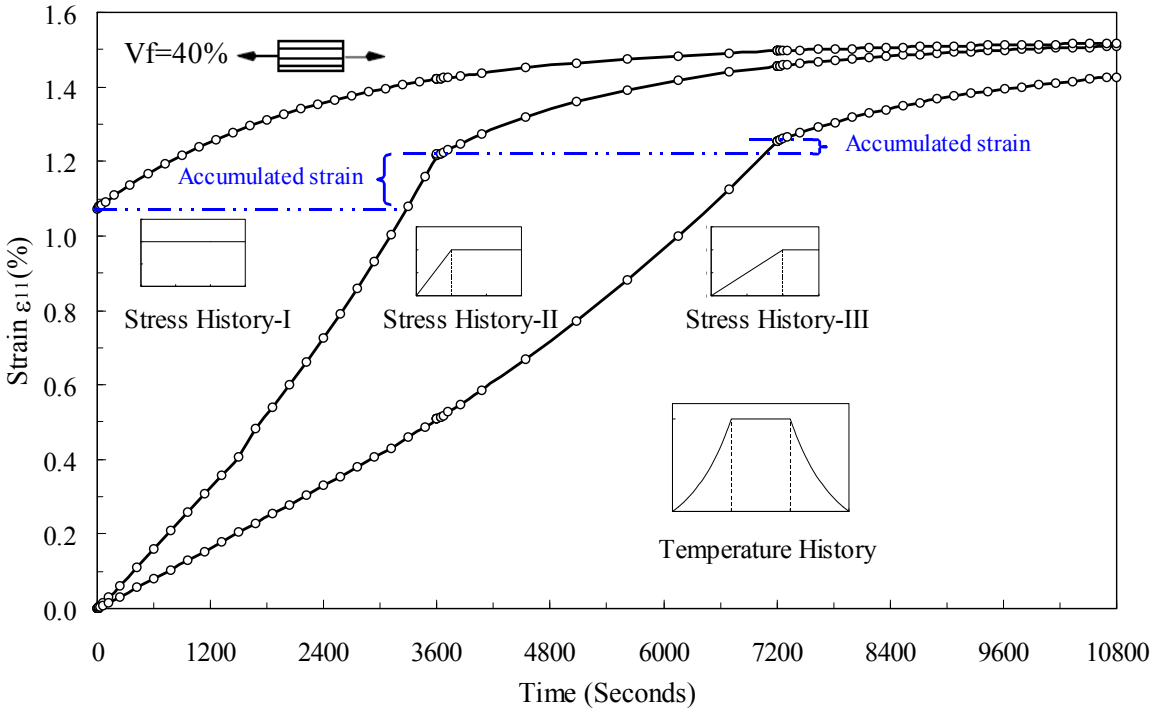

Fig. 3.16 Strain-time responses along fiber direction under general fiber-direction stress and temperature loading histories

The responses for transverse loading and similar stress and temperature histories are shown in Fig. 3.17. In this case, the effect of different temperature histories is observed due to the contribution of the nonlinear temperature dependent matrix.

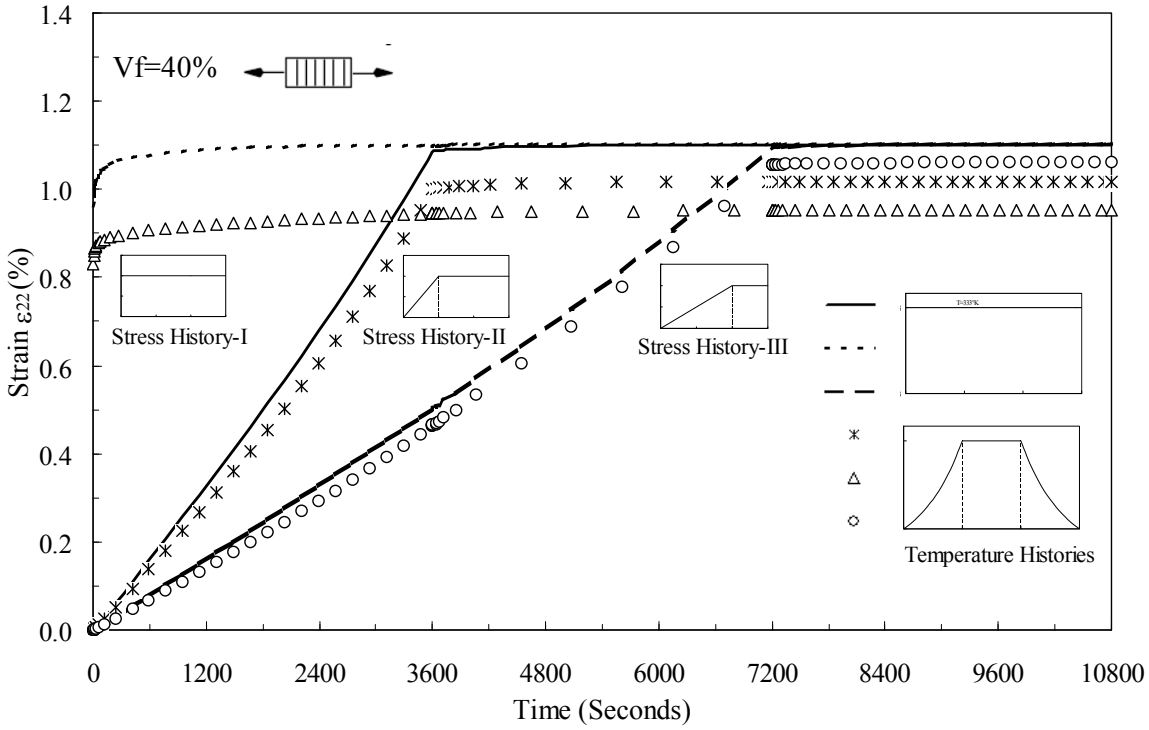

Fig. 3.17 Strain-time responses along transverse fiber direction under general transverse fiber-direction stress and temperature loading histories

This completes the discussion on the prediction of viscoelastic responses using the micromechanical algorithm. The application of this algorithm within the multi-scale framework is discussed in the next chapter.

CHAPTER IV

A MULTI-SCALE FRAMEWORK FOR NONLINEAR VISCOELASTIC ANALYSES OF FIBER METAL LAMINATES

This chapter presents a multi-scale framework for predicting effective nonlinear thermo-viscoelastic responses of FML by incorporating different nonlinear viscoelastic constitutive models for the fiber, polymer matrix, and metal lamina. Two approaches are introduced to analyze the FML. The first approach uses a layered composite element within the finite element (FE) framework having multiple integration points through the thickness. The constitutive material models for the metallic and FRP layers are implemented separately at each material point. The second approach uses a sublaminate model to first homogenize responses of the metallic and FRP layers. The outcome of the sublaminate model is a 3D orthotropic thermo-viscoelastic response, which is implemented at the material/Gaussian points in a general shell or 3D continuum elements. The use of the sublaminate model can reduce the computational cost with limitation in recognizing the sequence of the layers and inter-laminar stresses. The algorithm discussed in chapter II is used to obtain the thermo-viscoelastic responses for each constituent. It is also possible to incorporate the micromechanical model developed in chapter III for the FRP layer within the two approaches mentioned above. Experimental data from the literature on the effective creep responses of FML are used to verify the modeling approaches. The approaches are compared in terms of computational costs as well.

Stress correction schemes are also formulated and used at every scale in the multi-scale framework. These schemes are introduced to solve nonlinear constitutive material models within the FE framework. At every incremental time, linearized solution is obtained followed by an iterative procedure to minimize errors from the linearization. The linearized predictor-corrector schemes are performed simultaneously at the structural (finite element) levels, sublaminate level, FRP micromechanical level and the constituent levels. This is done to ensure accurate responses and accelerate convergence. The effect of multiple scales of the stress correction (predictor-corrector) schemes on the overall nonlinear responses of the FML is also studied.

4.1 MULTI-SCALE FRAMEWORK FOR THE ANALYSIS OF FML

The multi-scale framework for analyzing responses of FML is shown in Fig. 4.1. The upper level illustrates FE structures made of FML. Layered composite continuum/shell elements and standard continuum/shell elements can be used.

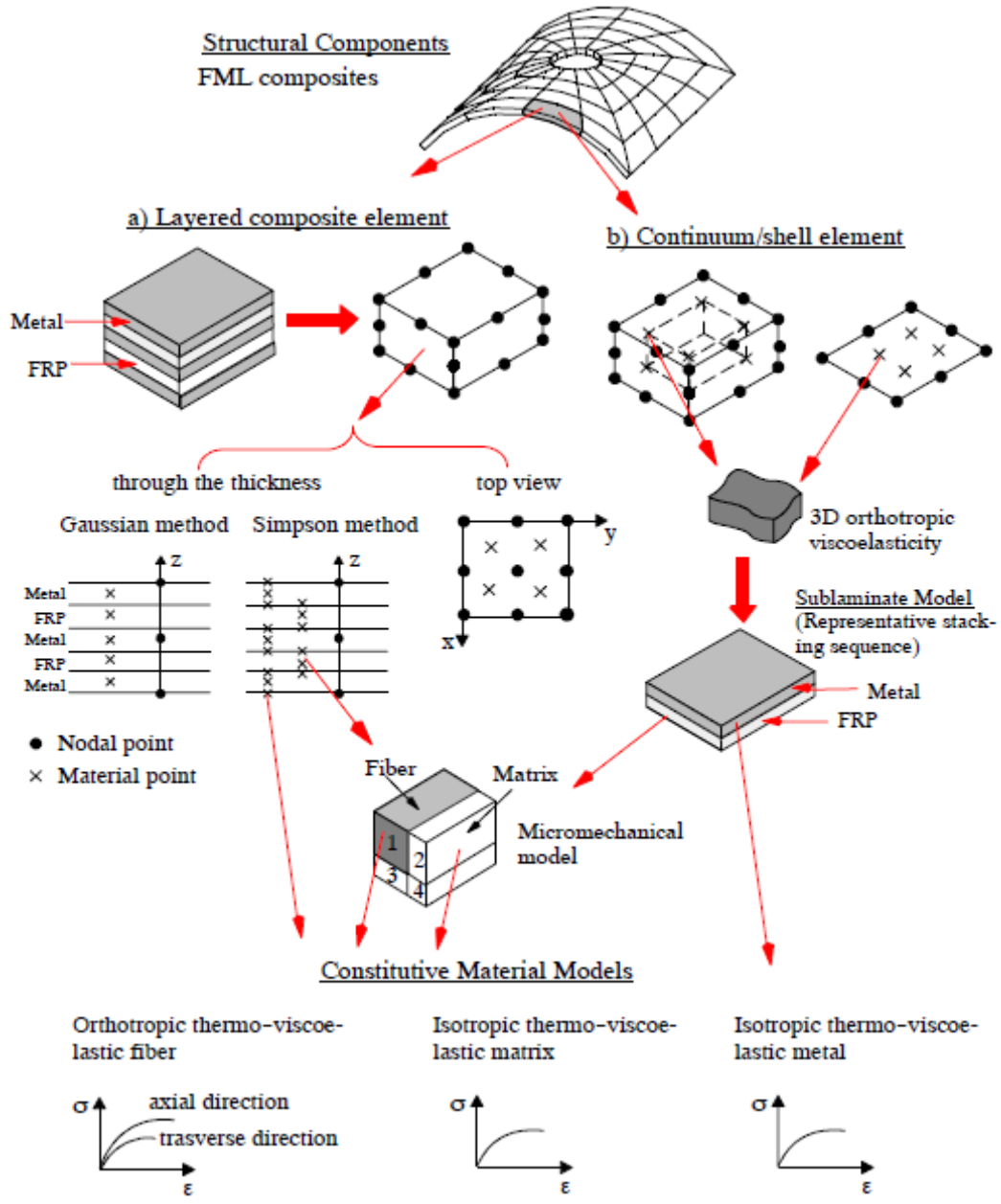

Fig. 4.1 Multi-scale framework for analysis of FML

Two multi-scale approaches are considered:

1. Using layered composite elements with multiple integration (Gaussian) points through the thickness. The constitutive material models for the metallic and FRP layers in the FML are sampled at the integration points (Fig. 4.1 a).
2. Using a sublaminate model to homogenize the viscoelastic responses of the metal and FRP layers in the FML. The outcome from the sublaminate model is a 3D anisotropic viscoelastic constitutive relation, which is sampled at the Gaussian points of a 3D continuum or a shell element (Fig. 4.1 b). In the case of shell elements are used, a plane stress condition must be imposed to the 3D sublaminate constitutive model.

In the first approach, the constitutive viscoelastic material models are calculated at the respective Gaussian points, which represent the FRP and aluminum layers of the FML. The algorithm for modeling the viscoelastic constitutive behavior of orthotropic materials (discussed in chapter II) is used for the FRP layers. The nonlinearity due to stress and temperature is incorporated. This algorithm can also be easily reduced to obtain the viscoelastic responses for isotropic metal in the FML. In the second approach, the response obtained for the FRP and metallic layer is first homogenized using a sublaminate model. A previously developed sublaminate model [31] is modified to incorporate the FRP and metallic layers. The average stresses and strains across the effective FML related to the average stresses and strains in each layer. The homogenized anisotropic response of the FML is then sampled at the Gaussian points of a 3D continuum element.

In both approaches, it is also possible to incorporate the micromechanical model developed in chapter III for the unidirectional FRP layers of FML. This is achieved by integrating the nonlinear viscoelastic constitutive models for the constituents (transversely isotropic fiber and isotropic matrix) into the micromechanical model of unidirectional FRP and then integrating the responses obtained from the micromodel to the layered composite element or to the sublaminate models. The use of micromechanical model is very useful for the design of FML with various combinations of fiber and matrix systems and of different fiber volume fractions.

4.2 THERMO-VISCOELASTIC ANALYSIS OF FML USING LAYERED COMPOSITE ELEMENTS

4.2.1. Implementation of constitutive models for the homogenous FRP and metal layers

In general, FML form thin section composites such that the effects of transverse shear deformation on the overall responses of the FML are less significant. Furthermore, the aluminum layers provide the lay-up with significant transverse shear stiffness. Hence, the layered composite shell elements based on the ESL theories; especially the first order shear deformation theory (FSDT) is sufficient to obtain the overall response of FML. These layered shell elements that are based on the first order transverse shear flexible theory allow for a constant shear deformation across the thickness. Appropriate shear correction factors are also required for the element. It is possible to use a layered continuum solid composite element for the analysis of multi-layered materials. Such an

element is available in ABAQUS FE code. Layered 3D continuum elements are formulated for convenience of multi-layered material modeling and usually only one element with multiple integration points is used through the thickness as illustrated in Fig. 4.1. The detailed 3D stress-strain relations for the FRP and metal are obtained at each material point. This approach gives average values of the out of plane stiffness. In case of one integration point per layer, average stress and strain variation across thickness is obtained for each layer, which is sampled at the mid-layer. In this case, the linear layered element is comparable to the CLT where a linear variation of displacement through the thickness of the laminate is assumed.

A typical linear layered composite brick element and the corresponding isoparametric element are shown in Fig. 4.2. The layer thickness, i.e, the lamina stacking direction, is represented along the z (or t) direction. This element uses Lagrangian interpolation functions to interpolate the displacement fields. It should be noted that the layered composite element has the same level of p-refinement (same order of displacement interpolation function) in all three directions (including the thickness direction) similar to a homogenous continuum brick element. The stiffness formulation for a typical linear layered composite 3D continuum element using iso-parametric co-ordinate system is provided below.

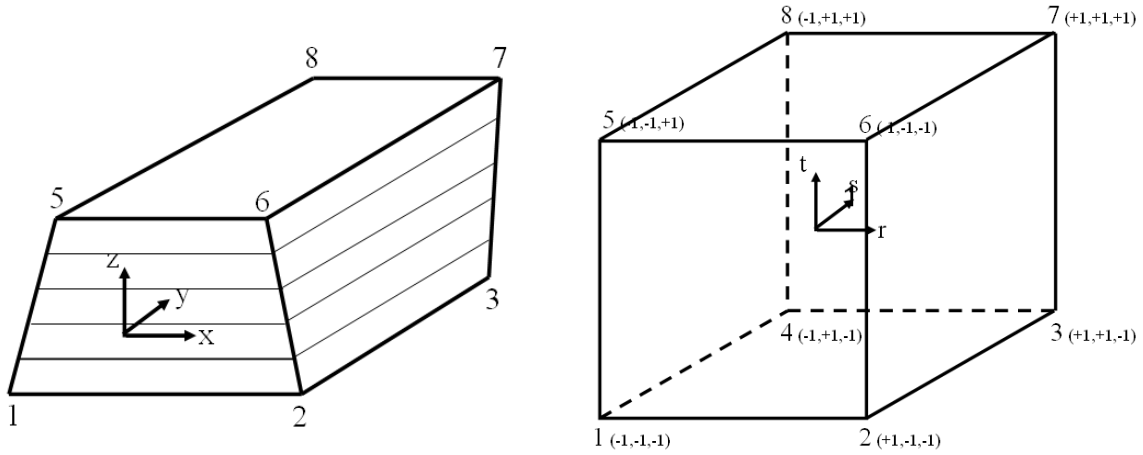

Fig. 4.2 Linear layered composite element and corresponding brick element in iso-parametric co-ordinates

The displacement interpolation functions (shape functions) are similar to those of a homogenous element and for a linear element are given by the following equations:

$$\varphi_1 = \frac{1}{8}(1-r)(1-s)(1-t); \quad \varphi_2 = \frac{1}{8}(1+r)(1-s)(1-t); \quad \varphi_3 = \frac{1}{8}(1+r)(1+s)(1-t); \quad \varphi_4 = \frac{1}{8}(1-r)(1+s)(1-t)$$
$$\varphi_5 = \frac{1}{8}(1-r)(1-s)(1+t); \quad \varphi_6 = \frac{1}{8}(1+r)(1-s)(1+t); \quad \varphi_7 = \frac{1}{8}(1+r)(1+s)(1+t); \quad \varphi_8 = \frac{1}{8}(1-r)(1+s)(1+t) \tag{4.1}$$

For the iso-parametric formulation, the element geometry and nodal field variables (displacements *u, v* and *w* in this case) are interpolated using the same set of interpolation functions. Hence we have

$$x = \sum_{i=1}^{8} \varphi_i(r,s,t)x_i; \quad y = \sum_{i=1}^{8} \varphi_i(r,s,t)y_i; \quad z = \sum_{i=1}^{8} \varphi_i(r,s,t)z_i \tag{4.2}$$

$$u(x,y,z) = \sum_{i=1}^{8} \varphi_i(r,s,t)u_i; \quad v(x,y,z) = \sum_{i=1}^{8} \varphi_i(r,s,t)v_i; \quad w(x,y,z) = \sum_{i=1}^{8} \varphi_i(r,s,t)w_i \tag{4.3}$$

The Jacobian matrix of transformation [***J***] relates the iso-parametric (r-s-t) co-ordinate space of the element to the global (x-y-z) co-ordinates of the element so that:

$$\underset{3\times3}{[\boldsymbol{J}]} = \frac{\partial x_i}{\partial \xi_j} \quad i, j = 1,2,3$$

$$\text{where } x_1 = x, \quad x_2 = y, \quad x_3 = z \qquad (4.4)$$
$$\text{and} \quad \xi_1 = r, \quad \xi_2 = s, \quad \xi_3 = t$$

The various terms of the inverse matrix of the Jacobian, $[\boldsymbol{JI}] \equiv [\boldsymbol{J}]^{-1}$ are rearranged as a (6x9) geometric mapping matrix $\mathbf{[\bar{J}]}$ and used to relate the strain $\{\boldsymbol{\varepsilon}\}$ in x-y-z co-ordinates to the displacement gradient vector $\{\boldsymbol{S_N}\}$ in the r-s-t co-ordinates so that:

$$\underset{6\times1}{\{\boldsymbol{\varepsilon}\}} = \underset{6\times9}{[\bar{\boldsymbol{J}}]} \underset{9\times1}{\{\boldsymbol{S_N}\}} \qquad (4.5)$$

where,

$$\{\boldsymbol{S}^N\}^T = \left\{\partial u/\partial r, \partial u/\partial s, \partial u/\partial t, \partial v/\partial r, \partial v/\partial s, \partial v/\partial t, \partial w/\partial r, \partial w/\partial s, \partial w/\partial t\right\}$$

The stiffness matrix for the layered element is derived based on a small strain formulation and hence the $\{\boldsymbol{\varepsilon}\}$ is as given in eq. (C1) of the Appendix C. The matrices, $[\boldsymbol{J}]$ and $\mathbf{[\bar{J}]}$ are given in eq. (C2) and (C3) of Appendix C. Furthermore, the displacement gradient vector $\{\boldsymbol{S_N}\}$ is related to the nodal displacement vector $\{\boldsymbol{U^N}\}$ through the matrix $[\boldsymbol{P}]$ as given in Eq. (4.6). The matrix $[\boldsymbol{P}]$ is the matrix of partial derivatives of interpolation functions.

$$\underset{9\times1}{\{\boldsymbol{S_N}\}} = \underset{9\times24}{[\boldsymbol{P}]} \underset{24\times1}{\{\boldsymbol{U^N}\}} \qquad (4.6)$$

where, $\{\boldsymbol{U}^N\}^T = \{u_1, v_1, w_1, u_2, v_2, w_2, u_3, v_3, w_3, u_4, v_4, w_4, u_5, v_5, w_5, u_6, v_6, w_6, u_7, v_7, w_7, u_8, v_8, w_8\}$

The $[\boldsymbol{P}]$ matrix is given in eq. (C4) of Appendix C. Combining Eqs. (4.5) and (4.6) we get,

$$\begin{aligned}\underset{6\times1}{\{\varepsilon\}} &= \underset{6\times9}{[\bar{J}]}\,\underset{9\times24}{[P]}\,\underset{24\times1}{\{U^N\}} \\ &= \underset{6\times24}{[B]}\,\underset{24\times1}{\{U^N\}}\end{aligned} \tag{4.7}$$

where **[*B*]** is the strain displacement matrix and is observed to be a 6 x 24 matrix composed of the first partial derivatives of the interpolation functions.

The stiffness matrix $[K_e]$ for a 8-node continuum 3D finite element is derived from the expression of elemental strain energy for a linearized problem as given below:

$$\begin{aligned}U^e &= \frac{1}{2}\int_{V_e} \underset{1\times6}{\{\sigma\}^T}\,\underset{6\times1}{\{\varepsilon\}}\,dV \\ &= \frac{1}{2}\int_{V_e} \underset{1\times6}{\{\varepsilon\}^T}\,\underset{6\times6}{[C]}\,\underset{6\times1}{\{\varepsilon\}}\,dV \\ &= \frac{1}{2}\int_{V_e} \left\{\underset{6\times24}{[B]}\,\underset{24\times1}{\{U^N\}}\right\}^T \underset{6\times6}{[C]}\left\{\underset{6\times24}{[B]}\,\underset{24\times1}{\{U^N\}}\right\}dV \\ &= \frac{1}{2}\underset{1\times24}{\{U^N\}^T}\left[\int_{V_e} \underset{6\times24}{[B]^T}\,\underset{6\times6}{[C]}\,\underset{6\times24}{[B]}\,dV\right]\underset{24\times1}{\{U^N\}} \\ &= \frac{1}{2}\underset{1\times24}{\{U^N\}^T}\,\underset{24\times24}{[K_e]}\,\underset{24\times1}{\{U^N\}}\end{aligned}$$

Finally, the stiffness matrix for the layered composite element is given as:

$$\begin{aligned}\underset{24\times24}{[K^e]} &= \int_V \underset{24\times6}{[B]^T}\,\underset{6\times6}{[C(z)]}\,\underset{6\times24}{[B]}\;dV \\ &= |J|\int_{-1}^{+1}\int_{-1}^{+1}\int_{-1}^{+1}[B]^T[C(t)][B]\,drdsdt\end{aligned} \tag{4.8}$$

The matrix **[*C(z)*]** is a (6 x 6) material stiffness matrix. The **[*C(t)*]** is allowed to vary with each layer of the laminate so that **[*C(t)*]** can be replaced by $[C^{(k)}]$, which

represents the material linear elastic stiffness matrix for the kth layer of the laminate. For the nonlinear viscoelastic material layer, $\mathbf{[}\boldsymbol{C}^{(k)}\mathbf{]}$ is a function of time, temperature, and stress which needs to be updated at every time and for different stress and temperature fields. Thus, this study formulates a consistent tangent stiffness at every time. The consistent tangent stiffness matrices $\mathbf{[}\boldsymbol{C}^{(k)}\mathbf{]}$ are implemented at the material integration points in the composite elements. Due to the nonlinear constitutive relation, Eq. (4.8) is used to obtain the linearized trial (predictor) solutions and iterative (corrector) procedure is added to minimize errors arising from linearization. Detailed discussion on the predictor-corrector procedure is given in section 4.4. This study uses Gaussian quadrature to evaluate the stress and strain fields of the FML, as shown in Fig. 4.1. The through-thickness stress-strains are evaluated using average stress-strain of each layer (at the Gaussian points). The material consistent tangent stiffness of each layer is incorporated into the element stiffness matrix during the numerical integration. The final form of the stiffness matrix is:

$$\left[\boldsymbol{K}^{e}\right] = |\boldsymbol{J}| \sum_{i=1}^{2}\sum_{j=1}^{2}\sum_{k=1}^{n}\left[\boldsymbol{B}(r_i, s_j, t_k)\right]^{T}\left[\boldsymbol{C}^{(k)}\right]\left[\boldsymbol{B}(r_i, s_j, t_k)\right] w_i w_j w_k \tag{4.9}$$

The above equation can be written in index notation as:

$$\mathrm{K_{mn}} = |\mathrm{J}| \sum_{i=1}^{2}\sum_{j=1}^{2}\sum_{k=1}^{n} \mathrm{B_{mp}}(\mathrm{r_i}, s_\mathrm{j}, t_\mathrm{k})\mathrm{C_{pq}^{(k)}}\mathrm{B_{qn}}(\mathrm{r_i}, s_\mathrm{j}, t_\mathrm{k}) w_i w_j w_k \tag{4.10}$$

where m & n vary from 1 to 24 and p & q vary from 1 to 6

If it is desirable to determine for example, the stress discontinuities between the layers in the FML, the Simpson's integration points, which allow determining stress-

strain at the interfaces between layers, can be used. For a Simpson's rule, the range of integration is divided into an even number of intervals. This means that it is required to use an odd number of integration points per layer when Simpson's rule is used. The integration points are equally spaced in each layer. An example of multiple application of Simpson's rule for a two layered laminate with three integration points per layer is illustrated in Fig. 4.3.

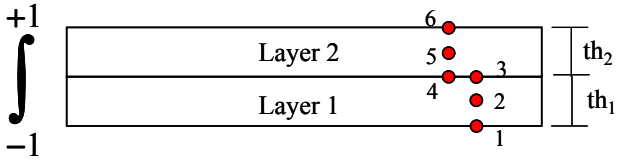

$$Total\ thickness = th = th_1 + th_1 = 2$$

$$Thickness\ ratio\ of\ layer\ 1 = tr_1 = \frac{th_1}{th} = \frac{th_1}{2}$$

$$Thickness\ ratio\ of\ layer\ 2 = tr_2 = \frac{th_2}{th} = \frac{th_2}{2} = 1 - tr_1$$

Fig. 4.3 Application of Simpson's rule for a two layered laminate

The expression for the through thickness integration is given in eq. (4.11) as,

$$K_{mn} = \frac{|J|}{6}\sum_{i=1}^{2}\sum_{j=1}^{2}\left[\begin{array}{l}\left(1+2tr_1\right)C_{pq}^{(1)}\left\{\begin{array}{l}B_{mp}(r_i,s_j,t_1)B_{qn}(r_i,s_j,t_1)+4B_{mp}(r_i,s_j,t_2)B_{qn}(r_i,s_j,t_2)+\\ B_{mp}(r_i,s_j,t_3)B_{qn}(r_i,s_j,t_3)\end{array}\right\}\\ +\left(1-2tr_1\right)C_{pq}^{(2)}\left\{\begin{array}{l}B_{mp}(r_i,s_j,t_4)B_{qn}(r_i,s_j,t_4)+4B_{mp}(r_i,s_j,t_5)B_{qn}(r_i,s_j,t_5)+\\ B_{mp}r_i,s_j,t_6)B_{qn}(r_i,s_j,t_6)\end{array}\right\}\end{array}\right]w_i w_j \qquad (4.11)$$

where the indices m & n vary from 1 to 24 and indices p & q vary from 1 to 6. Note that

$$B_{mp}(r_i,s_j,t_3)B_{qn}(r_i,s_j,t_3) = B_{mp}(r_i,s_j,t_4)B_{qn}(r_i,s_j,t_4)$$

For the analysis of FML, we have used the linear layered composite element and the $[C^{(KFRP)}]$ and $[C^{(metal)}]$ are evaluated at the respective material points of the FRP and

metal layers. In case of one integration point per layer is used, average stress and strain variation across thickness is obtained for each layer, which is sampled at the mid-layer.

The analysis of viscoelastic FML with the layered composite element is verified using available creep data for ARALL-4 laminate reported by Pindera et al. [64]. The ARALL-4 FML laminate has a lay-up of {Al/KFRP/AL/KFRP/AL} where the KFRP has a single orientation of 0°. The aluminum layers are 0.305 mm thick while the KFRP layers are 0.216 mm thick resulting in a total thickness of 1.347 mm. The time-dependent properties of the constituents, the isotropic aluminum and the transversely isotropic 0 KFRP are obtained from Pindera et al. [64]. The KFRP exhibits linear viscoelastic behavior along fiber direction while the aluminum exhibits stress dependent nonlinear viscoelastic behavior. The elastic and linear viscoelastic properties of aluminum and KFRP are given in Tables 4.1 and 4.2, respectively.

Table 4.1 Elastic properties for KFRP, Kevlar, aluminum and epoxy

Material	Modulus (MPa)				Poisson's ratio	
	E_{11}	$E_{22}=E_{33}$	$G_{12}=G_{13}$	G_{23}	$\nu_{12}=\nu_{13}$	ν_{23}
KFRP (Transversely Isotropic)	46700	2980	24000	20000	0.35	0.4
Kevlar-49 (Transversely Isotropic)	99000	2230	4319	4000	0.4	0.4
Aluminum (Isotropic)	69000				0.34	
Epoxy (Isotropic)	4344				0.36	

Table 4.2 Prony parameters for KFRP, aluminum, Kevlar and epoxy

N	λn (1/min)	Prony Coefficients x 10^{-6} (1/MPa)					
		KFRP		Aluminum	Kevlar		Epoxy
		$S_{1111(n)}$	$S_{2222(n)}=S_{3333(n)}$	$S_{(n)}$*	$S_{1111(n)}$	$S_{2222(n)}=S_{3333(n)}$	$S_{(n)}$*
1	1	0.04	40	0.049	0.73	0.07	176
2	10^{-1}	0.6	150	0.054	0.071	0.1	5
3	10^{-2}	0.5	50	0.24	0.31	2.8	29
4	10^{-3}	1.5	240	1	0.03	0.44	25
5	10^{-4}	-	2500	-	0.48	4.2	35
6	10^{-5}	-	-	-	0.38	0.4	6.8

* $S_{(n)} = S_{1111(n)} = S_{2222(n)} = S_{3333(n)}$ and $S_{1212(n)} = S_{1313(n)} = S_{2323(n)} = 2(1+\nu)\, S_{(n)}$ for isotropic material

The nonlinear stress dependent parameters for the aluminum are characterized from the creep test data as discussed in chapter II. The variation of these parameters with the effective stress is given in Eq. (4.12).

$$\begin{aligned} g_0 &= 3.606\times10^{-4}\,\bar{\sigma} + 0.892 \ \text{for}\ \bar{\sigma} \geq 241\text{MPa} \\ g_1 g_2 &= \begin{cases} 8.788\times10^{-2}\, e^{1.17\times10^{-2}\bar{\sigma}} & \text{for } 207 \leq \bar{\sigma} < 310\text{MPa} \\ 6.378\times10^{-4}\, e^{2.766\times10^{-2}\bar{\sigma}} & \text{for } \bar{\sigma} \geq 310\text{MPa} \end{cases} \\ a &= 1.0 \end{aligned} \tag{4.12}$$

The yield stress for aluminum is 331 MPa hence the experimental creep strain data above this stress level (the experimental curve at 345 MPa) can be composed of a plastic/viscoplastic component as well. With only the creep loading curves, it is not possible to correctly segregate the viscoelastic and viscoplastic data for aluminum at the 345 MPa stress level so the nonlinear parameters g_0 and g_2 are calibrated at stress levels of 331 MPa and higher with the assumption of a nonlinear viscoelastic behavior. Such an

assumption is done only for the purpose of verification of the framework. In fact the use of this highly nonlinear data also verifies the robustness of the algorithm for high nonlinearities. For an analysis involving a load removal and strain recovery (e.g. cyclic loading), the use of these values for g_0 and g_2 can give erroneous results. For such an analysis, it is important to consider the viscoplastic behavior of aluminum at stress levels higher than the yield limit.

Fig. 4.4 illustrates creep responses of the ARALL-4 at two stress levels of 276 and 345 MPa. These stresses are applied along the unidirectional fiber direction of the KFRP. The creep responses determined using the layered composite elements are comparable with the ones from the experiments. Effective analytical models based on the CLT are also obtained by [64], which are shown in the Fig. 4.4.

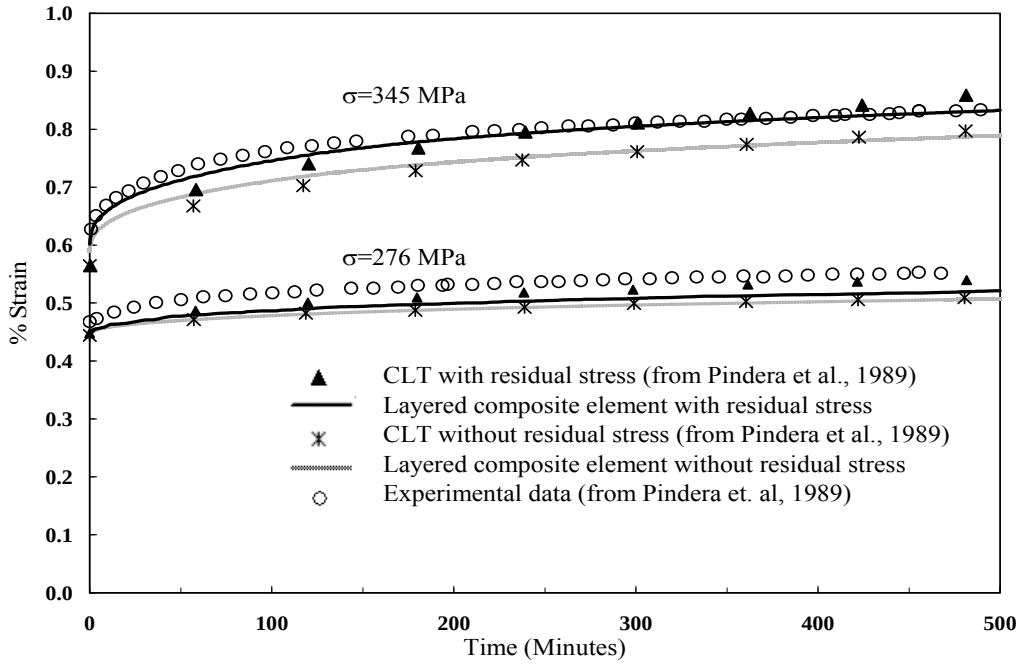

Fig. 4.4 Comparison of creep response with experimental data for ARALL-4 laminate

Significant residual thermal stresses are observed in the ARALL-4 during cool down from the cure temperature of 177°C to the test temperature of 121°C. This is due to the significant difference in the thermal expansion coefficient of the aluminum and KFRP. The analyses with and without residual thermal stresses are carried out and the results are compared with the CLT results (with and without residual stresses) and the experimental results from [64]. For these applied stresses, the stress induced in the aluminum layers is in the nonlinear viscoelastic range. It is observed that the numerical values from the layered composite element having one through thickness integration point per layer match very well with those of the CLT and experimental results. The nonlinear parameters calibrated only up to 345 MPa from the experimental data are extrapolated up to 400 MPa using the linearized tangent from the last point (345 MPa).

4.2.2. Integrated micromodel for the FRP layers in the layered composite element

It is also possible to incorporate a micromodel (for unidirectional composites) discussed in chapter III, for the FRP layers in the layered composite element. The unidirectional fiber is modeled as orthotropic viscoelastic and the matrix constituent follows isotropic viscoelastic solids. The fiber and matrix are modeled with different stress and temperature dependent viscoelastic behaviors. The unit-cell model, consisting of four fiber and matrix subcells, is already discussed in detail in chapter III. The homogenization schemes also include a stress correction algorithm to enhance computational efficiency and accuracy. This approach requires inputing fiber and matrix material properties along with the fiber volume fraction for the FRP layer. The

micromodel provides the effective material constant $[C]^{(k)}$ for each of the k^{th} FRP layer in the FML. Such an approach can be very useful for the design of new FML material configurations. The use of the micromodel also allows calculating detailed nonlinear elastic and time dependent behaviors of the fiber and matrix constituents.

The analyses carried out previously for the ARALL-4 laminates are now performed using the micromechanical model to first obtain effective properties for the FRP layers. The KFRP layers of the ARALL-4 have aramid-epoxy prepregs with a fiber weight fraction of 50%. This translates to a fiber volume fraction of 48.2%. The elastic and time dependent properties for Kevlar fiber and epoxy matrix are given in Tables 4.1 and 4.2. The ARALL-4 for which experimental data is available uses AF 191 epoxy resin but the properties of this resin are not easily available in literature. The properties of epoxy 3501 resin from [87] are used instead. The time dependent properties for the Kevlar are obtained from [84]. The elastic moduli for Kevlar-49 are calibrated based on the elastic response of ARALL-4.

The analysis is again carried out at the stress levels of 276 MPa and 345 MPa without considering residual thermal stresses. The results are compared with the one obtained using the layered composite element with orthotropic properties of the homogenous layers. It is noted that FML are often analyzed using detailed 3D brick element for each lamina (FRP and metal). Thus, to analyze responses of FML with five FRP and metal laminas, at least five 3D continuum elements are generated through the thickness. The advantages of using this method are that a detailed and non-averaged 3D response of each layer can be obtained so that phenomenon such as delamination and

damage can be studied. The other failure modes induced by these phenomenon such as delamination buckling can also be studied. However, it is computationally expensive especially when nonlinear time-dependent constitutive material models are included. In this study, the creep responses of FML obtained using a layered composite element are also compared to the ones from the analysis with detailed 3D elements for each layer. The results are shown in Fig. 4.5.

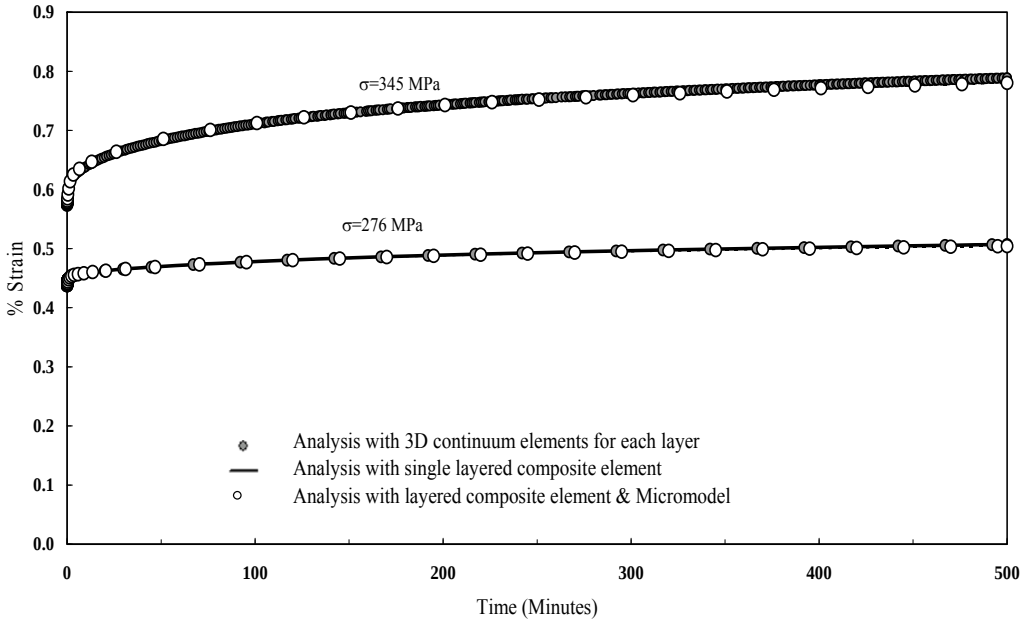

Fig. 4.5 Comparison of creep response for ARALL-4 for layered composite element with and without micromodel with detailed 3D analysis

This comparison verifies the successful incorporation of the micromodel to the layered composite element as well as the accuracy of the use of layered composite element itself. The analysis methods explained are also compared with respect to their

computation costs involved. The CPU time required for the analysis at the stress level of 345 MPa is considered. The comparison is given in Table 4.3.

Table 4.3 Comparison of CPU time for analysis at 345 MPa

Analysis Method	Detailed 3D analysis	Analysis using layered element	Analysis using layered element with micromechanics
CPU Time (seconds)	6.69	3.85	4.39

It is observed that the analysis with layered composite element is the most efficient one and requires 42% less CPU time than that required for a detailed 3D analysis. This data reflects the advantage of using a layered composite element for carrying out large scale FE analysis of practical structural components. If micromechanical model is added to the layered element the time required is still approximately 34% less than that for a detailed 3D analysis without micromechanical model. This is very promising for trying out a component material and structural "design through analysis" with new materials.

4.3 THERMO-VISCOELASTIC ANALYSIS OF FML USING A SUBLAMINATE APPROACH

This section discusses the development of a constitutive sublaminate model to homogenize the nonlinear viscoelastic responses of the FRP and aluminum layers of the FML. The sublaminate model is used to obtain a 3D through-thickness effective

response of the FML. This model can be linked with general element types in displacement-based FE framework and used for the analysis of GLARE® and ARALL® structures.

The sublaminate model, which was proposed by Haj-ali and Muliana [30], is based on the 3D lamination theory assuming a perfect bond between layers. The incremental average stress and strain vectors for the effective continuum, representing the response of the layered medium, are partitioned into *in-plane* (x_1-x_2 axes) and *out-of-plane* (x_3 axis) components:

$$\begin{aligned} d\bar{\sigma}_i &= \left\{ d\bar{\sigma}_{11}, d\bar{\sigma}_{22}, d\bar{\tau}_{12} \right\}, \qquad d\bar{\sigma}_o = \left\{ d\bar{\sigma}_{33}, d\bar{\tau}_{13}, d\bar{\tau}_{23} \right\} \\ d\bar{\varepsilon}_i &= \left\{ d\bar{\varepsilon}_{11}, d\bar{\varepsilon}_{22}, d\bar{\gamma}_{12} \right\}, \qquad d\bar{\varepsilon}_o = \left\{ d\bar{\varepsilon}_{33}, d\bar{\gamma}_{13}, d\bar{\gamma}_{23} \right\} \end{aligned} \tag{4.13}$$

where an over bar indicates a homogenized sublaminate quantity. The subscript "i" and "o" denote an in-plane and out-of-plane stress or strain vectors, respectively. The displacement continuity requires that the in-plane strains to be continuous across the interface, while equilibrium of tractions across the interface requires the out-of-plane stresses to be continuous across the interface. These conditions are satisfied in the global coordinate system, which can be expressed in an incremental form as:

$$d\varepsilon_i^{(k)} = d\bar{\varepsilon}_i \qquad d\sigma_o^{(k)} = d\bar{\sigma}_o \qquad \text{k=Al, KFRP} \tag{4.14}$$

where k is the ply (layer) name, which is aluminum and FRP, and N is the total number of plies in the sublaminate, which is two in this case. The complementary in-plane stress and out-of-plane strain vectors are taken as weighted averages of all layers:

$$d\bar{\sigma}_i = \sum_{k=1}^{N} \frac{t^{(k)}}{t} d\sigma_i^{(k)} \qquad d\bar{\varepsilon}_o = \sum_{k=1}^{N} \frac{t^{(k)}}{t} d\varepsilon_o^{(k)}$$
$$\text{where} \qquad t = \sum_{k=1}^{N} t^{(k)} \tag{4.15}$$

Equations (4.14) and (4.15) define the through-thickness homogenized relations needed for the incremental formulation of the sublaminate model. The time-dependent stress-strain relation for each layer, in the global coordinate system, is combined with the sublaminate homogenized relations to form the sublaminate effective time-dependent properties. The stress-strain relations of the k[th] ply are:

$$\begin{Bmatrix} d\sigma_i \\ d\sigma_o \end{Bmatrix}^{(k)} = \begin{bmatrix} C_{ii} & C_{io} \\ C_{oi} & C_{oo} \end{bmatrix}^{(k)} \begin{Bmatrix} d\varepsilon_i \\ d\varepsilon_o \end{Bmatrix}^{(k)} \tag{4.16}$$

which can be written in a partially inverted form as:

$$\begin{Bmatrix} d\sigma_i \\ d\varepsilon_o \end{Bmatrix}^{(k)} = \begin{bmatrix} A & B \\ -B^T & D \end{bmatrix}^{(k)} \begin{Bmatrix} d\varepsilon_i \\ d\sigma_o \end{Bmatrix}^{(k)}$$
$$\text{where:} \quad D = C_{oo}^{-1}$$
$$B = C_{io} C_{oo}^{-1} \tag{4.17}$$
$$A = C_{ii} - C_{io} C_{oo}^{-1} C_{oi}$$

Substituting Eq. (4.17) into Eqs. (4.14) and (4.15) gives the overall incremental sublaminate stress-strain vector as functions of the ply's material constitutive model:

$$\begin{Bmatrix} d\bar{\sigma}_i \\ d\bar{\varepsilon}_o \end{Bmatrix} = \sum_{k=1}^{N} \frac{t^{(k)}}{t} \begin{bmatrix} A & B \\ -B^T & D \end{bmatrix}^{(k)} \begin{Bmatrix} d\bar{\varepsilon}_i \\ d\bar{\sigma}_o \end{Bmatrix} \tag{4.18}$$

Equation (4.18) can be written as:

$$\begin{Bmatrix} d\bar{\sigma}_i \\ d\bar{\varepsilon}_o \end{Bmatrix} = \begin{bmatrix} \bar{A} & \bar{B} \\ -\bar{B}^T & \bar{D} \end{bmatrix} \begin{Bmatrix} d\bar{\varepsilon}_i \\ d\bar{\sigma}_o \end{Bmatrix} \tag{4.19}$$

Finally, the effective tangent stiffness matrix $\left[\bar{C}\right]$ for the sublaminate is obtained from Eq. (4.19) as:

$$\begin{Bmatrix} d\bar{\sigma}_i \\ d\bar{\sigma}_o \end{Bmatrix} = \left[\bar{C}\right] \begin{Bmatrix} d\bar{\varepsilon}_i \\ d\bar{\varepsilon}_o \end{Bmatrix} = \begin{bmatrix} \bar{C}_{ii} & \bar{C}_{io} \\ \bar{C}_{oi} & \bar{C}_{oo} \end{bmatrix} \begin{Bmatrix} d\bar{\varepsilon}_i \\ d\bar{\varepsilon}_o \end{Bmatrix}$$

$$\text{where:} \quad \begin{aligned} \bar{C}_{oo} &= \bar{D}^{-1} \\ \bar{C}_{io} &= \bar{B}\bar{D}^{-1} \\ \bar{C}_{oi} &= \bar{C}_{io}^{T} \\ C_{ii} &= \bar{A} + \bar{B}\bar{D}^{-1}\bar{B}^{T} \end{aligned} \tag{4.20}$$

In this study, a two-layer sublaminate model is developed with the first layer as an isotropic metal layer and the second layer as orthotropic unidirectional FRP layer. Hence it can be used to model a FML with single type of metal layers (current available FML have only one type of metal) and a single type (with single fiber angle) of FRP layers. Such a lay-up exists for GLARE-1 (0/0 Glass-FRP lay-up), GLARE-2 (0/0 or 90/90 Glass-FRP lay-up) and all ARALL® laminates. It is also possible to use the sublaminate model to homogenize responses of more than two ply layers as previously studied in [31]. The strain components in this representative stacking sequence is grouped into two parts based on the in-plane and out-of plane components:

$$\begin{aligned} d\varepsilon_o^T &= \left\{ d\varepsilon_{33}^{(1)}, d\gamma_{13}^{(1)}, d\gamma_{23}^{(1)}, d\varepsilon_{33}^{(2)}, d\gamma_{13}^{(2)}, d\gamma_{23}^{(2)} \right\} \\ d\varepsilon_i^T &= \left\{ d\varepsilon_{11}^{(1)}, d\varepsilon_{22}^{(1)}, d\gamma_{12}^{(1)}, d\varepsilon_{11}^{(2)}, d\varepsilon_{22}^{(2)}, d\gamma_{12}^{(2)} \right\} \end{aligned} \tag{4.21}$$

Equations (4.14) to (4.20) are satisfied when the constitutive relations for the layers 1 and 2 are linear elastic. An iterative correction scheme is performed in order to correct for errors due to linearized sublaminate relations. Each layer of the laminate experiences different nonlinear behaviors so imposing the sublminate relations leads to a nonzero residual strain and stress, which are defined by:

$$\begin{Bmatrix} dR_{\varepsilon} \\ dR_{\sigma} \end{Bmatrix}_{6\times 1} = \begin{Bmatrix} t_1 d\varepsilon_{33}^{(1)} + t_2 d\varepsilon_{33}^{(2)} - t d\bar{\varepsilon}_{33} \\ t_1 d\gamma_{13}^{(1)} + t_2 d\gamma_{13}^{(2)} - t d\bar{\gamma}_{13} \\ t_1 d\gamma_{23}^{(1)} + t_2 d\gamma_{23}^{(2)} - t d\bar{\gamma}_{23} \\ d\sigma_{33}^{(1)} - d\sigma_{33}^{(2)} \\ d\tau_{13}^{(1)} - d\tau_{13}^{(2)} \\ d\tau_{23}^{(1)} - d\tau_{23}^{(2)} \end{Bmatrix} = \begin{Bmatrix} \sum_{k=1}^{2} t_k d\varepsilon_o^{(1)} - t d\bar{\varepsilon}_o \\ C_{oi}^{(1)} d\varepsilon_i^{(1)} + C_{oo}^{(1)} d\varepsilon_o^{(1)} - C_{oi}^{(2)} d\varepsilon_i^{(2)} - C_{oi}^{(2)} d\varepsilon_o^{(2)} \end{Bmatrix} = 0 \tag{4.22}$$

where dR_{ε} is the residual from the strain relation in Eq. (4.15) and dR_{σ} is the residual form of the stress relations in Eq. (4.14) expressed incrementally in terms of the strains in the subcells. The stress and strain components at each layers (unknown variables) are determined by solving $dR_{\sigma} = 0$ and $dR_{\varepsilon} = 0$.

An iterative corrector scheme is formulated at every incremental time step to satisfy both the sublaminate constraints and the nonlinear viscoelastic constitutive equations. To minimize the 6 components of the residual vector, the stress-strain components of each layer need to be corrected, which involves a total of 24 stress and strain scalar variables in the two layers. These scalar variables are related via constitutive relations and sublaminate constraints leading to only 6 independent variables. In this study, the out of plane components of strains in each layer $\varepsilon_o^{(k)}$ are chosen as independent variables. The stress correction algorithm for the sublaminate model is schematically shown in Fig. 4.6. A converged solution is achieved when the residual vectors $\boldsymbol{R}_{\boldsymbol{\varepsilon}}^{\boldsymbol{t}}$ and $\boldsymbol{R}_{\boldsymbol{\sigma}}^{\boldsymbol{t}}$ defined in Eq. (4.22) are diminished. Once convergence is achieved the current incremental stresses

and consistent tangent stiffness matrix are updated. To perform structural analyses using the FE framework, these variables are sampled at each material point and sent to the upper FE structural level.

4. Input variables: (at the mth global iteration)

$\bar{\varepsilon}^{t-\Delta t}, \Delta\bar{\varepsilon}^{t,(m)}, \Delta \mathbf{t}^{(m)}, \Delta \mathbf{T}^{t,(m)}$ History: $\bar{\sigma}^{t-\Delta t}, \mathbf{T}^{t-\Delta t}, \mathbf{Hist}^{t-\Delta t}$

5. Initialize linearized state:

$$\mathbf{C}^{(k),t,tr} = \mathbf{C}^{(k),t-\Delta t}(\mathbf{Hist}^{t-\Delta t}) \qquad \mathbf{k=Al,FRP}$$

$$\Delta\varepsilon^{(k),t,(0)} = \Delta\varepsilon^{(k),t,tr} = (\mathbf{C}^{(k),t,tr}, \bar{\mathbf{C}}^{t,tr})\Delta\bar{\varepsilon}^{t}$$

6. Iterate for n=1,2,3 …. (n =Sublaminate iteration counter)

4.1 Evaluate stresses at all layers to get $\sigma_{ij}^{(k),t,(n+1)}$ and $\mathbf{C}^{(k),t,(n)}$

4.2 Compute stress correction:

$$\delta\Delta\varepsilon_{o}^{(k),t,(n+1)} = \delta\Delta\varepsilon_{o}^{(k),t,(n)} + \left[\frac{\partial \mathbf{R}^{t,(n)}}{\partial\Delta\varepsilon_{o}^{(k)}}\right]^{-1} \mathbf{R}^{t,(n)}$$

$$\Delta\varepsilon^{(k),t,(n+1)} = \Delta\varepsilon^{(k),t,(n)} + \delta\Delta\varepsilon^{(k),t,(n+1)}$$

4.3 Evaluate residual vector $\mathbf{R}^{t,(n)} = (\mathbf{R}_{\varepsilon}, \mathbf{R}_{\sigma})$

IF $\left\|\mathbf{R}^{t,(k+1)}\right\| \le \mathbf{Tol}$ THEN GOTO 4 and EXIT

ELSE GOTO 3

7. Update effective stress, consistent tangent stiffness, and history variables:

$$\bar{\sigma}^{t,m} \leftarrow \bar{\sigma}^{t,(n+1)} \quad \bar{\mathbf{C}}^{t,m} \leftarrow \bar{\mathbf{C}}^{t,(n+1)} \quad \mathbf{Hist}^{t,m} \leftarrow \mathbf{Hist}^{t,(n+1)}$$

Fig. 4.6 Stress correction algorithm for sublaminate model

With the sublaminate model, the micromodel of the unidirectional fiber is again used to obtain the effective properties for the FRP layers, while the isotropic constitutive

relation is used for the aluminum layer. The creep responses from the sublaminate approach are compared with the ones of the detailed 3D analysis for two stress levels of 276MPa and 345 MPa. The analyses are done with elastic properties and also the viscoelastic properties for the Kevlar fiber. Fig. 4.7 shows the creep responses generated using the sublaminate model.

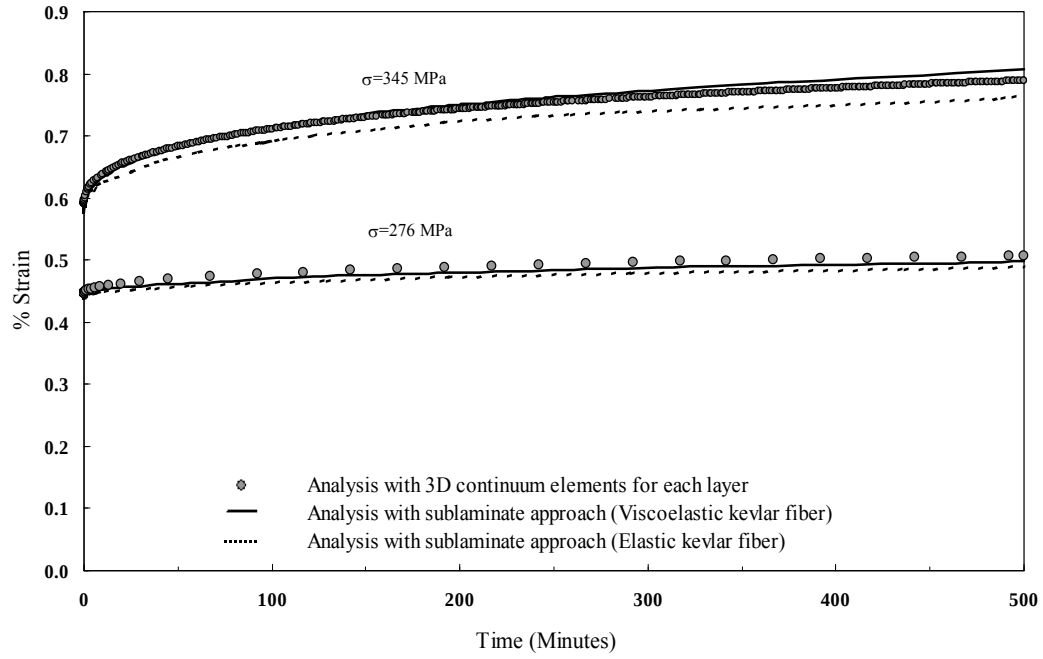

Fig. 4.7 Comparison of creep response for ARALL-4 using sublaminate approach (with micromodel) with detailed 3D analysis

It is observed that using only elastic properties for the Kevlar fibers results in a slight under-prediction of the overall creep response. In this particular case, the effect is not significant since the response is dominated by the creep behavior of the aluminum layers.

4.4 ITERATIVE CORRECTION SCHEMES WITHIN THE NONLINEAR MULTI-SCALE FRAMEWORK

Iterative correction schemes are required at every level of a hierarchical and concurrent nonlinear multi-scale framework. Linearized micromechanical and sublaminate relations will give exact solutions when the constitutive material models for all subcells and layers respectively are linear elastic. In this study, the fiber and matrix subcells and metal layers experience different nonlinear and time-dependent behaviors and hence additional stress correction algorithms are required to obtain accurate nonlinear responses for each sublaminate homogenization, micromechanical homogenization and nonlinear constitutive models for the constituents, i.e., fiber, matrix and metal layer. The stress correction algorithm consists of a predictor step, which is based on the linearized stress-strain state (trial state), and a corrector step, which corrects the trial stress-strain states. The correction algorithms for the multi-scale material models need to be performed in each material (Gaussian) point at every incremental time step within FE structural analyses. At the FE structural level, linearized prediction and iterative correction schemes are also performed. The stress correction for the micromechanical homogenization and for the nonlinear viscoelastic model of individual constituents has already been discussed in chapter III and II, respectively. The stress correction for the sublaminate model has been discussed in section 4.3. Fig. 4.8 shows nested stress-correction algorithm from the constituent level to the effective responses of the FML (macro level). The algorithm is designed to be suitable for displacement based FE formulations.

The algorithm for the current time increment is explained below:

1. Input for the algorithm:

   A trial effective incremental strain tensor $\Delta\bar{\boldsymbol{\varepsilon}}^{t}$ at current time t, an effective stress $\bar{\boldsymbol{\sigma}}^{t-\Delta t}$, strain $\bar{\boldsymbol{\varepsilon}}^{t-\Delta t}$, history variables $\boldsymbol{Hist}^{t-\Delta t}$ from the previous converged time step and the temperature at current time $\boldsymbol{T}^{t}$ as used as inputs. These input quantities are sampled at the Gaussian points (link between material and the element). The trial effective incremental strains are obtained from the FE structural scale using the consistent tangent stiffness of the FML at the previous converged time step ($t - \Delta t$).

2. Analysis Procedure:

   The trial lamina level incremental strains and stress are calculated from the sublaminate relations given in Eq. (4.14) and Eq. (4.15). The nonlinearities in each lamina results in a stress and strain residual given by Eq. (4.22). The stress correction is carried out using Newton-Raphson iterative scheme shown in Fig. 4.7. During the sublaminate calculations, the strains in each lamina are used as an input for the lower scale, i.e. for the micromechanical model of the FRP layer and the nonlinear viscoelastic model of the metal layer. The strain concentration matrix is used to relate the lamina strains to the strains in each subcell. Again the nonlinearities in the fiber and matrix cells result in a stress and strain residual and a stress correction is performed to diminish the residual.

The constituent level calculations for the nonlinear viscoelastic model are carried out in the metal layer, one fiber cell and three matrix cells of micromodel. The linearized prediction is obtained using the input incremental strains and stress correction as explained in chapter II is performed. The convergence is achieved once the residuals at the constituent, micromechanical, and sublaminate levels are minimized.

3. Output of the algorithm:

   Once convergence is achieved, the effective stress $\bar{\sigma}^t$ and the effective consistent tangent stiffness $\bar{\boldsymbol{C}}^t$ at each Gaussian point are calculated and sent back to the FE level. The history variables $\boldsymbol{Hist}^t$ are updated after convergence is achieved.

The effect of the stress correction schemes in the nonlinear framework on the accuracy of the overall nonlinear viscoelastic response is assessed. First the effect of the stress correction at the micromechanical level is studied. For this purpose, analysis is carried out for Kevlar-49/Epoxy AF191 composites. The stress and temperature dependent nonlinearity of matrix is considered.

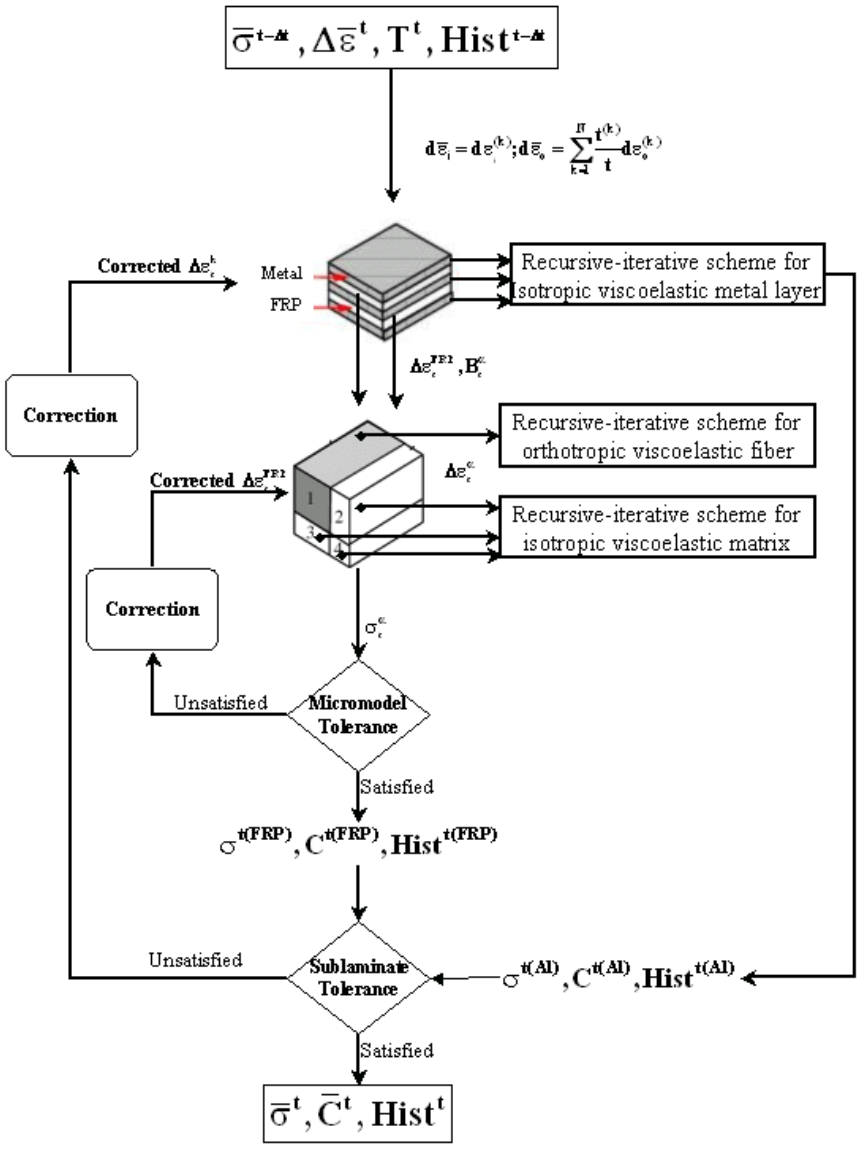

Fig. 4.8 Nested stress correction algorithm for multiple scales in the analysis framework

The elastic and Prony parameters for the constituents are given in Tables 3.2 and 3.4, respectively. The nonlinear stress and temperature dependent parameters for epoxy are given in Eq. (2.38). The fiber is assumed to be linear viscoelastic and hence the constitutive modeling of fiber will not require any stress correction. The stress

corrections are needed in the matrix constitutive model and in the micromechanical homogenization during the time dependent analyses. The analysis is carried out at two different stress and temperature levels for a fiber volume fraction of 20%. A creep loading is applied in the transverse fiber direction and the transverse fiber strains are reported in Fig. 4.9. Fig. 4.9 (a) shows response at fixed temperature and two stress levels, while Fig. 4.9 (b) presents response at two temperatures.

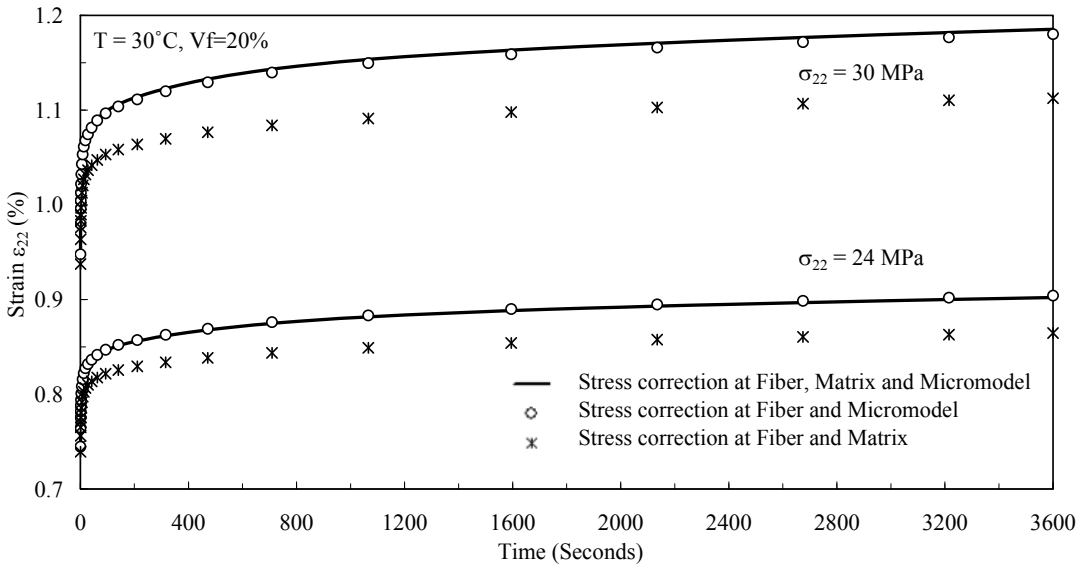

Fig. 4.9 Effect of stress corrections for FRP system (Vf=20%) with nonlinear stress-temperature dependent matrix

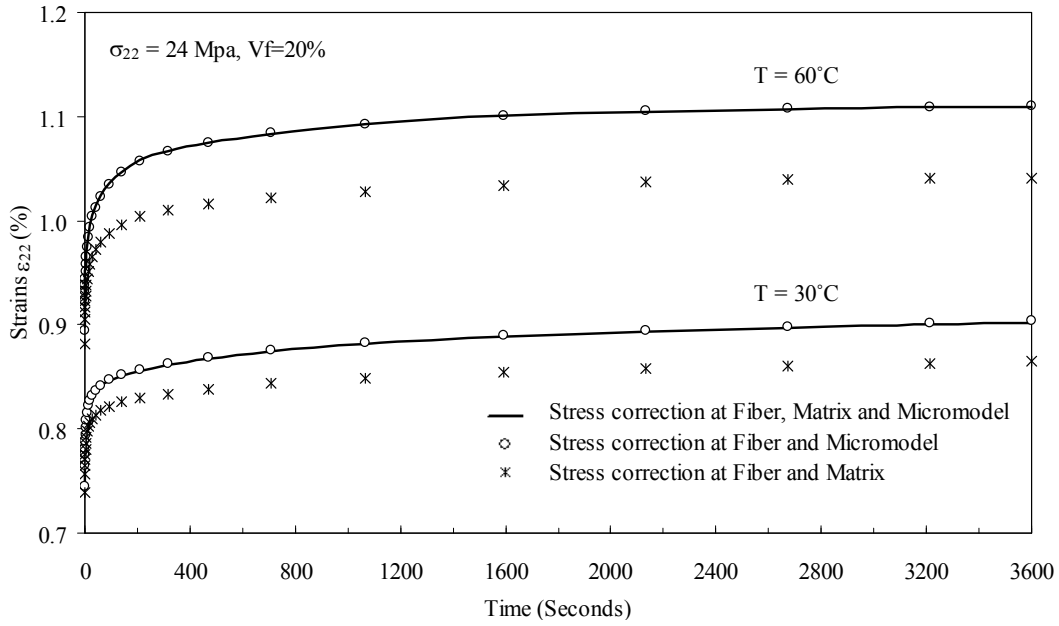

Fig. 4.9 (Continued)

It is observed that the stress correction at the micromechanical level affects the accuracy of the results significantly. Furthermore, in absence of the micromodel correction, the deviation of the response increases with increasing stresses and temperatures, i.e., the increasing stress and temperature dependent nonlinearity.

In the next analysis, the Kevlar-49 fiber is assumed to be stress-dependent nonlinear viscoelastic. The nonlinear stress dependent parameters are already given in Eq. (3.27) in chapter III. A fiber volume fraction of 40% is considered and three different creep loadings are applied along the fiber direction. The effect of stress correction in this case is shown in Fig. 4.10. In this case, it is observed that stress correction in the fiber affects the accuracy of the results. The strains also deviate significantly from the correct values with increasing stress dependent nonlinearity. The

response is governed by the stiff fibers and hence relatively negligible stress is induced in the matrix. Hence the iterations at the matrix and the micromodel are not significant.

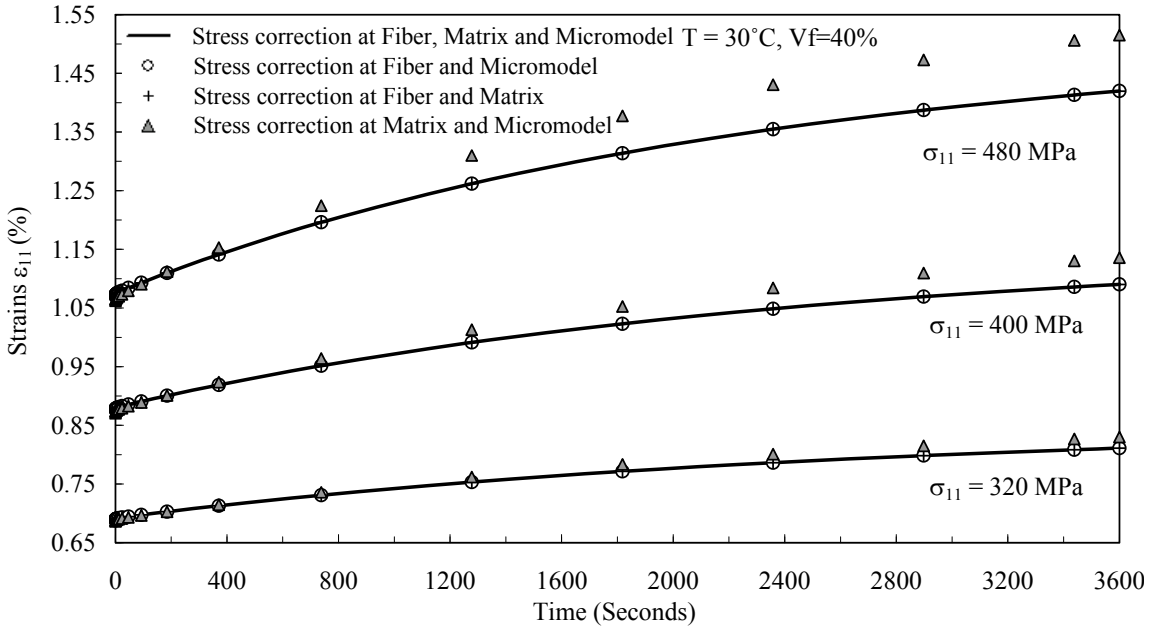

Fig. 4.10 Effect of stress corrections for FRP system (Vf=40%) with nonlinear stress-dependent fiber and nonlinear stress-temperature dependent matrix

In the next analysis, the effect of stress corrections in an integrated micromechanical-sublaminate algorithm with nonlinear constituents is assessed. For this purpose, the ARALL-4 FML is considered. The stress correction is required for the nonlinear aluminum layer and for micromechanical and sublaminate homogenizations. The micromechanical model homogenizes the linear viscoelastic fiber and linear viscoelastic matrix while the sublaminate model homogenizes the linear viscoelastic FRP and the nonlinear viscoelastic aluminum. The fiber and matrix are linear viscoelastic and hence there are no iterations for stress correction at these constituents.

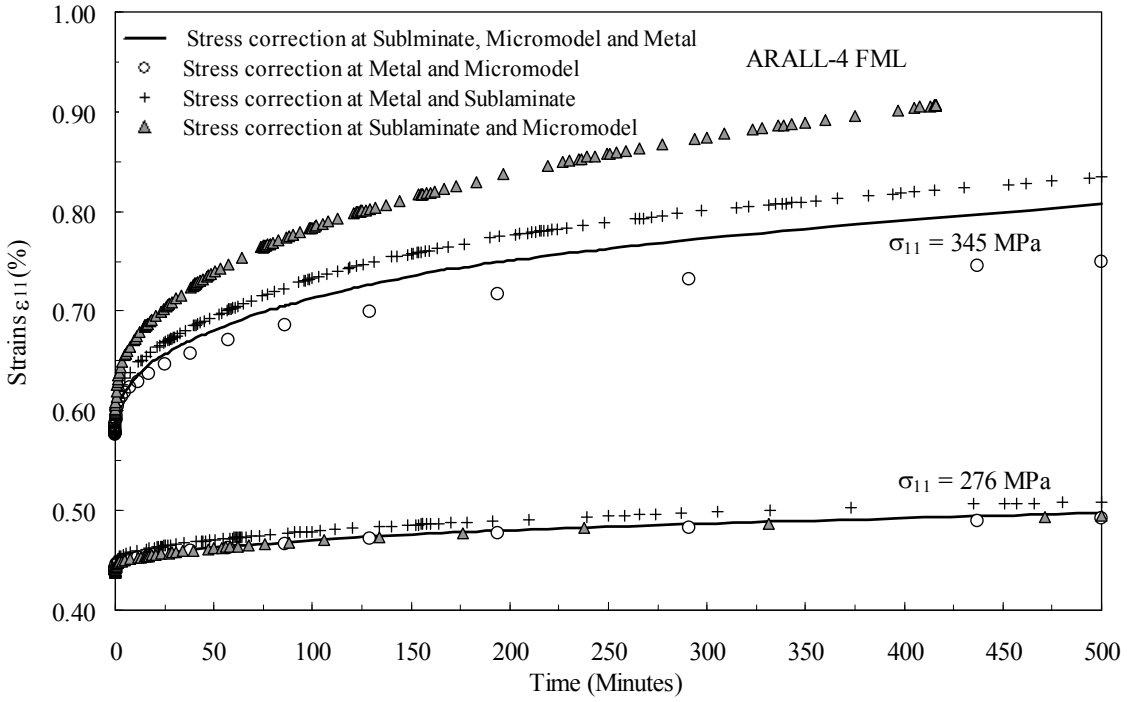

Fig. 4.11 Effect of stress corrections for sublaminate analysis of ARALL-4 FML with nonlinear stress-dependent viscoelastic metal layer and linear viscoelastic KFRP layer

The effect of stress correction is monitored at two stress levels of 276 MPa and 345 MPa as illustrated in Fig. 4.11. The solid line indicates the correct responses, which have been verified with experimental data (Fig. 4.4). At stress level of 276 MPa, the iterations at the metal level and the sublaminate level do not have a significant effect on the accuracy of the effective strains. This is due to presence of mild nonlinearity in the metal layers at this stress level. At the higher stress level (345 MPa), the aluminum layer exhibits significant nonlinearity and hence the stress correction at the metal level and the sublaminate level have a significant effect on the accuracy of the response. The stress corrections also affect the convergence at the structural level. This is visible from an abruptly terminated divergent solution (at 345 MPa) at the structural level when the

stress correction at the metal level is not performed. For both the stress levels, the micromechanics level stress correction also has a significant effect on the accuracy of the response. Thus at higher stress levels, the accuracy is affected by stress iterations at all levels. This prompts us to monitor the residual at the multiple levels at the stress level of 345 MPa as shown in Fig. 4.12.

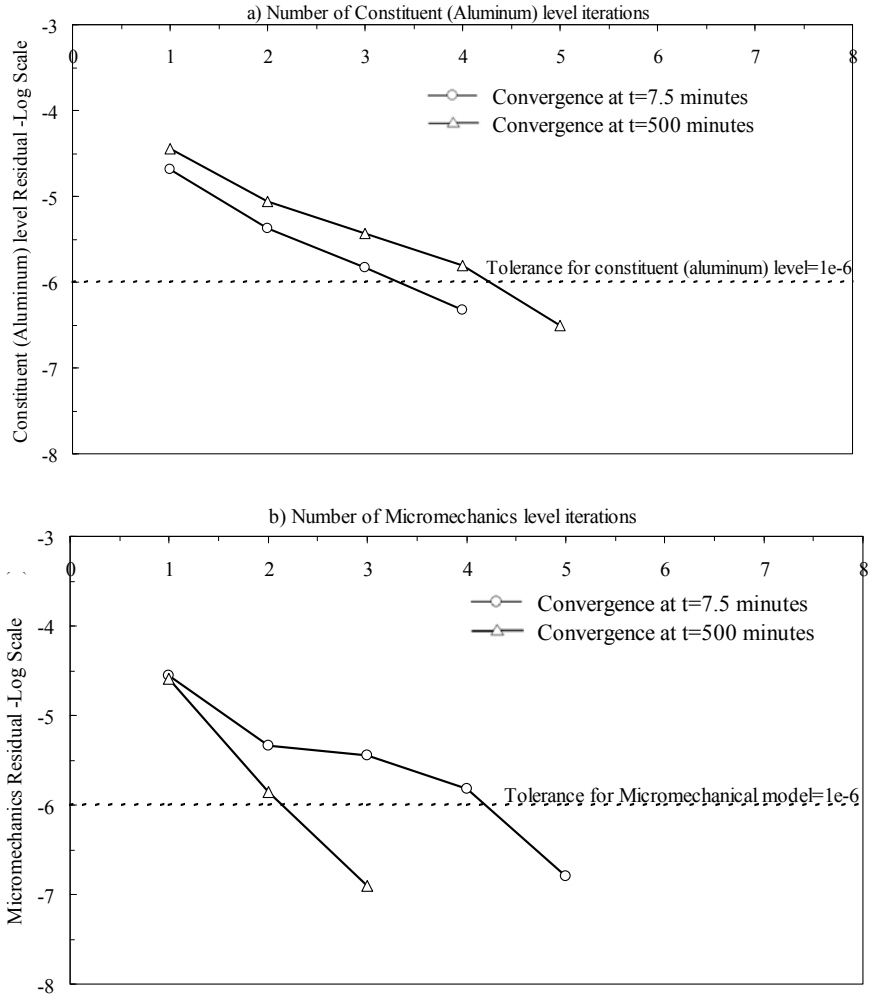

Fig 4.12 Monitoring of multiple scale iterations for ARALL-4 at stress level of 345 MPa

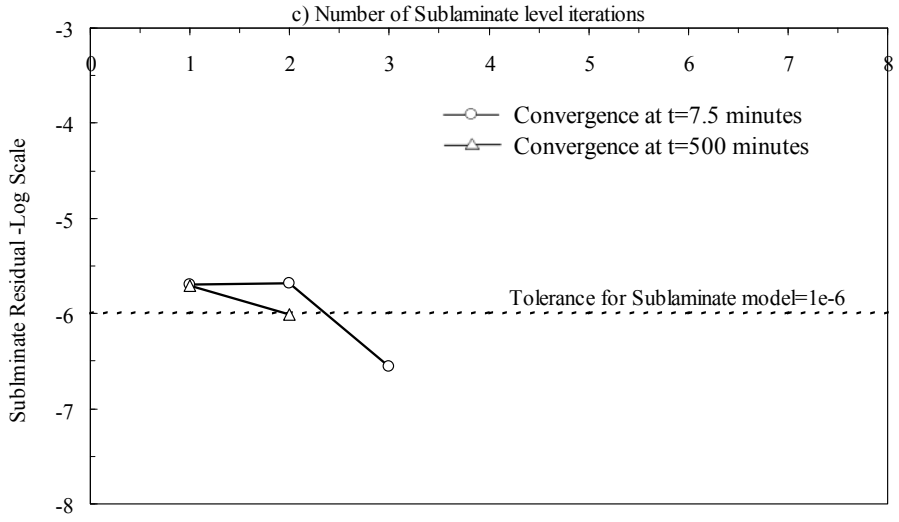

Fig 4.12 (Continued)

The iterations are monitored at two times of 7.5 minutes and 500 minutes. The residual at various levels follows a monotonic convergence as shown in Fig. 4.12. More iteration is needed at the metal level as compared to the micromechanics level and sublaminate level. This is confirmed by observing the number of iterations at other times (not reported here) as well. By observing Fig. 4.11 and 4.12, it can also be concluded that the accuracy of the solution is most affected by the stress correction level where there are the most number of iterations (constituent metal level in this case). The constituent level and homogenization tolerance level is chosen as 10^{-6}. The tolerance represents the allowable error in the strain responses and hence 10^{-6} ($1\mu\varepsilon$) is a suitable choice for the tolerances. The verification of responses in the previous sections and monitoring of iterations in the above figure indicate that a finer tolerance (for e.g. 10^{-7}) would require more number of iterations without significant gain in the accuracy of the results.

This completes the development and verification of the multi-scale framework to analyze nonlinear thermo-viscoelastic behaviors of FML. Micromechanical homogenization and sublaminate homogenization have been successfully incorporated into the framework. The framework can be easily applied to thermo-viscoelastic analysis of existing practical load bearing FML structures. This is discussed in the next chapter.

CHAPTER V

ANALYSIS OF FML STRUCTURAL COMPONENTS: A MULTISCALE APPROACH

This chapter presents an application of the multi-scale framework for predicting effective nonlinear time dependent responses of structural components made of FML. FML have currently been employed in aircraft components, such as fuselage and wing skins. The applications of GLARE® and ARALL® FML have been discussed in chapter I. GLARE® FML are predominantly applied to fuselage skins, while the ARALL® FML are used for the wing skins. GLARE® has been currently applied for fuselage skins of subsonic commercial aircrafts, in which the fuselage skin is not subjected to severe temperature changes. The design of the skin in this case is primarily based on the fatigue strength of the material. Although it is necessary to incorporate ageing (physical and chemical) effects, which can occur over the lifetime of the structure, in designing aircraft structures, current understanding of time-dependent responses of FML is still limited. Furthermore, current and future generations of aircrafts are expected to travel at high speeds, i.e., supersonic or/and hypersonic vehicles, in which the fuselage skin is subjected to extreme temperatures (due to aerodynamic heating), accompanied by complex mechanical loadings. The time dependent (viscoelastic, ageing) effects for GLARE® constituents, aluminum and polymers are more pronounced at high temperature. So in addition to fatigue and other high temperature effects (such as residual thermal stresses), it is necessary to consider the nonlinear time dependent

responses. In this chapter, the time dependent responses i.e., viscoelastic effects for a typical fuselage skin section at high temperatures are monitored. The suitability of GLARE® for this application at these high temperatures is assessed.

5.1 ANALYSIS APPROACH

The multi-scale framework for analyzing responses of FML has been discussed in chapter IV. The approach provides various alternatives, such as use of layered element, use of sublaminate approach, and an integrated micromodel approach. The choice of approach is dependent on the availability of material data of the constituents as well as the lay-up considered. An attempt has been made to utilize the framework in the most efficient way. The comparison of computational efficiency in Table 4.3 indicates that the use of a layered composite element with homogenous anisotropic properties of each layer is the most efficient approach in the framework. This approach requires the knowledge of elastic and time dependent properties of each unidirectional FRP and isotropic metal layer through material testing. In absence of properties of individual layers, experimental data of effective properties of FML can be used within the continuum elements. Although this approach is simple in terms of analyses, no information can be obtained on the behaviors of each constituent during loadings. It is also possible to use the micromechanics approach in conjunction with the layered composite element. This approach requires the knowledge of elastic and time dependent properties of the fiber and matrix, the microstructural arrangements, and the fiber volume fraction in the FRP layer. The advantage of the last approach is that it is capable

of monitoring nonlinear responses and possible damage detection of the lowest constituents (fiber, polymer matrix and metal), i.e., it recognizes microstructural change at various external stimuli, which is suitable for material and structural designs.

This study considers an analysis of GLARE® FML. Standard available GLARE® laminates use S-Glass continuous fiber, FM94 epoxy matrix and a 59% fiber volume fraction for the GFRP layers. Literature survey for the material data does not provide the bulk time dependent properties for such a GFRP. The micromechanical model along with the layered composite element or sublaminate model can be used for the analysis of a GLARE® component. Literature on S-Glass fiber indicates a linear elastic behavior even at moderate temperatures hence it is assumed to be linear elastic. Pindera et al. [64] have characterized the longitudinal and transverse time dependent behavior of KFRP in ARALL®. The data indicates a linear viscoelastic behavior for KFRP even at 121°C. This observation is sufficient to conclude a linear viscoelastic behavior of the structural epoxy matrix used in the FRP layers of FML due to a relatively low stress carried by the matrix as compared to the fibers and the metal layers. Hence a linear viscoelastic behavior can be assumed for the epoxy 3501 matrix in GFRP. The analyses are conducted as follows:

1. The homogenized linear viscoelastic response of GFRP layers is obtained by a separate micromechanical analysis of a single unit cell of unidirectional fiber reinforced composite. The homogenous orthotropic properties (elastic moduli and Prony parameters) are characterized using these responses.

2. These homogenous properties are then provided as input to the layered composite element and the use of micromechanics at each Gaussian point of the FE model is avoided.

It must be noted that the above approach of a stand-alone micromechanical homogenization is possible only due to the linear elastic/viscoelastic behavior of both the constituents (which means the law of linear scaling holds true). For a nonlinear fiber or matrix constituent the micromechanical model must be used concurrently. The elastic properties of S-Glass for the micromechanical analysis are given in Table 5.1. The properties of Epoxy 3501 can be referred to Tables 4.1 and 4.2 in the previous chapter.

Table 5.1 Elastic properties for S-Glass fiber

Material	Modulus (MPa)	Poisson's ratio
	E	ν
S-Glass (Isotropic)	88000	0.2

The strain-time responses in the principle direction of the FRP layers are given in Fig. 5.1. The Prony parameters are characterized using these responses and are given in Table 5.2.

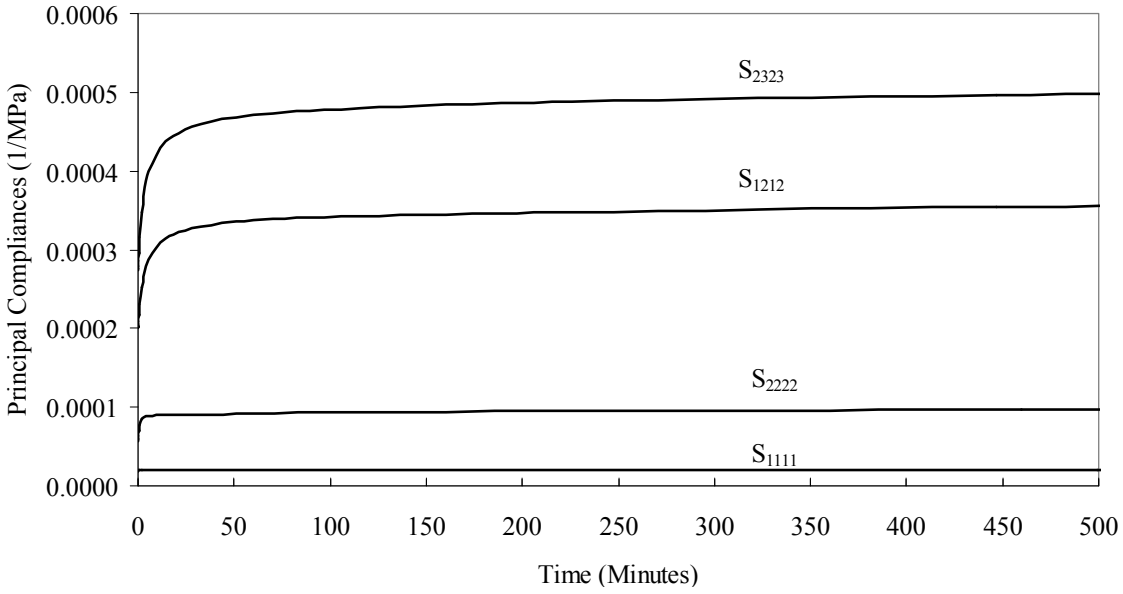

Fig. 5.1 Principal compliances for GFRP (59%) obtained from micromechanics approach

Table 5.2 Characterized Prony parameters for GFRP (59%)

N	λn (1/s)	Dn x 10^{-6} (1/MPa)			
		S_{1111}	S_{2222}	S_{1212}	S_{2323}
1	1	0.295	32.5	70	90
2	10^{-1}	0.002	1.4	52	90
3	10^{-2}	0.023	3.5	25	31
4	10^{-3}	0.01	6	21	32
5	10^{-4}	0.1	9	-	-

5.2 FUSELAGE SKIN LAY-UP AND FINITE ELEMENT MODELING

The standard GLARE® laminates have each GFRP layer as a prepreg with unidirectional fibers and a layer thickness of 0.127 mm. The standard FML laminate coding system will be used to refer the FML lay-ups in this chapter and hence is provided below. It provides information about the number of layers, fiber orientation in FRP layers and thickness of aluminum layers. For example, GLARE® 4A-4/3-0.4 indicates

i. Fiber orientation according to GLARE® 4A definition (as given in Table 1.1), which is a 0/90/0 lay-up for each GFRP.
ii. 4 layers of aluminum and 3 layers of GFRP
iii. A thickness of 0.4 mm for each aluminum layer

The adhesive used in between the GLARE® panel and doublers is same as that used for the matrix of the GFRP layers. As mentioned previously, the adhesive is assumed to behave as a linear viscoelastic material. Hence the properties of structural epoxy 3501 given in Table 4.1 and 4.2 are used for the adhesive. The properties for aluminum at 121°C are also given in Table 4.1, 4.2 and Eq. (4.26).

A typical fuselage has a frame layout with stringers in the longitudinal and hoop direction. The fuselage skin is bonded and riveted over the frame. This construction results in a primary in plane loading (can be normal and shear) in the fuselage skin while the bulk of the bending and out of plane shear loads are taken by the reinforcing stringers. Furthermore, the fuselage skin is also subjected to internal pressure loads. The geometry of the fuselage skin from the entire fuselage considered for this analysis is

shown in Fig. 5.2. The geometry represents the top portion of the fuselage. The fuselage panels are joined together using splices. This splice concept used for joining the FML sheets was introduced in chapter I. The splice connection is one of the critical areas during design and is incorporated into the analysis. The splice configuration used for this analysis and its FE modeling using layered element is also shown.

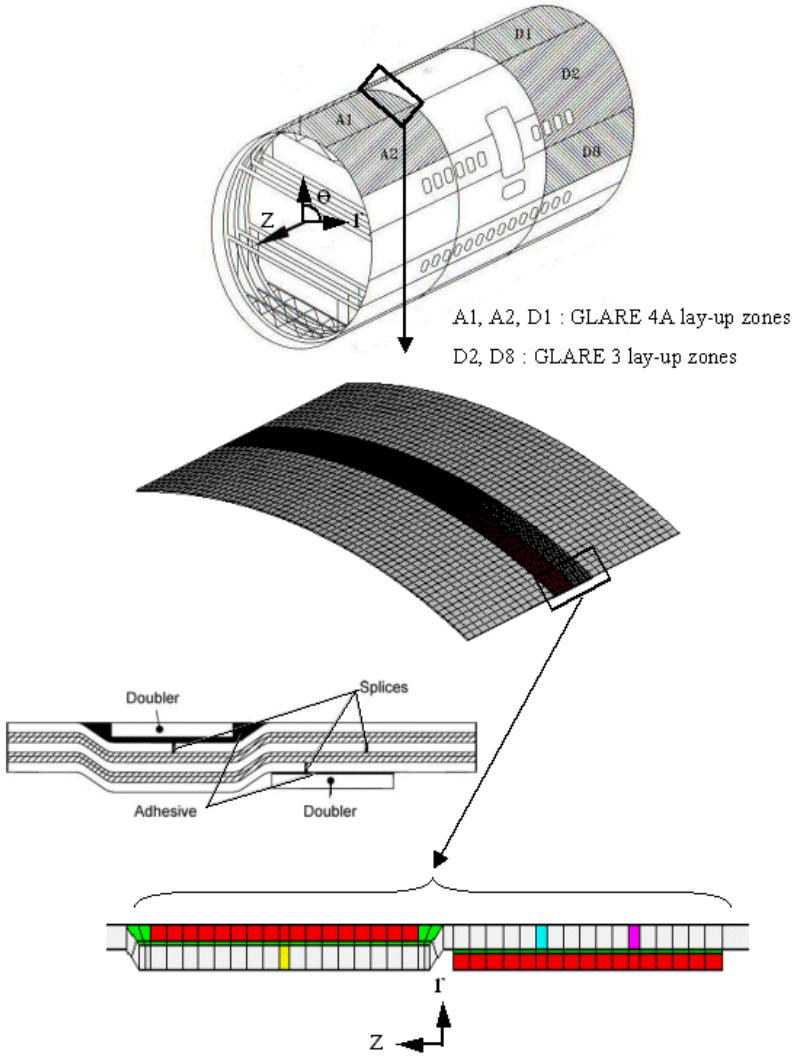

Fig. 5.2 Fuselage skin model for finite element analysis (Figure for fuselage cylinder obtained from Vlot and Gunnink [82])

The lay-ups for the GLARE® panel, the doubler plates used for providing additional stiffness and the intermediate joint zones between two GLARE® panels are shown in Fig. 5.3.

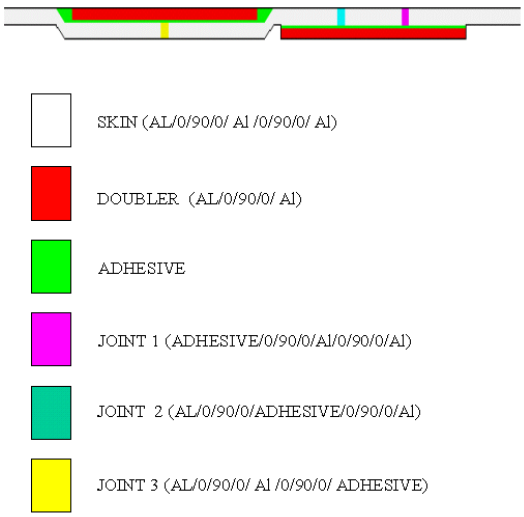

Fig. 5.3 Splice geometry and its lay-up using layered solid element

The fuselage skin and the doublers in the splice are modeled using layered composite element. The lay-up considered for the skin is GLARE® 4A-3/2-0.31 while the lay-up for the two doublers is assumed to be GLARE® 4A-2/1-0.31. One integration point is used to represent each layer so the results obtained are at the middle of each layer. The GLARE® panel has 3 aluminum layers and 6 GFRP layers and hence requires 9 integration points through the thickness. Similarly, the doublers require 5 integration points while each of the joint again requires 9 integration points. The regions with

adhesive are modeled with homogenous 3D elements. The dimensions used for the GLARE® panel model representing the fuselage skin are shown in Fig. 5.4.

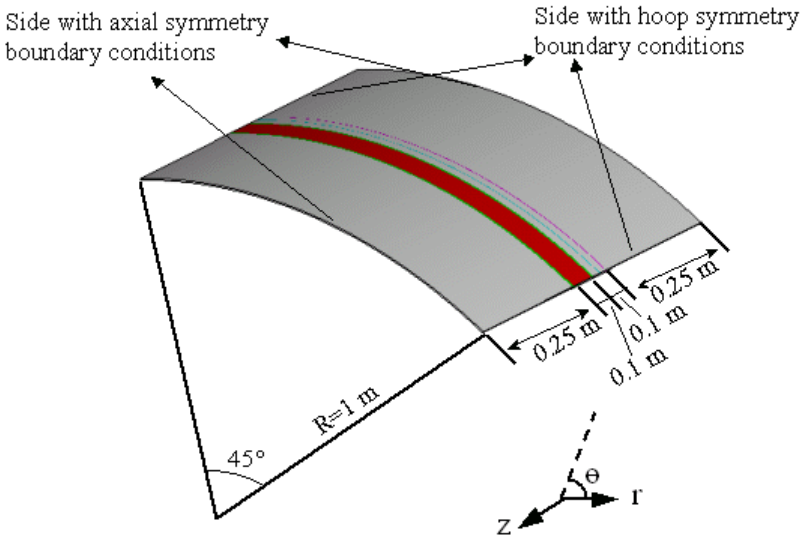

Fig. 5.4 Dimensions of the GLARE® panel

The symmetric hoop and axial boundary conditions are applied on the sides shown in Fig. 5.4. The boundary conditions can be expressed in terms of the co-ordinate axes (r, ɵ, z) as follows:

$u_\Theta = 0$ at $\theta = 67.5^\circ$, 112.5° and $t \geq 0$

$u_z = 0$ at $z = 0, 0.7$ m and $t \geq 0$

The GLARE® panel is analyzed for a time dependent internal pressure loading. The loading cycle is shown in Fig. 5.5. Such a cycle shape is selected to approximately simulate the pressure loading during take-off, in-flight and landing.

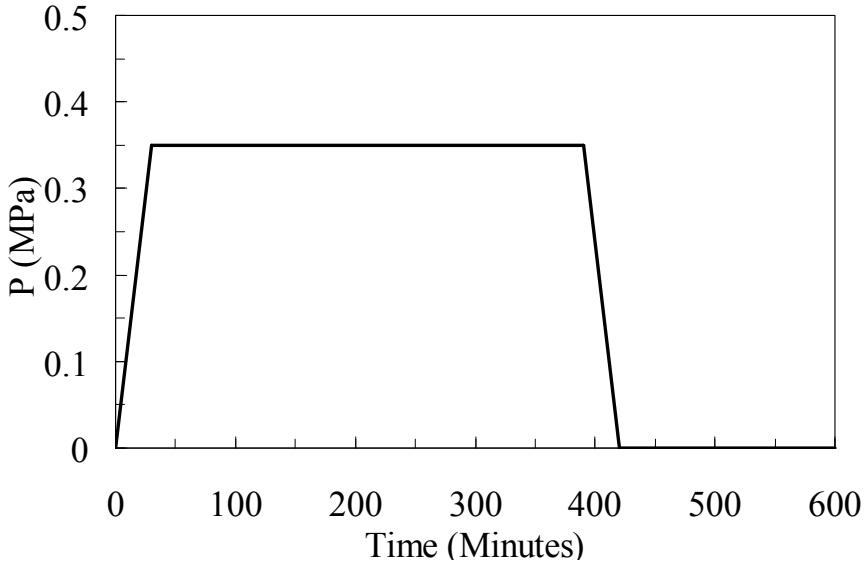

Fig. 5.5 Loading cycle for internal pressure

The applied boundary conditions (on the nodal points) and internal pressure (applied on the element faces) on the finite element model are shown in Fig. 5.6.

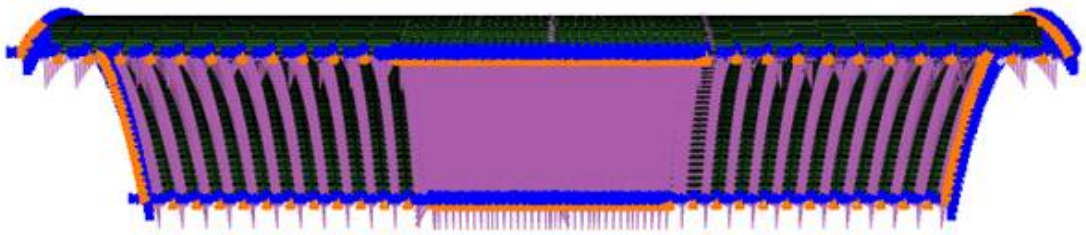

Fig. 5.6 Applied internal pressure and boundary conditions on FE model

5.3 RESULTS AND DISCUSSION

The total displacement of the panel at a typical time of 600 minutes is shown in Fig. 5.7. The displacement plot shows a very small displacement at the splice zone. This indicates that the doublers provide with sufficient stiffening at the interface. It is also observed that at 390 minutes, the displacement increases though the pressure is fixed constant. This is due to the viscoelastic constituents otherwise no additional displacement should occur after 30 minutes. The displacement plot at time of 420 minutes shows a small magnitude of displacement though the internal pressure is zero at this time. This is due to a gradual recovery of a viscoelastic material instead of an instantaneous one.

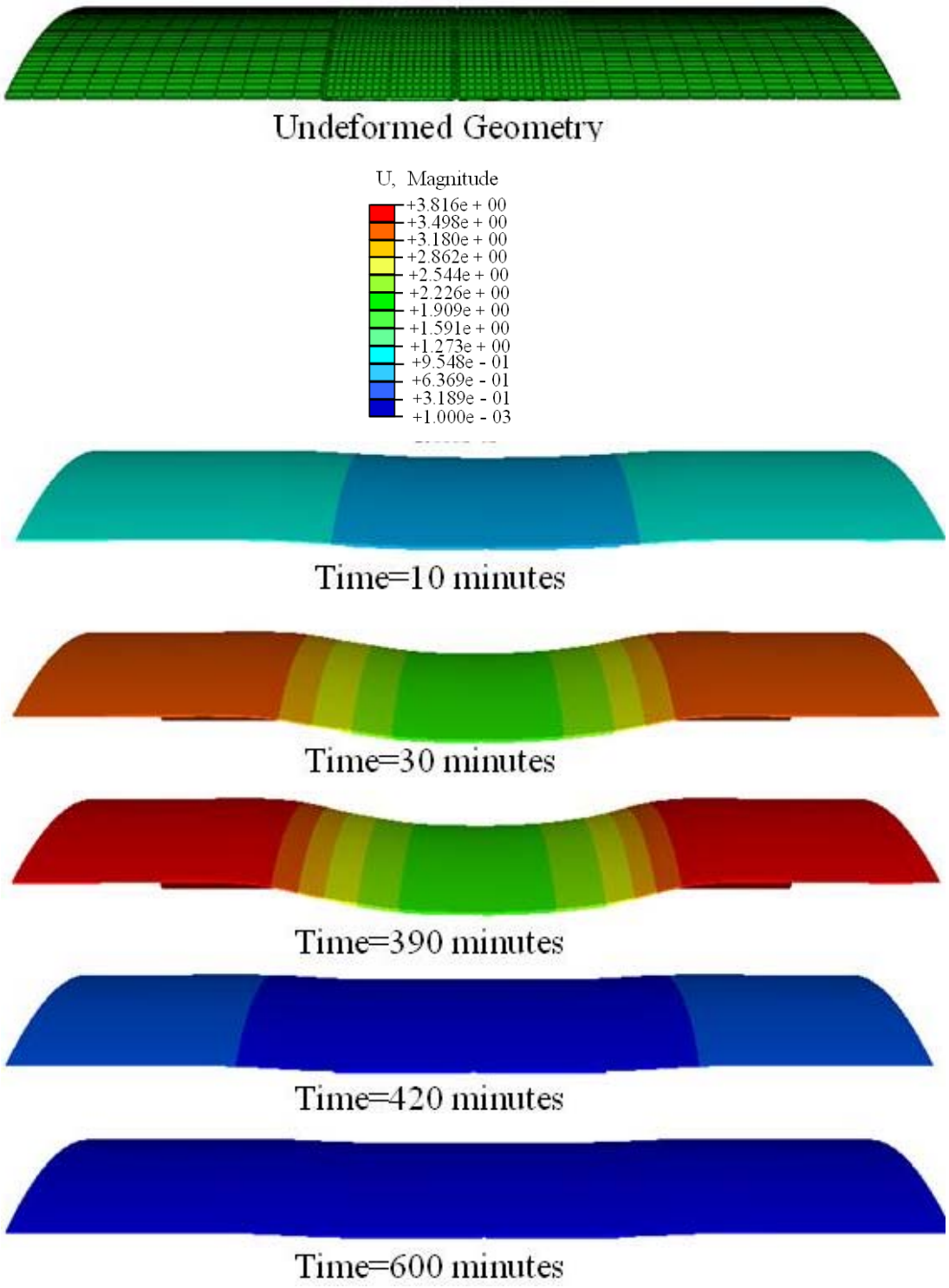

Fig. 5.7 Displacement (magnitude) contour for the panel at various times (unit of displacement is mm)

The stress-time and strain-time responses are monitored at the locations shown in Fig. 5.8.

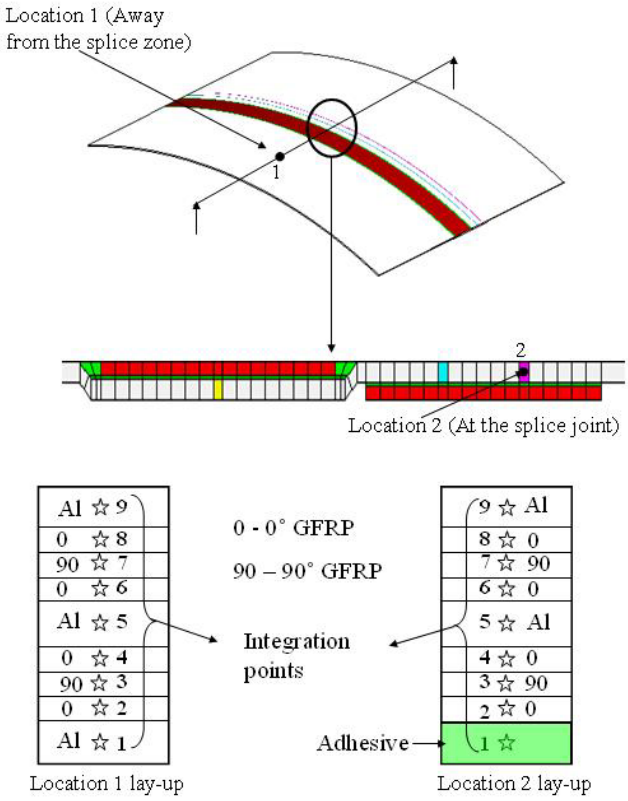

Fig. 5.8 Locations with lay-up details selected for plotting stress-time and strain-time results

The stress-time and strain-time results at the location 1 are shown in Fig. 5.9. The magnitude of hoop stresses and strains are large as compared to the stresses and strains in the other directions and hence represent the critical parameters governing the design of the GLARE® panel.

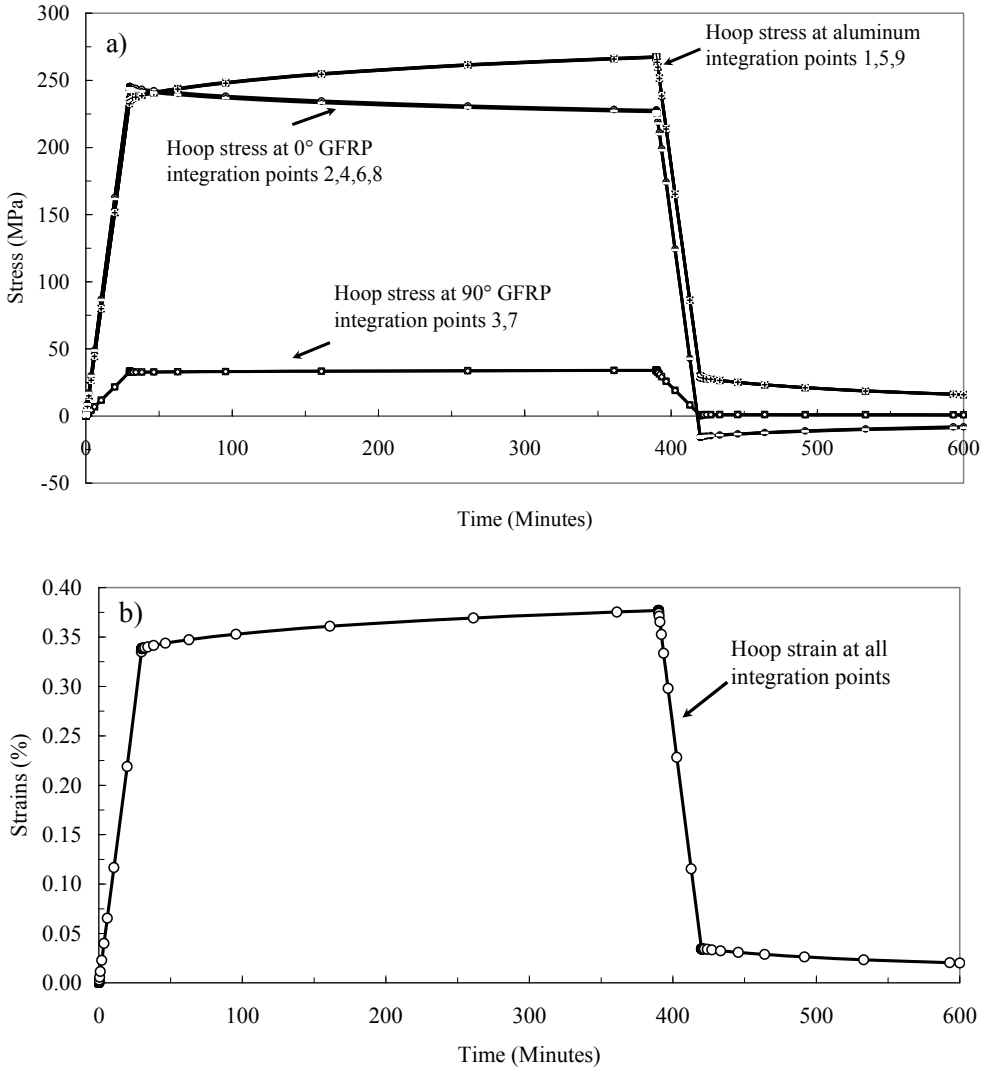

Fig. 5.9 a) Hoop stress and b) Hoop strain plots for GLARE® skin at location 1 (away from splice)

The stress-time plots at various integration points of a single element show same stress values for all the aluminum layers. This indicates a negligible effect of through-thickness location of the laminate due to the fact that FML form thin sections. The stress-time plots also indicate an increase in hoop stresses with time for the aluminum layers while the 0 GFRP layers exhibit a stress relaxation with time due to the

viscoelastic effects. The strain-time plot shows the viscoelastic strains in the hoop direction, which show strain continuity within layers. The plot also shows a gradual decrease in the hoop strain with time after the loading is removed (at t=420 min) indicating a recovery of the response. The stress-time and strain-time plots at the joint 1 (location 2) of Fig. 5.8 are also shown in Fig. 5.10.

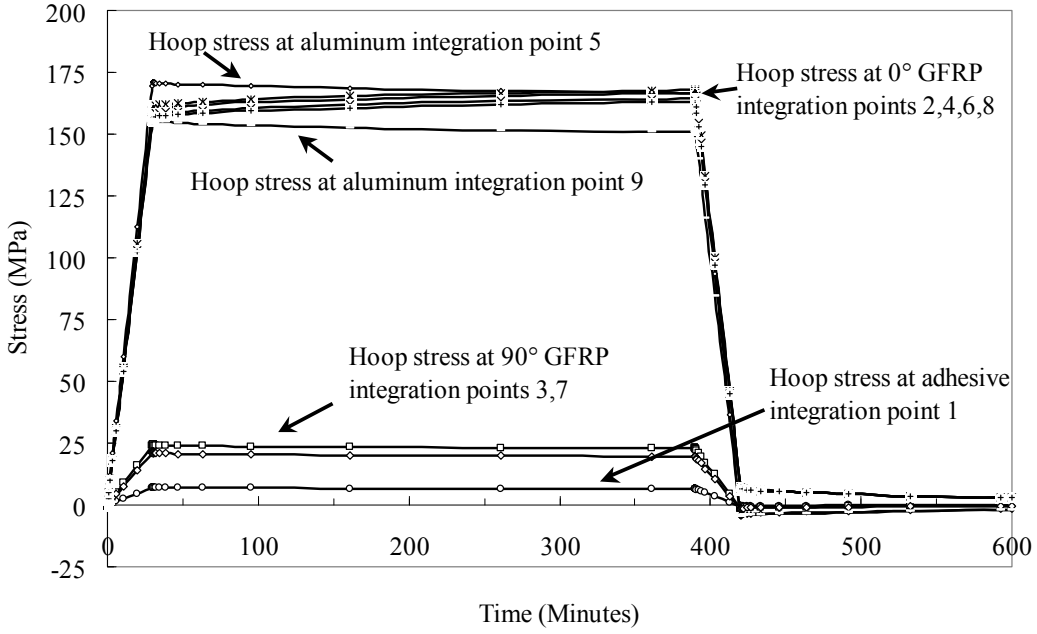

Fig. 5.10 Hoop stress and strain plots for GLARE® skin at joint 1 (location 2)

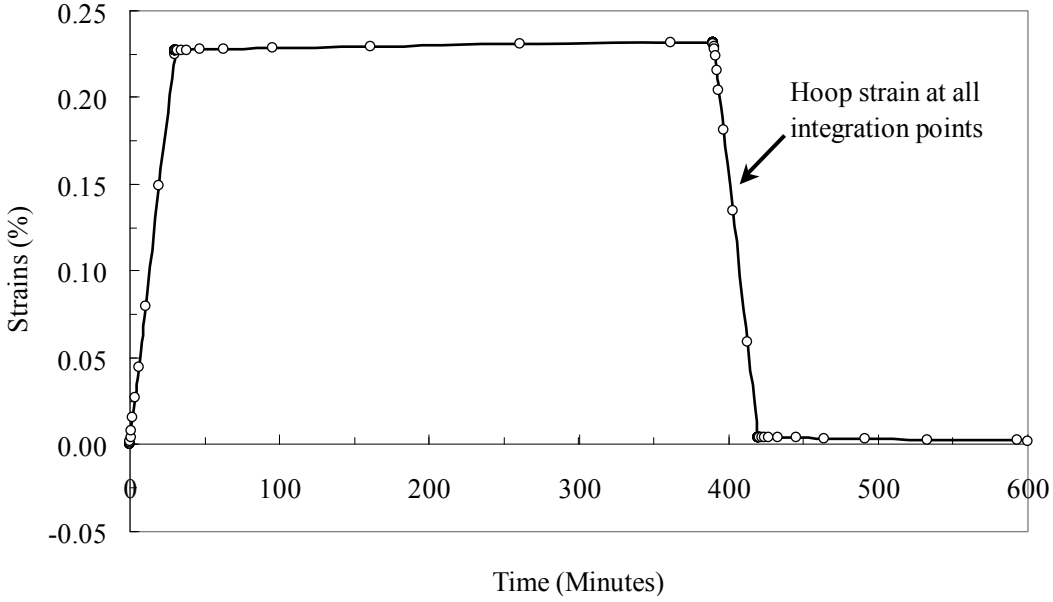

Fig. 5.10 (Continued)

The magnitude of stresses and strains at this location are lower than those at location 1. This is due to the presence of the inner doubler plate, which shares a part of the loading. A variation of stress across thickness is also observed at this location. The outermost layer of aluminum experiences the maximum hoop stress. The Von Mises stress contour for the homogenous elements of the adhesive layers between the GLARE® panel and the inner and outer doublers are shown in Fig. 5.11. The maximum value can be compared with the ultimate strength to check for failure of the adhesive. Apart from this failure mode, it is also required to check for the bonding strength of the adhesive in shear across the interface. The shear stress τ_{rz} induced in the adhesive is shown in Fig. 5.12. The high values of this stress at the edges are responsible for debonding.

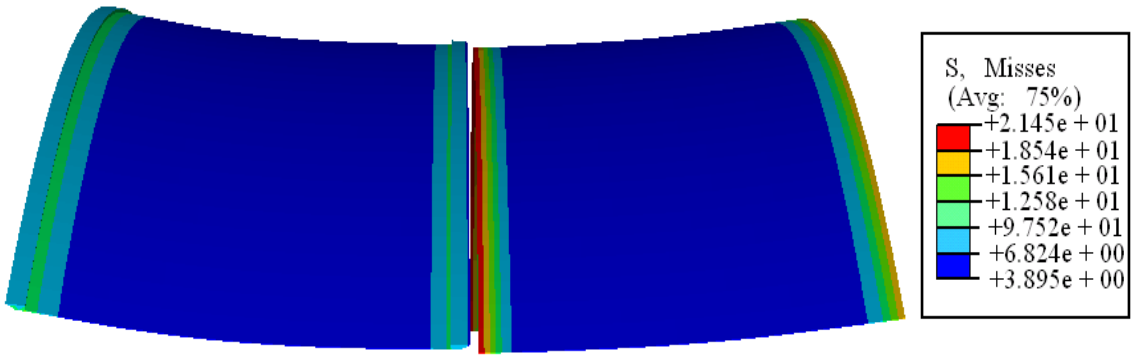

Fig. 5.11 Von-Mises stress contour for the adhesive layer (units are in MPa) at t=30 min

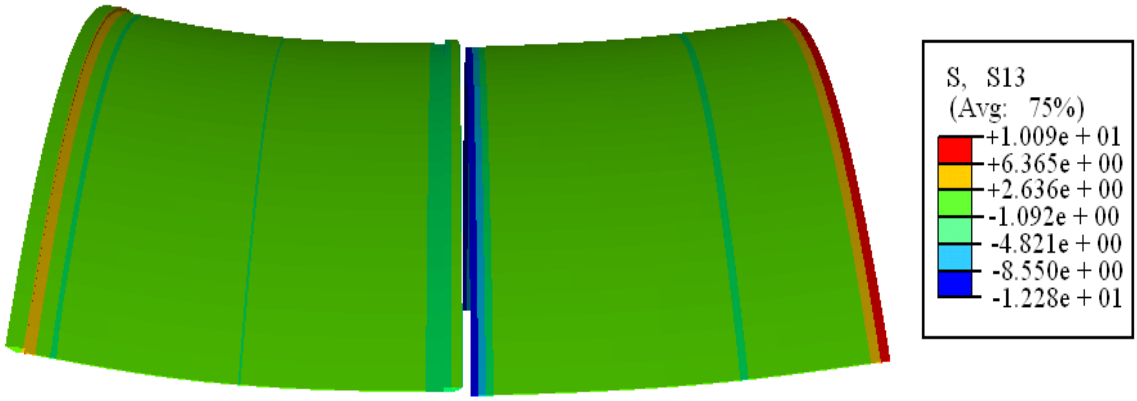

Fig. 5.12 Shear stress (σ_{rz}) contour for the adhesive layer (units are in MPa) at t=30 min

The above analysis can be used for design and optimizing thickness and material lay-ups in the FML and doublers. The suitability of adhesive at high temperatures can be assessed. However, these design verification and optimization procedures are not in the scope of this work. The above analysis has been performed with an objective of successfully applying the thermo-viscoelastic framework to FML structures. This analysis verifies the successful application of the multi-scale framework for time dependent analysis of practical structural components. Many applications require the

consideration of only the nonlinear elastic behavior of materials. The framework can be easily adjusted for obtaining the nonlinear time-independent responses of the FML systems. Instead of using the composite layered element, the developed integrated sublaminate-micromodel can also be applied for analysis of practical structural components made of a few GLARE® varieties (GLARE 1 and GLARE 2) and all the ARALL material systems. The capability of monitoring time-dependent responses can be extended to study ageing effects, which is long-term responses, on the aircraft components.

CHAPTER VI

CONCLUSIONS AND FURTHER RESEARCH

6.1 CONCLUSIONS

A multi-scale framework for analyzing nonlinear time, temperature, and stress dependent responses of fiber metal laminates (FML) has been developed. The highest scale includes layered composite and/or continuum elements within the finite element (FE) structural analyses. A sublaminate model, which homogenizes different responses of the fiber reinforced polymers (FRP) and metal layers, has been formed and implemented in the 3D continuum elements. Alternatively, responses from the FRP and metal layers can be individually implemented on the 3D layered composite elements. It is also possible to obtain the nonlinear time-dependent behaviors of the FRP layers through a micromechanical model of FRP. The lowest level presents 3D constitutive material model of general nonlinear viscoelastic responses. These constitutive models have been formed for the orthotropic FRP and metal layers and constituents of the homogenization models (fiber, matrix and metal constituents). The research findings and conclusions are discussed as follows:

1. A time-integration algorithm for analyzing nonlinear thermo-viscoelastic responses of general orthotropic materials has been developed, which is the lowest scale of the framework. The Schapery's integral model for stress dependent viscoelastic materials has been modified to make it suitable for thermo-viscoelastic analyses of orthotropic materials with stress and temperature

dependent material constants. The constitutive model is suitable for small deformation gradient problems. A recursive-iterative algorithm has been formed to solve the thermo-viscoelastic constitutive model numerically. This algorithm is compatible with displacement based FE code and multi-scale material framework. The recursive-iterative (time-integration) algorithm has been validated with available creep test data of glass-epoxy and glass vinyl-ester composites. The algorithm can be easily reduced for isotropic thermo-viscoelastic responses, thermo-elastic responses, and/or for linear elastic responses of materials.

2. Homogenization at various scales has been done for efficient analysis of heterogeneous composites. The micromechanical (ply level) and sublaminate (laminate level) models have been successfully formulated and incorporated into the multi-scale framework. The micromechanical model of unidirectional FRP layers has been developed to homogenize different nonlinear thermo-viscoelastic response of the fibers and matrix systems. The micromodel consists of four fibers and matrix subcells. Perfect bond along the subcell's interphases has been imposed. The capabilities of the micromechanical model in predicting effective thermo-viscoelastic responses of multi-axial FRP have been verified using data for Kevlar-epoxy and Kevlar-polyimde composites. The constitutive models for orthotropic fibers and isotropic matrix are incorporated in the four subcells. The sublaminate model has been formulated to homogenize different responses of FRP and metal layers. The homogenization scheme is based on the 3D

lamination theory assuming an in-plane strain and out of plane stress continuity and a perfect bond between layers.

3. Two multi-scale approaches have been developed for analyzing nonlinear thermo-viscoelastic responses of FML. One of the approaches is the use of the layered composite element for the FML. The formulation of the stiffness matrix for this element is similar to that for a homogenous 3D element and the effect of the heterogeneous layers is incorporated in the element stiffness matrix during numerical integration. The constitutive viscoelastic material models are calculated at the respective Gaussian points, which represent the FRP and aluminum layers of the FML. In the second approach, the sublaminate model is used to homogenize the response of FRP and metal layers of FML. This effective homogenized anisotropic response of the FML is then sampled at the Gaussian points of 3D continuum elements.
4. The multi-scale framework is applied for time dependent analysis of FML structures. A finite element model representing a FML fuselage structure is created and assigned with layered composite elements. The time dependent responses for various constituents of the structure such as GLARE® fuselage and doubler panels with different lay-ups and the epoxy adhesive between panels are obtained in the analysis.

This multi-scale framework can be applied to a broad class of composites including laminated composites and other multi-layered composites with unidirectional

reinforcements. In this research, the framework has been successfully employed for analysis of a new class of hybrid composites- the fiber metal laminates.

6.2 FURTHER RESEARCH

A complete study of time dependent responses of composites should include other transport mechanisms, such as moisture absorption and their detrimental effects on the mechanical properties. Constituents of composites and fiber metal laminates, especially, polymers are prone to physical and chemical ageing. The current multi-scale framework can be modified to account for these effects. Damage mechanics is another important area for composite materials. The synergy of fatigue and viscoelasticity can be explored by incorporating the damage mechanics within the framework at the ply and laminate level. The inclusion of damage would also require the use of suitable failure theories in conjunction with cohesive elements. These elements are capable of capturing the local stiffness degradation in the material due to damage. The developed framework can be extended to incorporate the effects of thermal conductivity and coefficient of thermal expansion of each layer within the sublaminate and also the effects of the thermal conductivity and coefficient of thermal expansion of the fiber and matrix constituents within the FRP micromodel. The residual thermal stresses induced during manufacturing and in service in the constituents can be calculated by including these thermal effects. The sublaminate model developed for this framework consists of two layers (one FRP and one metal layer) and can be applied to a few types of GLARE® laminates. The development of more varieties of hybrid composites and fiber metal laminates makes it

essential to have a sublaminate model with more than two layers. The inclusion of other coupled field effects such as piezoelectric effect and magnetostrictive effect may also be considered. A multi-scale framework with all the above features would result in a ideal framework for multi-field analyses of a broad class of composite materials and structures.

REFERENCES

1. Aboudi, J.: Mechanics of Composite Materials: A Unified Micromechanical Approach. Elsevier, Amsterdam (1991)
2. Alwis, K.G.N., Burgoyne, C.J.: Time-temperature superposition to determine the stress-rupture of aramid fibers. Appl. Compos. Mater. **13**, 249-264 (2006)
3. Antonakakis, J.N., Bhargava, P., Chuang, K.C., Zehnder, A.T.: Linear viscoelastic properties of HFPE--II--52 polyimide. J. Appl. Pol. Sci. **100**, 3255--3263 (2006)
4. Barbero, E.J., Reddy, J.N., Teply, J.L.: Accurate determination of stresses in ARALL laminates using a generalized laminate plate theory. AMD Symposium Series ASME Applied Mechanics Division 10, 55-62 (1989)
5. Benedikt, B., Rupnowski, P., and Kumosa, M.: Viscoelastic stress distribution and elastic properties in unidirectional composites with large volume fractions of fibers. Acta Mater. **51**, 3483-3493 (2003)
6. Botelho, E., Pardini, L., Rezende, M.: Hygrothermal effects on damping behavior of metal/glass fiber/epoxy hybrid composites. Mat. Sci. and Eng.-A **399**, 190-198 (2005)
7. Brinson, L.C., Knauss, W.G.: Thermorheologically complex behavior of multiphase viscoelastic materials. J. Mech. Phys. Solids **39**(7), 859-880 (1991)
8. Caruthers, J.M., Adolf, D.B., Chambers, R.S., Shrikhande, P.: A thermodynamically consistent, nonlinear viscoelastic approach for modeling glassy polymers. Polymer **45**, 4577-4597 (2004)

9. Caruthers, J., Cohen, R.: Consequences of thermo-rheological complexity in viscoelastic materials. Rheol. Acta. **19**, 606-613 (1980)
10. Chen, J., Sun, C. T.: Modeling of orthotropic elastic-plastic properties of ARALL laminates. Compos. Sci. Tech. **36,** 321-337 (1989)
11. Christensen, R. M.: Theory of Viscoelasticity. Dover Publications, New York (2003)
12. Christensen, R. M.: Mechanics of Composite Materials. Dover Publications, New York (2005)
13. Cortes, P., Cantwell, W.: The tensile and fatigue properties of carbon fiber-reinforced PEEK-titanium fiber-metal laminates. Journal of Reinforced Plastics and Composites **23**(15), 1615-1623 (2004)
14. Dillard, D., Brinson, H.: A numerical procedure for predicting creep and delayed failures in laminated composites. Long-Term Behavior of Composites, Symposium, Williamsburg, VA, USA, ASTM, Philadelphia, Pa, USA, 22-37 (1983)
15. Donnellan, M., Cook, J.: Metal/Polymer Reinforced Laminates: Potential Candidates for Space Applications. 23rd International SAMPE Technical Conference, 777-786 (1991)
16. Eckold, G.: Design and Manufacture of Composite Structures, Mc-Graw Hill, New York (1994)
17. Feng, W. W.: A recurrence formula for viscoelastic constitutive equations. Int. J. Nonlinear Mech. **27**(4), 675-678 (1992)
18. Findley, W.N., Lai, J.S., Onaran, K.: Creep and Relaxation of Nonlinear Viscoelastic Materials, Dover Publications, New York (1989)

19. Fish, J., Shek, K., Pandheeradi, M., Shepard, M.: Computational plasticity for composite structures based on mathematical homogenization: Theory and practice. Comput. Methods Appl. Mech. Eng. **148**, 53-73 (2000)
20. Fish, J., Shek, K.: Multiscale analysis of composite materials and structures. Compos. Sci. Tech. **60**, 2547-2556 (2000)
21. Gramoll, K., Dillard, D., Brinson, H.: A stable numerical solution method for in-plane loading of nonlinear viscoelastic laminated orthotropic materials. Compos. Struct. **13**, 251-274 (1989)
22. Haddad, Y.M. and Tanari, S.: On the micromechanical characterization of the creep response of a class of composite systems. J Press. Vessel Technol. Trans. ASME, **111**(2), 177-182 (1989)
23. Haftchenari, H., Al-Salehi, F.A.R., Al-Hasani, S.T.S., Hinton, M.J.: Effect of the temperatures on the tensile strength and failure modes of angle ply aramid fiber (KRP) tube under hoop loading. Appl. Compos. Mater. **9**, 99-115 (2002)
24. Haga, O., Kimura, M.: Tensile properties of Al/CFRP multilayered hybrid composite material. J. Society of Mater. Sci. Japan **35**: 1411-1417 (1986)
25. Haga, O., Koyama, H., Kawada, K.: Mechanical properties of a new type super hybrid material. Advanced Compos. Mater. **5**(2), 139-149 (1996)
26. Haj-Ali, R.: Nested nonlinear multi-scale framework for the analysis of thick-section composite materials and structures. In: Multiscale Modeling and Simulation of Composite Materials and Structures, Eds. Kwon, Y. W., Allen, D.H., and Talreja, R., Springer, New York, 332-371 (2007)

27. Haj-Ali, R., Hakan K., Abdul-Hamid, Z.: Three-dimensional micromechanics-based constitutive framework for analysis of pultruded composite structures. J. Eng. Mech. **127**(7), 653-660 (2001)

28. Haj-Ali, R. Muliana, A.: A micromechanical constitutive framework for the nonlinear viscoelastic behavior of pultruded composite materials. Int. J Solids Struct. **40**(5), 1037-1057 (2003)

29. Haj-Ali, R., Muliana, A.: Numerical finite element formulation of the schapery nonlinear viscoelastic material model. Int. J. Numer. Method Eng. **59**(1), 25-45 (2004)

30. Haj-Ali, R. and Muliana, A.: A multi-scale constitutive formulation for the nonlinear viscoelastic analysis of laminated composite materials and structures. Int. J Solids Struct., **41**(13), 3461-3490 (2004)

31. Haj-Ali, R.M., Muliana, A.H.: A micro-to-meso sublaminate model for the viscoelastic analysis of thick-section multi-layered FRP composite structures. Mech. Time Depend. Mater. **12**(1), 69-93 (2008)

32. Haj-Ali, R.M., Pecknold, D.A.: Nested 3-D micromechanical and damage models for analysis of laminated composite structures. In: Modeling and Simulation Based Engineering, edited by S.N. Atluri, and P.E. O'Donoghue, Tech Science Press, Proceedings of the International Conference on Computational Engineering Science, ICES98, October, Atlanta, GA, 1518-1525 (1998)

33. Halpin, J.C., Pagano, N.J.: Observation on linear anisotropic viscoelasticity. J. Compos. Mater. **2**(1), 68-81 (1968)

34. Hanson, M.P.: Feasibility of Kevlar 49/PMR-15 polyimide for high temperature applications. In: 12th National SAMPE Technical Conference, pp. 1-15. 7-9 October (1980)

35. Harris, C.E., Gates, T.S. (eds.): High temperature and environmental effects on polymeric composites. ASTM, Philadelphia, ASTM STP Paper No. 1174 (1993)

36. Harper, B.D., Weitsman, Y.: Characterization method for a class of thermorheologically complex materials. J. Rheol. **29**, 49-66 (1985)

37. Hashagen, F., Schellekens, J., Borst, R.: Finite element procedure for modeling fibre metal laminates. Compos. Struct. **32**, 255-264 (1995)

38. Hashin, Z., Humprey, E.A., Goering, J.: Analysis of thermoviscoelastic behavior of unidirectional fiber composites. Compos. Sci. Tech. **29**, 103-131 (1987)

39. Henriksen, M.: Nonlinear viscoelastic stress analysis - A finite element approach. Comput. Struct. **18**(1), 133-139 (1984)

40. Hilton H., Yi S.: The significance of (an)isotropic viscoelastic poisson ratio stress and time dependencies. Int. J. Solids Struct. **35**(23), 3081-3095 (1998)

41. Kaliske, M., Rothert, H.: Formulation and implementation of three-dimensional viscoelasticity at small and finite strain. Computational Mechanics **19**, 228-239 (1997)

42. Kawai, M., Morishita, M., Tomura, S., Takumida, K.: Inelastic behavior and strength of fiber-metal hybrid composite: GLARE. Int. J. Mech. Sci. **40**(2-3), 183-198 (1998)

43. Kennedy, T.C.: Nonlinear viscoelastic analyses of composite plates and shells. Compos. Struct. **41**, 265-272 (1998)

44. Krishnakumar, S.: Fiber metal laminates - The synthesis of metals and composites. Materials and Manufacturing Processes **9**(2), 295-354 (1994)

45. Lai, J., Bakker, A: 3-D Schapery representation for nonlinear visco-elasticity and finite element implementation. Comput. Mech. **18**, 182-191 (1996)

46. Levesque, M., Katell Derrien, K., Baptiste, D., Gilchrist, M.: On the development and parameter identification of Schapery-type constitutive theories. Mech. Time Dependent Mater. **12**(2), 95-127 (2008).

47. Lou, Y.C., Schapery, R.A.: Viscoelastic characterization of a nonlinear fiber-reinforced plastic. J. Compos. Mater. **5**, 208-234 (1971)

48. Marias, C., Villoutreix, G: Analysis and modeling of the creep behavior of the thermostable PMR-15 polyimide. J. Appl. Polymer Sci. **69**, 1983-1991 (1998)

49. Morgan, R.J., Shih, E.E., Lincoln, J.E.: Thermal properties of high temperature polymer matrix fibrous composites. In: Handbook of Thermal Analysis and Calorimetry vol.3 edited by Cheng, S.Z.D., Elsevier Sci., Amsterdam, 491-518 (2002)

50. Morland, L.W., Lee, E.H.: Stress analysis for linear viscoelastic materials with temperature variations. Soc. Rheol. Trans. **4**, 233--263 (1960)

51. Muliana, A.H.: Multi-scale framework for the thermo-viscoelastic analyses of polymer composites," Mech. Res. Commun. **34**, 561-567 (2007)

52. Muliana,A.H., Haj-Ali, R.M.: Nested nonlinear viscoelastic and micromechanical models for the analysis of pultruded composite structures. Mech. Mater. J. **36**, 1087-1110 (2004)

53. Muliana, A. H., Haj-Ali, R.M.: Multi-scale modeling for the long-term behavior of FRP composite structures. AIAA J. **43**(8), 1815-1822 (2005)

54. Muliana, A.H., Haj-Ali, R.M.: A multi-scale framework for layered composites with thermo-rheologically complex behaviors. Int. J. Solids Struct. **45**(10), 2937-2963 (2008)

55. Muliana, A.H., Khan, K.A.: A time integration algorithm for thermo--rheologically complex polymers. Comput. Mater. Sci. **41**, 576-588 (2008)

56. Muliana, A.H., Kim, J.S.: A concurrent micromechanical model for nonlinear viscoelastic behaviors of composites reinforced with solid spherical particles. Int. J. Solids Struct. **44**, 6891-6913 (2007)

57. Muliana A., Nair A., Khan K., Wagner S.: Characterization of thermo-mechanical and long-term behaviors of multi-layered composite materials. Compos. Sci. Tech. **66**(15), 2907-2924 (2006)

58. Muliana, A.H., Sawant, S.P.: Responses of fiber reinforced polymer composites having time and temperature dependent constituent properties. Acta Mech. Available Online DOI 10.1007/s00707-008-0052-4, (2008)

59. Nemat-Nasser, S., Hori, M.: Micromechanics: Overall Properties of Heterogeneous Materials. Elsevier, Amsterdam (1999)

60. Odegard, G., Kumosa, M.: Elastic-plastic and failure properties of a unidirectional graphite/PMR-15 composite at room and elevated temperatures. Compos. Sci. Tech. **60**(16), 2979-2988 (2000)

61. Pecknold, D., Haj-Ali, R.: Integrated micromechanical/structural analysis of laminated composites. 1st Joint Mechanics Meeting of ASME/ASCE/SES-MEET'N93, Charlottesville, VA, USA, ASME, New York, NY, USA. 197-206 (1993)

62. Pecknold, D., Rahman, S.: Micromechanics-based structural analysis of thick laminated composites. Compos. Struct. **51**(2), 163-179 (1994)

63. Peretz, D., Weitsman, Y.: The nonlinear thermoviscoelastic characterizations of FM-73 adhesive. J. Rheol. **27**(2), 97-114 (1983)

64. Pindera, M., Williams, T., Machaeret, Y.: Time-dependant response of Aramid-Epoxy-Aluminium sheet, ARALL laminates. Polymer Compos. **10**(5), 328-336 (1989)

65. Poon, H., Ahmad, F.: A material point time integration procedure for anisotropic, thermo-rheologically simple, viscoelastic solids. Comput. Mech. **21**, 236-242 (1998)

66. Poon, H., Ahmad, F.: A finite element constitutive update scheme for anisotropic, viscoelastic solids exhibiting non-linearity of the Schapery type. Int. J. Numer. Method Eng. **46**, 2027-2041 (1999)

67. Rajagopal, K., Srinivasa, A.: A note on the correspondence principle of nonlinear viscoelastic materials. Int. J. Fracture **131**, 47-52 (2005)

68. Ramberg, W., Osgood, W.R.: Description of stress-strain curves by three parameters. *Technical Note No. 902*, National Advisory Committee for Aeronautics, Washington DC. 1943.

69. Reddy, J.N.: Mechanics of Laminated Composite Plates and Shells: Theory and Analysis. CRC Press LLC, Boca Raton, FL (2004)

70. Rommel, M., Konopka, L., Kane, R.: Effect of matrix resins on the mechanical properties of titanium/composite hybrid laminates. In: Proceedings of International SAMPE Symposium and Exhibition **44** (1), 1-15 (1999)

71. Rupnowski, P., Gentz, M., Kumosa, M.: Mechanical response of a unidirectional graphite fiber/polyimide composite as a function of temperature. Compos. Sci. Tech. **66**, 1045-1055 (2006)

72. Sadkin, Y., Aboudi, J.: Viscoelastic behavior of thermo-rheologically complex resin matrix composites. Compos. Sci. Tech. **36**, 351-365 (1989)

73. Sawant, S., Muliana A.: A thermo-mechanical viscoelastic analysis of orthotropic media. Compos. Struct. **83**(1), 61-72 (2007)

74. Schapery, R.A.: On the characterization of nonlinear viscoelastic materials. Polym. Eng. Sci. **9**(4), 295-310 (1969)

75. Scott, D., Lai, J., Zureick, A.: Creep behavior of fiber-reinforced polymeric composites: A review of the technical literature. Reinforced Compos. Plastics **14**, 588-617 (1995)

76. Simo, J.C., Hughes, T.J.R.: Computational Inelasticity, Springer-Verlag, New York (1998)

77. Sui, G., Zheng, Z., Zhou, C., Shi, C.: Vinylon reinforced aluminum laminate. J. Mater. Sci. **9**, 382-384 (1993)

78. Taylor, R.L., Pister, K.S., Goudreau, G.L.: Thermo-mechanical analysis of viscoelastic solids. Int. J. Numer. Methods Eng. **2**, 45-59 (1970)

79. Van Rooijen, R., Sinke, J., De Vries, T., Van der Zwaag, S.: Property optimisation in fibre metal laminates. Appl. Compos. Mater. **11**, 63-76 (2004)

80. Vermeeren, C.: An historic overview of the development of fibre metal laminates. Appl. Compos. Mater. **10**, 189-205 (2003)

81. Vermeeren, C., De Kanter, J.: GLARE® design aspects and philosophies. Appl. Compos. Mater. **10**, 257-276 (2003)

82. Vlot, A., Gunnink, J.: Fibre Metal Laminates: An Introduction. Kluwer Academic Publishers, Dordrecht, The Netherlands (2001)

83. Walruth, D. E.: Viscoelastic response of a unidirectional composite containing two viscoelastic constituents. Expt. Mech. **31**(2), 111-117 (1991)

84. Walton, P.L., Majumdar, A.J.: Creep of Kevlar-49 fibre and a Kevlar-49 cement composite. J. Mater. Sci. **18**, 2939-2946 (1983)

85. Wang, J.Z., Dillard, D.A.: Testing of viscoelasticity of single fibers under transient moisture conditions. Expt. Techniques **15**(5), 47-49 (1991)

86. Wang, J.Z., Dillard, D.A., Ward, T.C.: Temperature and stress effects in the creep of aramid fibers under transient moisture conditions and discussions on the mechanisms. J. Polym. Sci., Part B **30**, 1391-1400 (1992)

87. White, S.R., Hartman, A.B.: Effect of cure state on stress relaxation in 3501-6 epoxy resin. J. Eng. Mater. Tech., Transactions of the ASME, **119**(3), 262-265 (1997)

88. Wineman, A.S., Rajagopal, K.R.: Mechanical Response of Polymers: An Introduction, Cambridge University Press, London, U.K (2000)

89. Yi, S., Hilton, H., Ahmad, M.F.: Nonlinear thermo-viscoelastic analysis of interlaminar stresses in laminated composites. J. Appl. Mech. **63**, 218-224 (1996)

90. Yu, Q., Fish, J., Multi-scale asymptotic homogenization for multiphysics problems with multiple spatial and temporal scales: a coupled thermo-viscoelastic example problem, Int. J Solids Struct. **39**, 6429-6452 (2001)

91. Zienkiewicz O.C., Watson M., King I.P.: A numerical method of visco-elastic stress analysis. Int. J. Mech. Sci. **10**, 807-827 (1968)

92. Zocher, M.A., Groves, S.E., and Allen, D.H: A three-dimensional finite element formulation for thermoviscoelastic orthotropic media. Int. J. Numer. Meth.Eng. **40**, 2267-2280 (1997)

APPENDIX A

This appendix describes a micromechanical relation of a unidirectional composite layer. This was previously introduced by Haj-Ali and Muliana [30] and Muliana and Haj-Ali [52] for nonlinear time-dependent responses on FRP composite materials and structures. The unit cell of the FRP (Fig. 3.1) is composed of four subcells. The first subcell is fiber constituent, while subcells 2, 3, and 4 represent the matrix constituents. The micromodel relations in the axial (fiber) direction are:

$$\begin{aligned} \Delta\varepsilon_{11}^{(1)} &= \Delta\varepsilon_{11}^{(2)} = \Delta\varepsilon_{11}^{(3)} = \Delta\varepsilon_{11}^{(4)} = \Delta\bar{\varepsilon}_{11} \\ V_1\Delta\sigma_{11}^{(1)} + V_2\Delta\sigma_{11}^{(2)} + V_3\Delta\sigma_{11}^{(3)} + V_4\Delta\sigma_{11}^{(4)} &= \Delta\bar{\sigma}_{11} \end{aligned} \tag{A.1}$$

Along the interfaces between the subcells with normal in the x2 direction, the following relation should be fulfilled:

$$\begin{aligned} \Delta\sigma_{22}^{(1)} &= \Delta\sigma_{22}^{(2)} \\ \Delta\sigma_{22}^{(3)} &= \Delta\sigma_{22}^{(4)} \\ \frac{V_1}{V_1+V_2}\Delta\varepsilon_{22}^{(1)} + \frac{V_2}{V_1+V_2}\Delta\varepsilon_{22}^{(2)} &= \Delta\bar{\varepsilon}_{22} \\ \frac{V_3}{V_3+V_4}\Delta\varepsilon_{22}^{(3)} + \frac{V_4}{V_3+V_4}\Delta\varepsilon_{22}^{(4)} &= \Delta\bar{\varepsilon}_{22} \end{aligned} \tag{A.2}$$

$$\begin{aligned} \Delta\tau_{12}^{(1)} &= \Delta\tau_{12}^{(2)} \\ \Delta\tau_{12}^{(3)} &= \Delta\tau_{12}^{(4)} \\ \frac{V_1}{V_1+V_2}\Delta\gamma_{12}^{(1)} + \frac{V_2}{V_1+V_2}\Delta\gamma_{12}^{(2)} &= \Delta\bar{\gamma}_{12} \\ \frac{V_3}{V_3+V_4}\Delta\gamma_{12}^{(3)} + \frac{V_4}{V_3+V_4}\Delta\gamma_{12}^{(4)} &= \Delta\bar{\gamma}_{12} \end{aligned} \tag{A.3}$$

Considering interfaces between subcells with normal in the x3 direction, the micromodel relations are expressed as:

$$\begin{gathered}
\Delta\sigma_{33}^{(1)} = \Delta\sigma_{33}^{(3)} \\
\Delta\sigma_{33}^{(2)} = \Delta\sigma_{33}^{(4)} \\
\frac{V_1}{V_1+V_3}\Delta\varepsilon_{33}^{(1)} + \frac{V_3}{V_1+V_3}\Delta\varepsilon_{33}^{(3)} = \Delta\overline{\varepsilon}_{33} \\
\frac{V_2}{V_2+V_4}\Delta\varepsilon_{33}^{(2)} + \frac{V_4}{V_2+V_4}\Delta\varepsilon_{33}^{(4)} = \Delta\overline{\varepsilon}_{33}
\end{gathered} \tag{A.4}$$

$$\begin{gathered}
\Delta\tau_{13}^{(1)} = \Delta\tau_{12}^{(3)} \\
\Delta\tau_{13}^{(2)} = \Delta\tau_{13}^{(4)} \\
\frac{V_1}{V_1+V_3}\Delta\gamma_{13}^{(1)} + \frac{V_3}{V_1+V_3}\Delta\gamma_{13}^{(3)} = \Delta\overline{\gamma}_{13} \\
\frac{V_2}{V_2+V_4}\Delta\gamma_{13}^{(2)} + \frac{V_4}{V_2+V_4}\Delta\gamma_{13}^{(4)} = \Delta\overline{\gamma}_{13}
\end{gathered} \tag{A.5}$$

Finally, the transverse shear relations are summarized as:

$$\begin{gathered}
\Delta\tau_{23}^{(1)} = \Delta\tau_{23}^{(2)} = \Delta\tau_{23}^{(3)} = \Delta\tau_{23}^{(4)} = \Delta\overline{\tau}_{23} \\
V_1\Delta\gamma_{23}^{(1)} + V_2\Delta\gamma_{23}^{(2)} + V_3\Delta\gamma_{23}^{(3)} + V_4\Delta\gamma_{23}^{(4)} = \Delta\overline{\gamma}_{23}
\end{gathered} \tag{A.6}$$

APPENDIX B

The nonzero components of matrix A_1 are:

$$
\begin{aligned}
&A_1(1,1) = A_1(2,7) = A_1(3,13) = A_1(4,19) = 1 \\
&A_1(5,2) = A_1(9,4) = \frac{V^{(1)}}{V^{(1)}+V^{(2)}} \qquad A_1(5,8) = A_1(9,10) = \frac{V^{(2)}}{V^{(1)}+V^{(2)}} \\
&A_1(6,14) = A_1(10,16) = \frac{V^{(3)}}{V^{(3)}+V^{(4)}} \quad A_1(6,20) = A_1(10,22) = \frac{V^{(3)}}{V^{(3)}+V^{(4)}} \\
&A_1(7,3) = A_1(11,5) = \frac{V^{(1)}}{V^{(1)}+V^{(3)}} \qquad A_1(7,15) = A_1(11,17) = \frac{V^{(3)}}{V^{(1)}+V^{(3)}} \\
&A_1(8,9) = A_1(12,11) = \frac{V^{(2)}}{V^{(2)}+V^{(4)}} \qquad A_1(8,21) = A_1(12,23) = \frac{V^{(4)}}{V^{(2)}+V^{(4)}} \\
&A_1(13,6) = V^{(1)} \quad A_1(13,12) = V^{(2)} \quad A_1(13,18) = V^{(3)} \quad A_1(13,24) = V^{(4)}
\end{aligned}
\tag{B.1}
$$

The nonzero components of the matrix A_2 are:

$$
\begin{aligned}
&A_2(1,1) = C^{(1)}_{2211} \quad A_2(1,2) = C^{(1)}_{2222} \quad A_2(1,3) = C^{(1)}_{2233} \\
&A_2(1,7) = -C^{(2)}_{2211} \quad A_2(1,8) = -C^{(2)}_{2222} \quad A_2(1,9) = -C^{(2)}_{2233} \\
&A_2(2,13) = C^{(3)}_{2211} \quad A_2(2,14) = C^{(3)}_{2222} \quad A_2(2,15) = C^{(3)}_{2233} \\
&A_2(2,19) = C^{(4)}_{2211} \quad A_2(2,20) = C^{(4)}_{2222} \quad A_2(2,21) = C^{(4)}_{2233} \\
&A_2(3,4) = C^{(1)}_{1212} \quad A_2(3,10) = -C^{(1)}_{1212} \quad A_2(4,16) = C^{(3)}_{1212} \quad A_2(4,22) = -C^{(4)}_{1212} \\
&A_2(5,1) = C^{(1)}_{3311} \quad A_2(5,2) = C^{(1)}_{3322} \quad A_2(5,3) = C^{(1)}_{3333} \\
&A_2(5,13) = -C^{(3)}_{3311} \quad A_2(5,14) = C^{(3)}_{3322} \quad A_2(5,15) = C^{(3)}_{3333} \\
&A_2(6,7) = C^{(2)}_{3311} \quad A_2(6,8) = C^{(2)}_{3322} \quad A_2(6,9) = C^{(2)}_{3333} \\
&A_2(6,19) = -C^{(4)}_{3311} \quad A_2(6,20) = -C^{(4)}_{3322} \quad A_2(6,21) = -C^{(4)}_{3333} \\
&A_2(7,5) = C^{(1)}_{1313} \quad A_2(7,17) = -C^{(3)}_{1313} \quad A_2(8,11) = C^{(2)}_{1313} \quad A_2(8,23) = -C^{(4)}_{1312} \\
&A_2(9,6) = A_2(10,6) = A_2(11,6) = C^{(1)}_{2323} \\
&A_2(9,12) = -C^{(2)}_{2323} \quad A_2(10,18) = -C^{(3)}_{2323} \quad A_2(11,24) = -C^{(4)}_{2323}
\end{aligned}
\tag{B.2}
$$

The nonzero components of the matrix D_1 are:

$$
\begin{aligned}
&D_1(1,1) = D_1(2,1) = D_1(3,1) = D_1(4,1) = 1 \\
&D_1(5,2) = D_1(6,2) = D_1(7,3) = D_1(8,4) = 1 \\
&D_1(9,4) = D_1(10,4) = D_1(11,5) = D_1(12,5) = D_1(13,6) = 1
\end{aligned}
\tag{B.3}
$$

APPENDIX C

The strain displacement relations for small strain formulation is given as:

$$\{\varepsilon\} = \begin{Bmatrix} \varepsilon_x \\ \varepsilon_y \\ \varepsilon_z \\ \gamma_{xy} \\ \gamma_{xz} \\ \gamma_{yz} \end{Bmatrix} = \begin{Bmatrix} \dfrac{\partial u}{\partial x} \\ \dfrac{\partial v}{\partial y} \\ \dfrac{\partial w}{\partial z} \\ \dfrac{\partial u}{\partial y} + \dfrac{\partial v}{\partial x} \\ \dfrac{\partial u}{\partial z} + \dfrac{\partial w}{\partial x} \\ \dfrac{\partial v}{\partial z} + \dfrac{\partial w}{\partial y} \end{Bmatrix} \tag{C.1}$$

The Jacobian matrix **[*J*]** of transformation from the isoparametric co-ordinate space to the x-y-z co-ordinates for a 8 noded linear brick element is given as:

$$\{J\} = \frac{1}{8} \begin{bmatrix} -(1-s)(1-t)x_1 + (1-s)(1-t)x_2 & -(1-s)(1-t)y_1 + (1-s)(1-t)y_2 & -(1-s)(1-t)z_1 + (1-s)(1-t)z_2 \\ +(1+s)(1-t)x_3 - (1+s)(1-t)x_4 & +(1+s)(1-t)y_3 - (1+s)(1-t)y_4 & +(1+s)(1-t)z_3 - (1+s)(1-t)z_4 \\ -(1-s)(1+t)x_5 + (1-s)(1+t)x_6 & -(1-s)(1+t)y_5 + (1-s)(1+t)y_6 & -(1-s)(1+t)z_5 + (1-s)(1+t)z_6 \\ +(1+s)(1+t)x_7 - (1+s)(1+t)x_8 & +(1+s)(1+t)y_7 - (1+s)(1+t)y_8 & +(1+s)(1+t)z_7 - (1+s)(1+t)z_8 \\ \\ -(1-r)(1-t)x_1 - (1+r)(1-t)x_2 & -(1-r)(1-t)y_1 - (1+r)(1-t)y_2 & -(1-r)(1-t)z_1 - (1+r)(1-t)z_2 \\ +(1+r)(1-t)x_3 + (1-r)(1-t)x_4 & +(1+r)(1-t)y_3 + (1-r)(1-t)y_4 & +(1+r)(1-t)z_3 + (1-r)(1-t)z_4 \\ -(1-r)(1+t)x_5 - (1+r)(1+t)x_6 & -(1-r)(1+t)y_5 - (1+r)(1+t)y_6 & -(1-r)(1+t)z_5 - (1+r)(1+t)z_6 \\ +(1+r)(1+t)x_7 + (1-r)(1+t)x_8 & +(1+r)(1+t)y_7 + (1-r)(1+t)y_8 & +(1+r)(1+t)z_7 + (1-r)(1+t)z_8 \\ \\ -(1-r)(1-s)x_1 - (1+r)(1-s)x_2 & -(1-r)(1-s)y_1 - (1+r)(1-s)y_2 & -(1-r)(1-s)z_1 - (1+r)(1-s)z_2 \\ -(1+r)(1+s)x_3 - (1+r)(1-s)x_4 & -(1+r)(1+s)y_3 - (1+r)(1-s)y_4 & -(1+r)(1+s)z_3 - (1+r)(1-s)z_4 \\ +(1-r)(1-s)x_5 + (1+r)(1-s)x_6 & +(1-r)(1-s)y_5 + (1+r)(1-s)y_6 & +(1-r)(1-s)z_5 + (1+r)(1-s)z_6 \\ +(1+r)(1+s)x_7 + (1-r)(1+s)x_8 & +(1+r)(1+s)y_7 + (1-r)(1+s)y_8 & +(1+r)(1+s)z_7 + (1-r)(1+s)z_8 \end{bmatrix} \tag{C.2}$$

The individual terms of $[JI] \equiv [J]^{-1}$ are arranged in the geometric mapping matrix $[\bar{J}]$ as given in Eq. (C3).

$$\left[\bar{J}\right]=\begin{bmatrix} JI(1,1) & JI(1,2) & JI(1,3) & 0 & 0 & 0 & 0 & 0 & 0 \\ 0 & 0 & 0 & JI(2,1) & JI(2,2) & JI(2,3) & 0 & 0 & 0 \\ 0 & 0 & 0 & 0 & 0 & 0 & JI(3,1) & JI(3,2) & JI(3,3) \\ JI(2,1) & JI(2,2) & JI(2,3) & JI(1,1) & JI(1,2) & JI(1,3) & 0 & 0 & 0 \\ JI(3,1) & JI(3,2) & JI(3,3) & 0 & 0 & 0 & JI(1,1) & JI(1,2) & JI(1,3) \\ 0 & 0 & 0 & JI(3,1) & JI(3,2) & JI(3,3) & JI(2,1) & JI(2,2) & JI(2,3) \end{bmatrix} \quad \text{(C.3)}$$

The matrix of partial derivatives **[*P*]** is given as:

$$\left[P\right]=\begin{bmatrix} \varphi_{1,r} & 0 & 0 & \varphi_{2,r} & 0 & 0 & \varphi_{3,r} & 0 & 0 & \varphi_{4,r} & 0 & 0 & \varphi_{5,r} & 0 & 0 & \varphi_{6,r} & 0 & 0 & \varphi_{7,r} & 0 & 0 & \varphi_{8,r} & 0 & 0 \\ \varphi_{1,s} & 0 & 0 & \varphi_{2,s} & 0 & 0 & \varphi_{3,s} & 0 & 0 & \varphi_{4,s} & 0 & 0 & \varphi_{5,s} & 0 & 0 & \varphi_{6,s} & 0 & 0 & \varphi_{7,s} & 0 & 0 & \varphi_{8,s} & 0 & 0 \\ \varphi_{1,t} & 0 & 0 & \varphi_{2,t} & 0 & 0 & \varphi_{3,t} & 0 & 0 & \varphi_{4,t} & 0 & 0 & \varphi_{5,t} & 0 & 0 & \varphi_{6,t} & 0 & 0 & \varphi_{7,t} & 0 & 0 & \varphi_{8,t} & 0 & 0 \\ 0 & \varphi_{1,r} & 0 & 0 & \varphi_{2,r} & 0 & 0 & \varphi_{3,r} & 0 & 0 & \varphi_{4,r} & 0 & 0 & \varphi_{5,r} & 0 & 0 & \varphi_{6,r} & 0 & 0 & \varphi_{7,r} & 0 & 0 & \varphi_{8,r} & 0 \\ 0 & \varphi_{1,s} & 0 & 0 & \varphi_{2,s} & 0 & 0 & \varphi_{3,s} & 0 & 0 & \varphi_{4,s} & 0 & 0 & \varphi_{5,s} & 0 & 0 & \varphi_{6,s} & 0 & 0 & \varphi_{7,s} & 0 & 0 & \varphi_{8,s} & 0 \\ 0 & \varphi_{1,t} & 0 & 0 & \varphi_{2,t} & 0 & 0 & \varphi_{3,t} & 0 & 0 & \varphi_{4,t} & 0 & 0 & \varphi_{5,t} & 0 & 0 & \varphi_{6,t} & 0 & 0 & \varphi_{7,t} & 0 & 0 & \varphi_{8,t} & 0 \\ 0 & 0 & \varphi_{1,r} & 0 & 0 & \varphi_{2,r} & 0 & 0 & \varphi_{3,r} & 0 & 0 & \varphi_{4,r} & 0 & 0 & \varphi_{5,r} & 0 & 0 & \varphi_{6,r} & 0 & 0 & \varphi_{7,r} & 0 & 0 & \varphi_{8,r} \\ 0 & 0 & \varphi_{1,s} & 0 & 0 & \varphi_{2,s} & 0 & 0 & \varphi_{3,s} & 0 & 0 & \varphi_{4,s} & 0 & 0 & \varphi_{5,s} & 0 & 0 & \varphi_{6,s} & 0 & 0 & \varphi_{7,s} & 0 & 0 & \varphi_{8,s} \\ 0 & 0 & \varphi_{1,t} & 0 & 0 & \varphi_{2,t} & 0 & 0 & \varphi_{3,t} & 0 & 0 & \varphi_{4,t} & 0 & 0 & \varphi_{5,t} & 0 & 0 & \varphi_{6,t} & 0 & 0 & \varphi_{7,t} & 0 & 0 & \varphi_{8,t} \end{bmatrix} \quad \text{(C.4)}$$

VITA

Sourabh Sawant received his Bachelor of Engineering degree in mechanical engineering from Shivaji University, India in February 1999 and Master of Technology degree in mechanical engineering from Indian Institute of Technology, Madras, India in July 2000. He entered the mechanical engineering program at Texas A&M University in June 2005 and received his Doctor of Philosophy degree in December 2008. His research interests include solid mechanics and design. He plans to continue his career in this area.

Mr. Sawant can be reached at DeepSea Engineering and Management Inc., 10333 Richmond Avenue, Suite 600, Houston, TX 77042, USA. His email address is sourabhsawant@yahoo.com.